UNIVERSITÉ DU LUXEMBOURG

PhD-FSTM-2023-114
The Faculty of Science, Technology and Medicine

DISSERTATION

Defence held on 15/11/2023 in Luxembourg

to obtain the degree of

DOCTEUR DE L'UNIVERSITÉ DU LUXEMBOURG

EN *PHYSIQUE*

by

Yiwei ZHANG
Born on 25 October 1994 in Suzhou, Jiangsu, China

DEFORMING PARTICLES OUT OF EQUILIBRIUM: COLLECTIVE BEHAVIOURS AND FIELD THEORIES

Dissertation defence committee

Dr Etienne FODOR, dissertation supervisor
Assistant Professor, Université du Luxembourg

Dr Demian LEVIS
Lecturer, Universidad de Barcelona

Dr Massimiliano ESPOSITO
Professor, Université du Luxembourg

Dr Robert JACK
Professor, University of Cambridge

Dr Alexandre SOLON, Vice Chairman
Chargé de Recherche, Laboratoire de Physique Théorique de la Matière Condensée (LPTMC), CNRS

Abstract

Classical many-body systems out of thermal equilibrium exhibit a wealth of collective behaviours without equilibrium equivalents. Whilst such collective behaviours are often seen as the linchpin towards understanding many processes of living matter, they can hardly be directly predicted from the particle-based dynamics of each constituent. Models specifying the dynamics at individual level can be developed for numerical simulations to reproduce those collective behaviours. Such particle-based models promote the efficiency of simulations, whilst also capturing the most relevant model ingredients causing the collective behaviours of interest. Since collective behaviours often occur at a length scale significantly larger than a single particle and a time scale clearly slower than single-particle fluctuations, they are often described by field theories, which involve only a small number of free parameters and neglects the details of single-particle dynamics.
In this thesis, we are interested in two typical collective behaviours in biophysical context: contraction wave propagation as a dynamical pattern and transient liquid-liquid phase separation. For both collective behaviours, we propose models of dense assemblies of deforming spherical particles. Based on those particle-based models, we carry out particle-based simulations that show the corresponding collective behaviours and measure their dependence on control parameters. Furthermore, we derive field theories through systematic coarse-graining and analyse the collective behaviours at field-theoretic level. In the first part of the thesis, we report our results on pulsating active matter which shows contraction wave patterns. We show a phase diagram highlighting the conditions for such patterns to occur and investigate the natures of phase transitions involved. We also derive a noisy field theory that leads to the same phases in the same parameter space as in particle-based simulations. In the second part of the thesis, we report our results on a particle-based model allowing transient liquid-liquid phase separations. We investigate the relaxation towards steady states and the influence of control parameters on steady states. We also derive a field theory that maps the model to an effective equilibrium, and therefore analyse the field theory in a

free-energetic approach.

Acknowledgement

Exploring the laws that describe processes in nature has long been my central interest since my school time. Theoretical physics, in particular, due to its compact yet universal description using the language of maths, has always been my comfort zone in the world of science. During my PhD, the central task is always to receive substantial training for becoming an independent scientist.

Therefore, I should first thank Dr. Étienne Fodor, for giving me the opportunity to start such an adventure during the CoVid-19 pandemic. In his research group, I have had access to the exciting research projects under his guidance, which shed light on the proper directions for pushing my research work on those projects. In fact, he has paid gigantic effort in following every step of my research works in order to keep me on a correct track. Besides, my former and current colleagues, from postdocs to master interns, are all much more capable and generous than to share their opinions on my research work.

In the research community of soft matter and non-equilibrium statistical physics, many competitive researchers I met during conferences and workshops, such as Prof. Dr. Thomas Speck, Prof. Dr. Ludovic Berthier, Prof. Dr. Julien Tailleur, Prof. Dr. Xiaqing Shi, Dr. Yongfeng Zhao, etc., have shared their insightful and constructive opinions that help improve the technical treatments in my research works. Their suggestions deepened my understanding about the research fields my research works are in and make my technical treatments more solid.

I should not forget to thank the supporting teams at the University of Luxembourg, including the secretaries who intensively worked on my professional travels. Those travels are mostly supported by the funding of DPhyMS/DPPM with Prof. Dr. Thomas Schmidt being the administrator. His work should also be appreciated. Also, the HPC team's work must be recognised since they provide necessary training regularly and maintain the HPC at the University. Their timely answers to my raised issues on HPC are particularly useful to smoothen my research work.

I would also send my thanks to my friends in and outside DPhyMS that supported my PhD life in a non-technical way. They helped me find affordable accommodations and with other personal affairs, which are quite non-trivial in the Grand-Duchy. Without them, my research life would have been much more difficult.
In the end, I would be grateful for everyone around me who has had everyday or academic exchanges with me. Their information broadened my horizon and knowledge despite living and working in a small town.
Yiwei Zhang

Contents

Introduction

Soft matter physics is known for its *mesoscopic* scale of description, which is much larger than atoms and molecules but yet much smaller than macroscopic material pieces [1]. It encompasses physical processes carried by soft, mechanically deformable matter under thermal fluctuations. It is closely related to the physics of living matter, such as living cells and living tissues [2]. Living tissues are composed of living cells featuring organised biochemical processes fueling their active deformations. The active deformations of living cells, with finite lengths of spatial correlations, lead to *collective behaviours* at larger scales, such as tissue expansion [3] and migration [4]. Such collective behaviours are amongst the central processes of morphogenesis and therefore deserve further rational understanding.

A simple approach towards a theoretical understanding begins with microscopic models mimicking the dynamics of living cells. In this direction, vertex models have been shown to be effectively reproducing tissue dynamics driven by living cells [5–8] and are thus intensively studied. An essential advantage is that in vertex models, simple dynamical rules can be readily applied to mimic the dynamics of a large number of living cells, thus providing a platform to study the collective behaviours at "many-cell" level.

Not every single ingredient involved in the dynamical rules of each single cell independently contributes to the formation of collective behaviours at "many-cell" level. A drastic reduction in the number of free parameters should therefore be considered in the framework of continuum theories. Ideally, each of the remaining free parameters should be essential enough to fully highlight an independent aspect of the contribution to the formation of the collective behaviour of interest. For instance, the continuum limit of a vertex model can lead to a field-theoretic description which involves only a small set of ingredients [9].

Field theories are known for describing collective behaviours of systems with enormous degrees of freedom [10]. Their simpler formulation allows easier further analytical treatments and/or cheaper numerical simulations. In the context of pattern formation, a well-known example is the *complex Ginzburg-*

Landau equation which describes the formation of *Turing patterns* with a single deterministic partial differential equation [11]. In the context of phase ordering kinetics [12, 13], model A and model B are known as universal descriptions for non-conserved and conserved dynamics respectively, encoded in an underlying (effective) free energy functional describing a field theory.
Although being simple yet powerful, field theories do not guarantee that the collective behaviours they describe can be realised in practice. Indeed, many field theories are postulated only based on macroscopic symmetries, without referring to any microscopic details. Consequently, finding quantitative connections between coupling coefficients in field theories and microscopic parameters often turns out to be intractable. Alternatively, obtaining field theories by coarse-graining microscopic models explicitly maintains such macro-micro connections.
As is suggested by Manning [14], particles should be *deformable* in order to mimic deforming living cells. In order for particle deformation to play a central role, the particle assemblies should be dense [14]. In this context, the fluctuating internal degrees of freedom determining the shapes of particles are expected to collectively carve new classes of large-scale phenomenologies [14]. In fact, even deforming spherical particles subject to forces and fluctuations contain a rich source of novel behaviours [15, 16]. These novel behaviours should be relevant since dense assemblies of deforming spherical particles are expected to mimic the behaviours of living biological tissues [17]. Studying such models can build up the new physics describing the biophysical processes those living biological tissues undergo.
This thesis aims at proposing two particle-based models using deforming spherical particles. The first model represents a novel class of active matter: the pulsating active matter, in which particles actively deform. The second model, featuring a confining one-body potential landscape where each local minimum represents a specific species, reproduces species interconversion through particle deformation. Such a model provides a scheme of transient *liquid-liquid phase separations*(LLPS) via species interconversion, which is based on recent observations of intracellular LLPS [18, 19]. Based on both models, we perform systematic particle-based simulations for quantitative measurements of their collective behaviours, and derive field theories via standard coarse-graining procedures [20]. The obtained field theories are studied numerically and analytically to recover the observations in particle-based simulations.
This thesis is organised as follows: in Chapter 1, we review the state of the art of relevant studies and the methodologies used in this thesis. In Chapter 2, we present the results of our work on pulsating active matter. In Chapter 3, we present the results of our work on realising transient LLPS via species

interconversion.

Chapter 1

Stochastic Dynamics of Soft Systems: Individual and Collective Behaviours

In this chapter, we present the necessary techniques and motivations for the works described in this thesis. In Section 1.1, we describe the general motivations of the work. We begin with the state of the art of various fields of research related to this thesis, including active matter, tissue models, deforming particles and pattern formation. In Section 1.2, we introduce the standard coarse-graining method and numerical techniques used in this thesis.

1.1 State of the art

In this section, we review the scientific background of the work presented in this thesis. The background is covered by three aspects. In Subsection 1.1.2, we review the well-known models of active matter. In Subsection 1.1.3, we present existing particle-based and continuum models models for tissue dynamics. In Subsection 1.1.4, we introduce a model of deforming particles in the context of glassy dynamics.

1.1.1 Brownian motion

In 1827, Robert Brown, a scottish botanist, observed the "jittery" leaping behaviour of *amyloplasts* and *spherosomes*, minute particles ejected from pollen grains, when looking at the pollen of *Clarkia pulchella* through a microscope [21]. By replacing those particles in pedesis with inorganic particles,

he confirmed that this behaviour is not life-driven. Due to this experimental discovery, this random motion is later known as Brownian motion.
Although being baptised with his name, R. Brown was not the first to notice this type of motion. As early as in the first century B. C., pedesis was already mentioned in *De rerum natura*, a didactic poem by Lucretius, a Roman poet and philosopher, in order to convince his Roman audience of the existence of atoms. Small suspended dust particles, continuously hit by their neighbouring air molecules, becomes a perfect example of pedesis following the description in the poem. This example further suggests the mechanical origin of Brownian motion, since dust particles are usually seen as chemically inert. In 1785, Jan Ingenhousz observed similar behaviour of dust particles suspended in alcohol [22], four decades prior to Brown's discovery.
Theories illustrating the mechanical origin of Brownian motion were first probed by Albert Einstein in 1905 [23]. In his work, assuming that the motion of each suspended particle is independent from other suspended particles and each time interval of observation is independent, Einstein demonstrated that Brownian motion is the microscopic origin of diffusion. In a continuous liquid, Einstein recovered the diffusion equation based on the assumptions above by deriving the diffusion coefficient $D = \frac{1}{\tau}\int_{\mathbb{R}} \frac{\Delta^2}{2}\varphi(\Delta)\,\mathrm{d}\Delta$, where $\varphi(\Delta)$ is the probability density of particle displacement Δ within time τ.
Slightly later, in 1908, a particle-based approach to treat Brownian motion was adopted by Paul Langevin [24]. A Brownian particle at position $\mathbf{r}$ is considered to be damped by its surrounding fluid with a strength γ. To maintain its random motion, a random force $\mathbf{B}$ should exist to account for the frequent collisions. By simply applying Newton's second law, one may write down the one-body equation of motion

$$m\ddot{\mathbf{r}}(t) = -\gamma\dot{\mathbf{r}}(t) + \mathbf{B}(t) \tag{1.1}$$

where m is the mass of the Brownian particle. To satisfy the assumptions by Einstein, the random force should be a Gaussian white noise, i.e.

$$\langle B^{\alpha}(t)B^{\beta}(t')\rangle = 2\gamma k_{\mathrm{B}}T\delta^{\alpha\beta}\delta(t-t'), \tag{1.2}$$

where $\alpha, \beta \in \{x, y, ...\}$ represent Cartesian components, $\delta(t)$ is the delta distribution of time and $\langle\cdot\rangle$ is the noise average. At temperature T of the surrounding environment, the noise has a strength $2\gamma k_{\mathrm{B}}T$ where k_{B} is the Boltzmann constant. Using (1.2), one can also calculate the mean-squared displacement in the long-time limit

$$\langle(\mathbf{r}(t) - \mathbf{r}(0))^2\rangle = 2d\gamma k_{\mathrm{B}}Tt, \tag{1.3}$$

which recovers the result from the diffusion equation and build a relation $D = \gamma k_{\mathrm{B}}T$. For simplicity, in the following, we set $k_B = 1$.

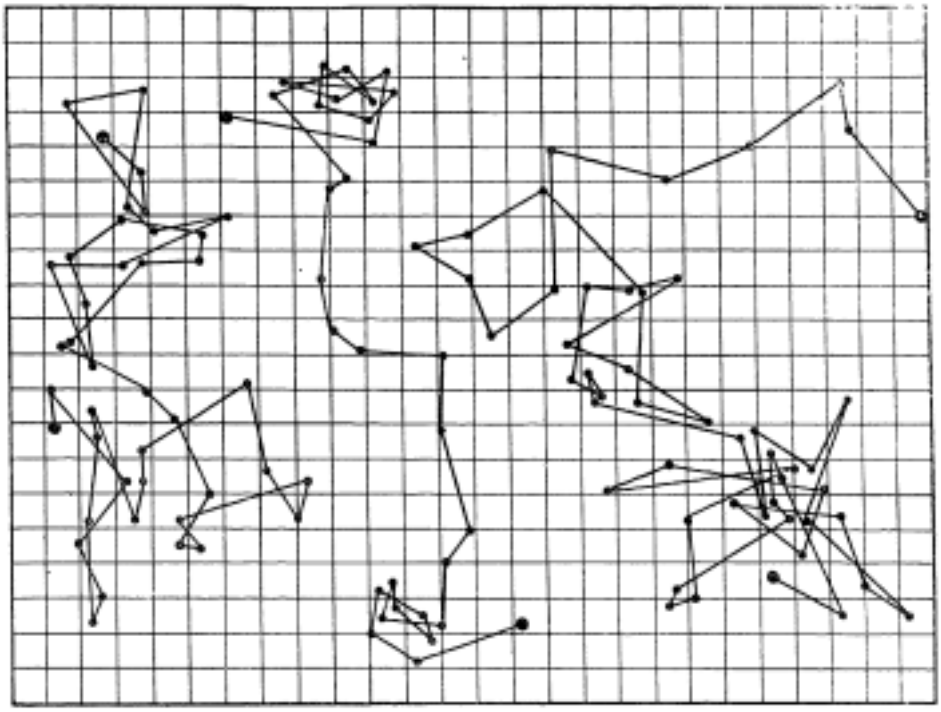

Figure 1.1: Trajectories of colloidal particles of radius 0.53 μm measured in experiments by Jean Perrin. The particle positions were recorded every 30s. The background grids have a uniformed mesh size 3.2 μm. Taken from [25]

.

In the same year, Jean Perrin reported his experiments using colloids for refined observations of Brownian motion [26]. Thanks to the more advanced optical tools, he managed to record the trajectories of the colloidal particles with an improved accuracy, up to the time resolution he had access to, as is shown in Figure 1.1 [25]. The theoretical description amounts to the overdamped regime of (1.2), namely the *overdamped Langevin equation*

$$\dot{\mathbf{r}}(t) = -\mu\partial_{\mathbf{r}}U + \sqrt{2D}\boldsymbol{\xi}(t), \tag{1.4}$$

which neglects the inertial effect $m\ddot{\mathbf{r}}$, with $\langle\xi_\alpha(t)\xi_{\alpha'}(t')\rangle = \delta_{\alpha\alpha'}\delta(t-t')$. Here $\mu = 1/\gamma$ is the mobility and U is the external potential.
Alternatively, one can adopt a probabilistic approach in order to calculate ensemble-averaged macroscopic observables. This is achieved by *Fokker-Planck equations*. One may start from the time-dependent probabilistic distribution in configuration space $P(\mathbf{r}, t)$ and write down the time-evolution

equation it satisfies

$$\partial_t P = \partial_{\mathbf{r}} \cdot (\mu \partial_{\mathbf{r}} U P + D \partial_{\mathbf{r}} P) \tag{1.5}$$

known as the Fokker-Planck equation. The stationary solution of (1.5) can be formally found to be the Boltzmann distribution

$$P_{\mathrm{s}}(\mathbf{r}) \propto \exp[-\beta U(\mathbf{r})], \tag{1.6}$$

where $\beta = 1/T$ is the inverse temperature [27].

1.1.2 Active matter

Particles in Brownian motion, namely *Brownian particles*, are considered inert. Brownian particles are *passively*, yet ceaselessly hit by the underlying solvent molecules in thermal motion, such that the pedesis of Brownian particles is sustained. In contrast, *active* particles sustain their motion *actively* by individually consuming external energy to generate driving forces. An assembly of active particles compose *active matter* [28]. The open-system nature of active matter gives rise to novel emergent phenomena on large scales, which is potentially capable of modelling the behaviours of living matter such as biological organisms [29]. Typical novel phenomena in active matter without equilibrium equivalents include the *motility-induced phase separation (MIPS)* [30], *flocking* [31], *rachet* [32], *active turbulence* [33], etc. For physicists, the clear non-equilibrium nature of active matter motivates the development of a novel toolbox of statistical mechanics beyond its success in equilibrium systems. Several classes of models for active matter have been proposed to produce the above-mentioned non-equilibrium phenomena with minimal setups, such that the essential pieces constituting the phenomenologies are preserved and concentrated on. Meanwhile, these models of active matter are simple enough for further investigations in terms of statistical mechanics. Two main classes of models are listed and introduced below in chronological order.

Aligning active matter: Flocking transition Before the birth of the concept "active matter", self-driven particles have already been found to exhibit the flocking transition, a novel, kinetic phase transition that is analogous to the spatial ordering in equilibrium [34]. However, the flocking transition has recently been found to have a different nature from spatial ordering in equilibrium [35]. Examples of its applications range from bird flock and fish schools to vehicular traffic [36].
Essentially, the Vicsek model may be seen as a "mobile XY model". In Vicesk model, each moving agent carries an XY-spin value indicating the direction of

its velocity. The simplest setup is composed by polar particles described by its position $\mathbf{r}(t)$ and its velocity $\mathbf{v}(t)$, with $v = \|\mathbf{v}\|$ being a fixed parameter. The direction of $\mathbf{v}$ is determined by the "spin" value $\theta(t)$ which is updated in time. The dynamics takes place over discrete time $t \in \mathbb{Z}$. The rules of update read

$$\begin{aligned} \mathbf{r}_i(t+1) &= \mathbf{r}_i(t) + \mathbf{v}_i(t) \\ \theta_i(t+1) &= \langle \theta(t) \rangle_r + \xi_i(t), \end{aligned} \tag{1.7}$$

where the *average direction* $\langle \cdot \rangle_r$ denotes the average over particles within a circle of radius r (Here we set $r = 1$ for convenience, as the unit measuring the system size), including the particle i itself. Here the average direction is defined as $\langle \theta(t) \rangle_r = \arctan(\langle \sin\theta(t) \rangle_r / \langle \cos\theta(t) \rangle_r)$. A random number $\xi_i(t)$ also contributes to the update of θ_i as a deviation from the short-range average. To play the role of a noise, it takes a value from a uniform distribution over a fixed interval $[-\eta/2, \eta/2]$. Therefore another parameter $\eta > 0$ measures the noise strength. Besides v, η, the number density ρ measuring the size of the particle crowd is the only remaining parameter determining the large-scale dynamics.

With the setup described by (1.7), Vicsek *et al.* carried out the simulations in a system of N point particles living in a square box of size L with periodic boundary conditions in both dimensions, such that $\rho = N/L^2$. The speed v only determines the moving distance by a single update. It should be finite in order to move the particles, whilst not too large compared to r, in order to avoid large numerical errors. Within this range, the speed v was found not to affect the results. Hence the control parameters become the number density ρ and noise strength η.

Figure 1.2 (a)-(d) visualise the results from particle-based simulations, where the instantaneous velocities on particles were indicated by an arrow, forming a *velocity field*. The short curve segments attached to the arrows demonstrate the trajectories in the past 20 timesteps. The initial configurations at $t = 0$ were always chosen to be disordered, as is shown in (a). (b)-(d) show the different steady states resulting from different magnitudes of ρ and η. When both ρ and η are small, the particles form clusters moving randomly and "coherently" [34]. See Figure 1.2 (b). When both ρ and η are large, it is random motions of particles with "some correlations" [34] that was observed. See Figure 1.2 (c). The flocking takes place at large ρ and small η. In this case, the velocity field becomes globally ordered up to local fluctuations, which is analogous to the spontaneous symmetry breaking in equilibrium continuous ferromagnetic transitions. This kinetic phase transition is possible due to the lack of total momentum conservation, since the particles are driven by

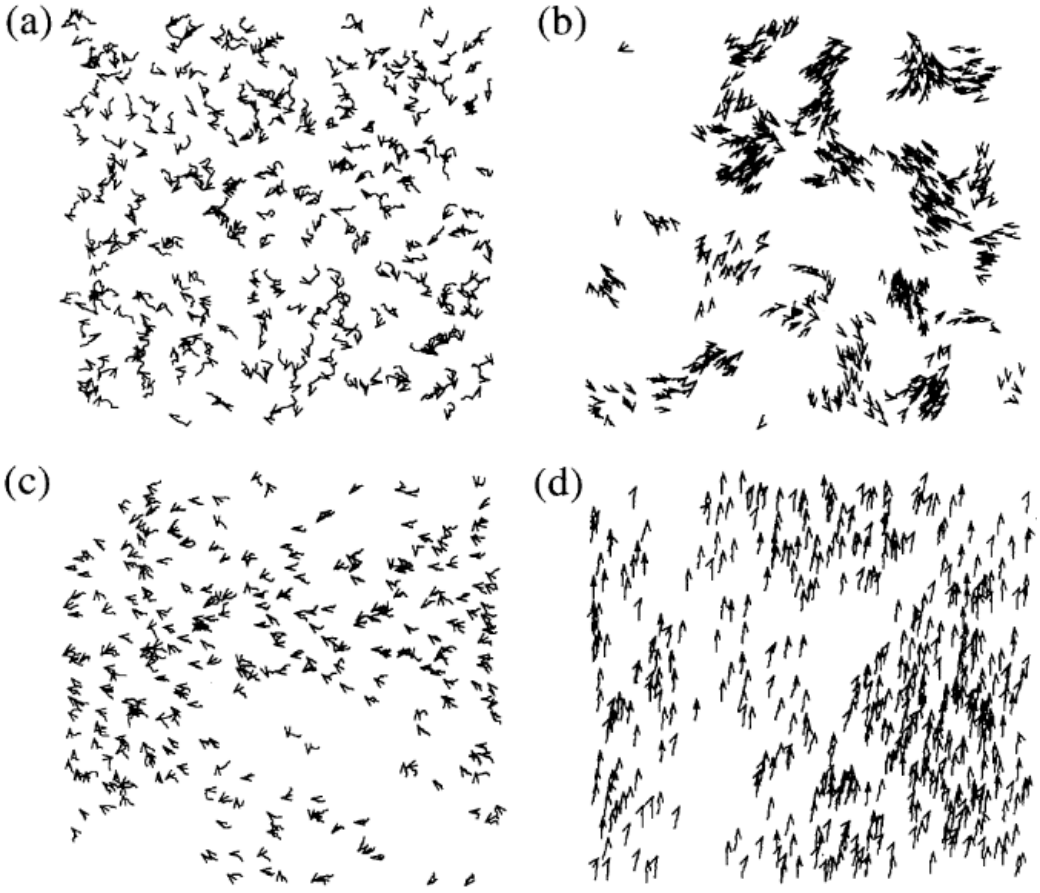

Figure 1.2: Simulation results of Vicsek model. Starting from a disordered configuration (a) of $\{\theta_i(0)\}$, the simulations lead to different steady states (b)-(d). (b) Low density ρ together with weak noise η leads to clusters of random coherent motion. (c) High density ρ together with strong noise η leads to random motion of particles with weak spatial correlations. No clusters are formed. (d) High density ρ together with weak noise η leads to global flocking with the particle velocities being globally ordered. Taken from [34].

active velocities. This flocking transition exhibits a long-range order, which is forbidden in equilibrium by the Mermin-Wagner theorem [37, 38].
Upon observing the flocking transition, Vicsek *et al.* assumed it continuous and measured the critical exponents around the flocking transition. The order parameter characterising the flocking transition is chosen to be the norm of the normalised averaged velocity

$$v_a = \frac{1}{Nv}\left\|\sum_{i=1}^{N}\mathbf{v}_i\right\|. \tag{1.8}$$

The order parameter v_a ranges from 0 to 1. The closer v_a is to the unity, the more ordered the velocities are. In the work by Vicsek *et al*, the critical exponents in the power-law decays

$$v_a \propto [\eta_c(\rho) - \eta]^{\beta}, v_a \propto [\rho - \rho_c(\eta)]^{\delta} \tag{1.9}$$

were considered. The two exponents were measured to be $\beta = 0.45\pm0.07, \delta = 0.35 \pm 0.06$.
Later, Toner and Tu proposed a field-theoretic description allowing the flocking transition, namely the *Toner-Tu* equation [39–41]

$$\begin{aligned}(\partial_t + \lambda\mathbf{v}\cdot\partial_{\mathbf{r}})\mathbf{v} + \partial_{\mathbf{r}}P &= (a - b|\mathbf{v}|^2)\mathbf{v} + D_1\partial^2_{\mathbf{rr}}\mathbf{v} \\ &\quad + D_L\partial_{\mathbf{r}}(\partial_{\mathbf{r}}\cdot\mathbf{v}) + D_2(\mathbf{v}\cdot\partial_{\mathbf{r}})^2\mathbf{v} + \mathbf{f}, \\ \partial_t\rho + \partial_{\mathbf{r}}\cdot(\rho\mathbf{v}) &= 0,\end{aligned} \tag{1.10}$$

where $\mathbf{f}$ is a Gaussian random noise satisfying

$$\langle f_\mu(\mathbf{r},t) f_\nu(\mathbf{r}',t')\rangle = \Delta\delta_{\mu\nu}\delta(\mathbf{r}-\mathbf{r}')\delta(t-t'), \tag{1.11}$$

with Δ being constant and μ, ν the Cartesian components. In Equation (1.10), the coefficient b along with all diffusion coefficients , $D_{1,2,L}$ is positive. $a > 0$ leads to the ordered phase and $a < 0$ results in the disordered phase. The pressure P is a function of local density ρ.
The Toner-Tu equation (1.10) in its complete form is built without referring to microscopic details, containing all terms obeying the macroscopic symmetries. As a result, the large number of parameters in Equation (1.10) can hardly be connected to particle-based models [35]. So far, no simulations of the Toner-Tu equation (1.10) without simplification have been reported. Still, under the framework of Toner-Tu equation, the dynamical renormalisation group (RG) analysis set constraints between critical exponents existing

in the approximated RG-flow equations near the fixed point of the flocking transition [39]. The constraints refer to the values of those critical exponents in terms of spatial dimensions d. Nevertheless, later quantitative insights into flocking transition indicate discrepancies from the measurement by Toner and Tu in 1995 [42].
Still, numerical evidences are indispensable. Instead of simulating Equation (1.10), Chaté simulated equations reminiscent of (1.10) derived through systematic coarse-graining [35]. There, based on Vicsek class models, which belongs to a broader class called *Dry Aligning Dilute Active Matter* (DADAM), Chaté simulated the hydrodynamic equations

$$\begin{aligned} \partial_t \rho &= -\operatorname{Re}\{\overline{\partial} f_1\}, \\ \partial_t f_1 + \kappa_1 f_1 \overline{\partial} f_1 + \kappa_2 \overline{f}_1 \partial f_1 &= [\mu(\rho) - \xi |f_1|^2] f_1 - \frac{1}{2}\partial\rho + D\partial\overline{\partial} f_1, \end{aligned} \tag{1.12}$$

where ρ is the real-valued density field over a complex plane $\mathbb{Z}$, $f_1 = \rho(v_x + \mathrm{i}v_y)$ is the $\rho\mathbf{v}$-field of Equation (1.10) but over a complex plane, $\partial = \partial_z, \overline{\partial} = \partial_{\overline{z}}$ are partial derivative operators with respect to complex coordinates $z = x + \mathrm{i}y, \overline{z} = x - \mathrm{i}y$. Instead of a disorder-order transition scheme, flocking is considered under a liquid-gas transition scheme, which is of first order instead of second order. See Figure 1.3. Indeed, flocking entails a spatial separation between a dense region and a dilute region, as is shown in Figure 1.2. Between the gaseous and liquid configurations, the flocking transition goes through a coexistence region featuring multiple chaotic bands of high densities, which is reproduced as a solution of the hydrodynamic equation (1.12). See Figure 1.4.

Repulsive active matter: Motility-induced phase separation The flocking transition observed in Vicsek Model requires a pivotal role of alignments between active velocities. This interaction is non-conservative, as the neighbours of each particle change in time. This non-conservative alignment interaction is another element causing the non-equilibrium nature. In fact, a simpler model of active matter may be achieved by reducing the weight of alignment in the model, or even neglect it. In those models without alignment, isotropic active particles repel each other upon overlapping. Such a non-interacting limit is sufficient for non-trivial density profiles to be observed as steady states in experiments using synthetic active colloids [30].
One potential theoretical model is to consider self-propelled spheres with isotropic interactions between them. These isotropic interactions, without alignment between active velocities, may be repulsive or attractive, short-range or long-range, etc. A physically novel case is to apply only repulsive

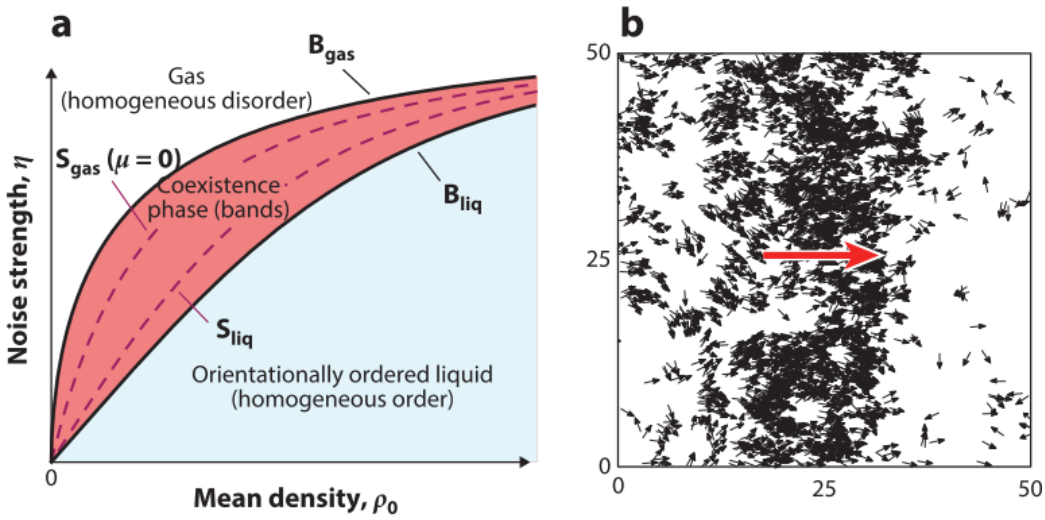

Figure 1.3: (a) Phase diagram involving the flocking transition of Vicsek-type models and its hydrodynamics (1.12). Clearly, a coexistence region containing multiple chaotic bands highlights the first-order nature of the transition. (b) Snapshot from simulation of Vicsek model showing a single band travelling along the red arrow, which exists in the disordered liquid phase. Taken from [35].

short-range interactions between particles, after which a liquid-gas phase separation can exist as a steady state. This is clearly unimaginable in equilibrium, without active velocities—how can particles condensate into clusters without attractive or effectively attractive interactions?

Such a condensation featuring a liquid-gas phase separation hence results from active driving velocities. This mechanism enables the phase separation by departing from equilibrium, known as *mobility-induced phase separation* (MIPS). In MIPS, the system density ρ and the active speed v become control parameters. In a regime where the speeds of particles drastically fall due to strong repulsion from crowding particles, a liquid-gas phase separation becomes stable. Such MIPS has been observed both experimentally and theoretically, see Figure 1.5.

Constructing a model to realise MIPS then requires using motile particles as building blocks. Two limiting cases are *run-and-tumble particles* (RTPs), which swim persistently and tumble suddenly in discrete time spots at a rate α, and *active Brownian particles* (ABPs), which swim at a fixed speed but in directions subject to noises in continuous time, i.e. *rotational diffusions* [30, 44]. Both RTPs and ABPs can lead to MIPS, although having different swimming schemes at microscopic level, see Figure 1.6. In fact, once

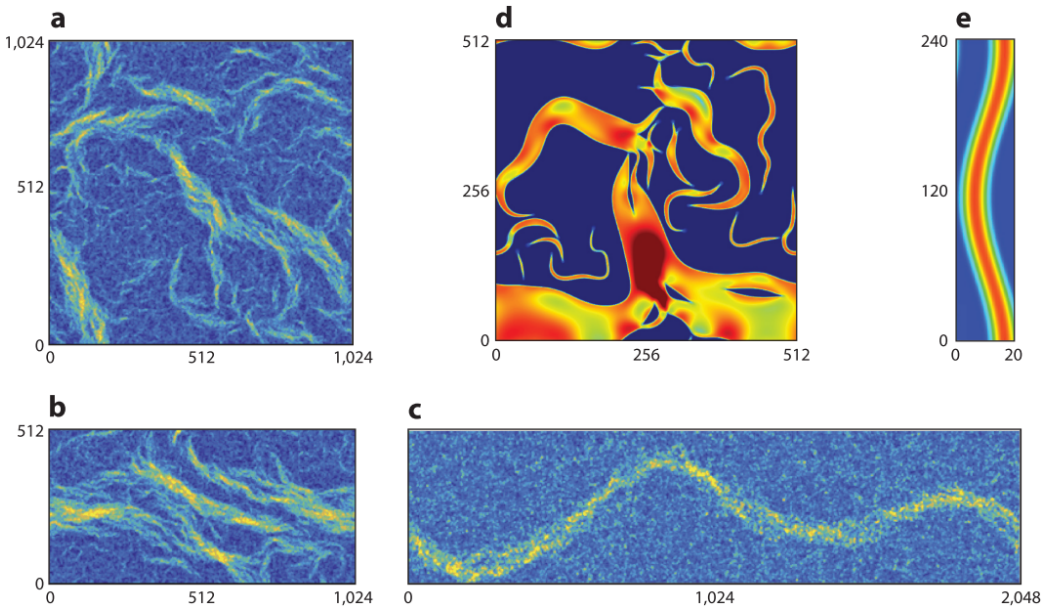

Figure 1.4: (a)-(c) Snapshots showing the band chaos in nematic DADAM models within the coexistence region of Figure 1.3 (a), where the flocking bands endlessly bend, split and merge with each other. (d),(e) Snapshots showing the spatiotemporal band chaos solutions of hydrodynamics. Taken from [35].

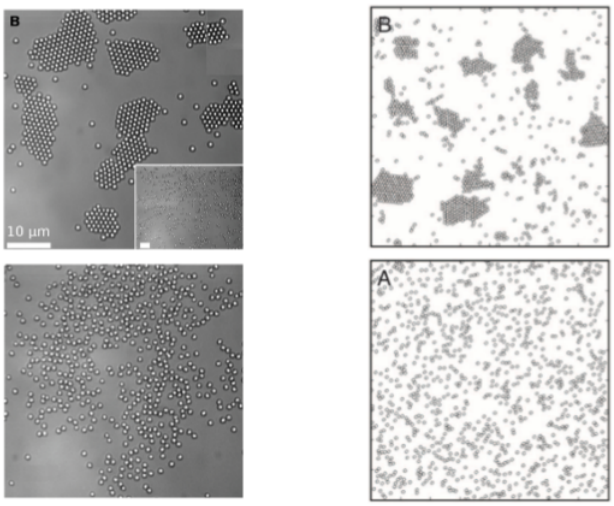

Figure 1.5: MIPS observed in experiments (left) and simulations (right). Turning off the light in experiments removes the active velocity of colloidal particles, leading to a homogeneous density distribution. (lower left) In simulations, this is achieved by reducing or removing the active velocities of particles (lower right). MIPS occurs when the light is on, due to sufficient self-propulsion of collidial particles (upper left). This is realised in simulations by assigning a strong enough active velocity to each particle. (upper right) Taken from [43].

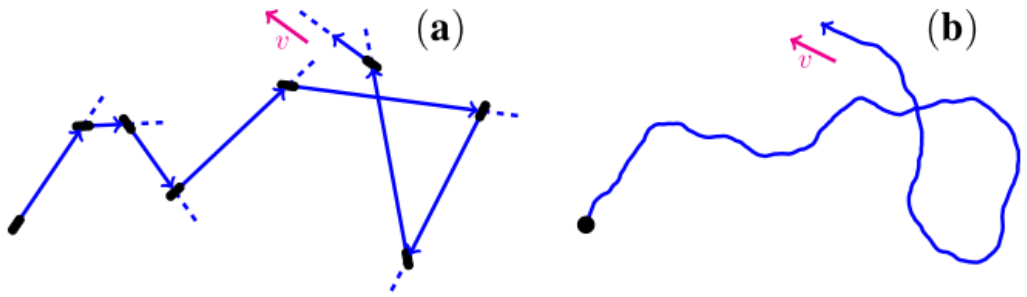

Figure 1.6: Schemes of run-and-tumble particles (RTPs) (a) and active Brownian particles (ABPs) (b). The reorientations of RTP are jump events in discrete times, whilst ABP reorientate via rotational diffusion in continuous time. Taken from [30, 44].

the swimming speeds v and tumbling rate α are isotropic, in a superposition between RTPs and ABPs in a d-dimensional space, an exchange between α and $(d-1)D_r$ keeps the orientational relaxation time τ invariant. Here D_r is the angular diffusion coefficient of ABPs. This is explicitly shown by

$$\tau^{-1} = \alpha + (d-1)D_r. \tag{1.13}$$

Compared to the Vicsek model, RTPs and ABPs are defined on continuous time instead of discrete time. Therefore, explicit stochastic differential equations can be used to describe RTPs and ABPs. With continuous-time descriptions, tools treating *continuous-time random walks* (CTRWs) can be applied to investigate the first-passage time statistics [45], thus allowing one to consider treating trapping problems of RTPs and ABPs [46] analytically.

1.1.3 Models of tissues

We switch our scope from a group of individuals to a piece of biological tissue. *Living* biological tissues are well-organised clusters of *living* cells carrying life activities. Similar to *living* bacteria, *living* cells are driven by internal biochemical processes to perform *active* motions individually. Their motions are organised to allow collective dynamics of tissues, such as wound healing, morphogenesis, cancer invasion, etc [47]. These intrinsically non-equilibrium processes have been studies *in vitro* using epithelial monolayers as a model system for tissues [3, 4, 48–50]. They have been found to mechanically drive plenty of collective dynamics under classes of collective migration, glass transition, active turbulence, etc [51]. The richness in non-equilibrium collective dynamics has motivated theoretical studies using different models for this

type of active matter. Prior to this thesis, most theoretical studies were based on vertex models and/or continuum models. Here we review some already existing models of biological tissues.

Vertex models To simplify the description of epithelial monolayers and reduce the computational cost, epithelial cells can be represented by polygons, often produced by Voronoi division of space. Edges and vertices are shared between neighbouring polygon cells. A bidimensional vertex model usually models a single cross section of an epithelial monolayer, but contains all essential descriptions for its tridimensional dynamics [7].
Under this setup, specific dynamics can be defined by applying rules to the motion of vertices

$$\dot{\mathbf{r}}_i = \mu \mathbf{F}_i, \tag{1.14}$$

where the position of vertex i varies according to the total force $\mathbf{F}_i$ exerted on it, up to a mobility coefficient μ. Current models can be divided into two classes, based on the arguments deriving the components of $\mathbf{F}_i$, as is shown in Figure 1.7. From a force-based approach first derived by Weliky and Oster [7, 52], models can be derived with membrane tensions $\hat{\mathbf{u}}_i^\alpha, \hat{\mathbf{v}}_i^\alpha$ exerted by a neighbouring cell α along its two shared edges associated with vertex i. Besides, the "cortical pressure", i.e. the difference between the osmotic pressure and the restraining elastic pressure, contributes an off-edge force component $\hat{\mathbf{p}}_i^j$.
The force-based approach is handy when all force components are known. Quite often, these cases are far from equibrium, with all force components contributing to vertex i being localised. In contrast, when studying the relaxation towards equilibrium, the driving forces are often not well specified. Here, the energy-based approach, which is more intuitive, may be adopted [6, 7]. In this approach, instead of specifying forces on vertex i, one calculates the total force as the negative gradient $\mathbf{F}_i = -\partial_{\mathbf{r}_i} U$ of an underlying potential energy U of the whole system. In the example depicted in Figure 1.7, the contribution to the gradient force $\mathbf{F}_i$ by a single neighbouring cell α can be separated into two off-edge components with clear physical interpretations. One component varies the area A_α of cell α to approach an ideal area $A_\alpha^{(0)}$, whereas the other component tunes the perimeter P_α of cell α.
The computation power of such vertex models has been revealed by mimicking several typical cell dynamic behaviours, including neighbour exchange, vertex merging, cell removal, cell division, etc. See Figure 1.8.

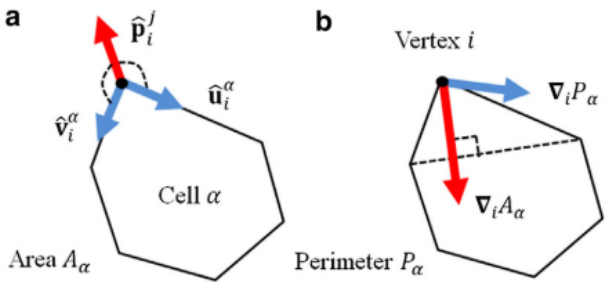

Figure 1.7: Schemes of force assignment in vertex models. The force contributions to a vertex are based on its neighbouring cells. Based on a single neighbouring cell α, the phenomenological scheme (a) explicitly assigns forces $\hat{\mathbf{u}}_i^\alpha, \hat{\mathbf{v}}_i^\alpha$ (blue) for perimeter contraction along the two neighbouring edges, and an off-edge cortical pressure $\hat{\mathbf{p}}_i^j$ (red), whilst the energy-based approach computes an off-edge force based on the gradient of an underlying potential U, and decomposes the force into contributions based on their physical interpretations. Taken from [7].

Continuum models Vertex models as models defined in discrete space have been successful in mimicking several microscopic behaviours of epithelial cells. These microscopic behaviours can potentially give rise to macroscopic patterns that can be simulated with vertex models, which is useful in linking certain collective behaviours to their microscopic origins. However, the underlying macroscopic instabilities behind those collective behaviours, especially the relevant factors leading to them, may be implicit in vertex models.

At multicellular level, several continuum models have been developed, depending on the application scenarios. In the context of morphogenesis, especially wound healing, models focusing on the collective migration of cells, which are driven by cell activities, often centre on velocity fields [1, 53]. Besides collective migrations, the mechanochemical coupling in living tissues, by forming a feedback loop between mechanical stress and biochemical regulations, is in fact responsible for an abundance of collective behaviours [51, 53].
In particular, to describe the experimentally observed wave propagation driven by local cell contractions triggered by a protein known as ERK (Figure 1.9) [50], a continuum model was derived and investigated by Boocock *et al* [51]. Taking the continuum limit transforms the set of equations of motion of vertices into a system of partial differential equations about the displacement $\mathbf{r}$ of a vertex, cell length l_0 and ERK activity E at position $\mathbf{x}$

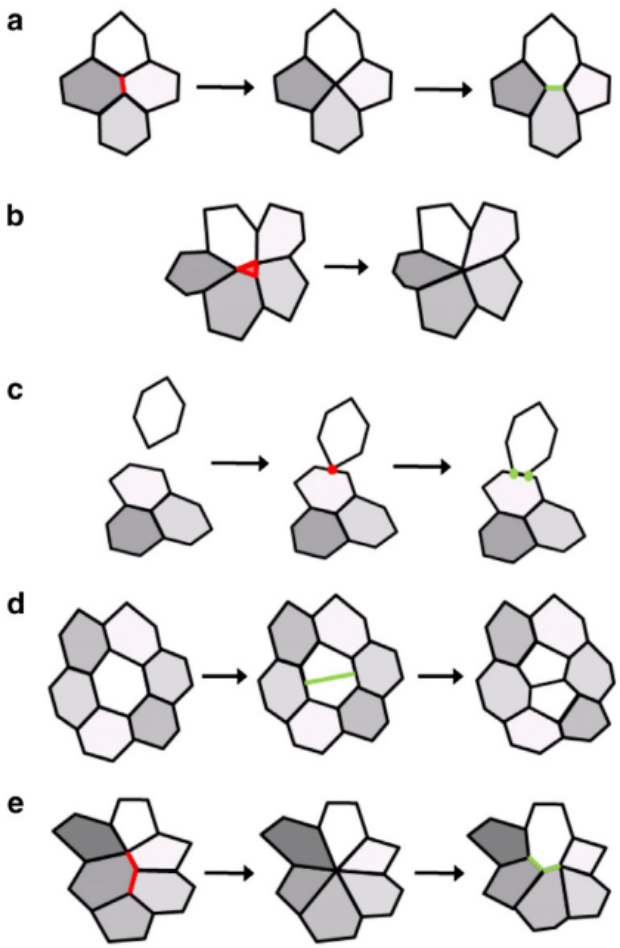

Figure 1.8: Types of vertex dynamics mimicking cell dynamic processes. (a) edge reorganisation through vertex merging via edge shrinkage followed by the birth of a new edge from the merged vertex. (b) cell removal mimicking apoptosis. (c) vertex creation via vertex-edge intersection. (d) Cell division by adding a pair of vertices bonded with a new edge. (e) Multicellular edge reorganisation. Taken from [7].

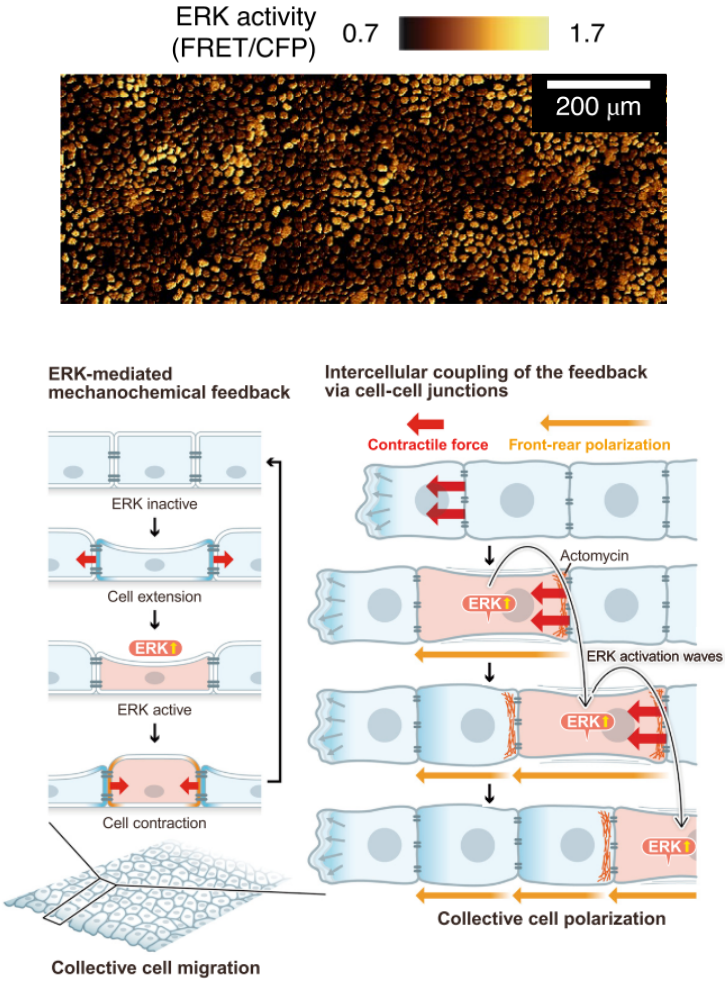

Figure 1.9: Cell contraction waves carried by circular deformation of cells driven by the activity of ERK, independent of systematic cell migration. The snapshot (top) of experimental observation highlights the ERK activity using FRET techniques, with light colours representing high ERK activity and consequently, extended cells. The scheme of such a wave propagation (below) shows the mechanism of ERK activity propagation via cell-cell couplings. Taken from [50].

and time t. After redefining $l_0 \to l_0 - l_{\mathrm{st}}, E \to E_{\mathrm{st}}$, where "st" means values in the steady state, one obtains

$$\begin{aligned} \tau_{\mathbf{r}} \partial_t \mathbf{r}(\mathbf{x}, t) &= \partial^2_{\mathbf{xx}} \mathbf{r}(\mathbf{x}, t) - \partial_{\mathbf{x}} l_0(\mathbf{x}, t) \\ \tau_l \partial_t l_0(\mathbf{x}, t) &= -l_0(\mathbf{x}, t) - \alpha E(\mathbf{x}, t) \\ \tau_E \partial_t E(\mathbf{x}, t) &= -E(\mathbf{x}, t) + \beta \partial_{\mathbf{x}} \mathbf{r}(\mathbf{x}, t). \end{aligned} \tag{1.15}$$

In Equations (1.15), the first equation describes the motion of the vertex at position $\mathbf{x}$ and time t. On the right hand side (RHS), the first term describes vertex diffusion, whilst the second term sets a drift driven by the cell length relaxation at position $\mathbf{x}$ and time t. The second equation then describes the relaxation of cell length at position $\mathbf{x}$ and time t. On the RHS, the first term assigns a restoring force following the Hook's law, whilst the second term is the contribution from the ERK activity at position $\mathbf{x}$ and time t. The third equation then describes the evolution of ERK activity at position $\mathbf{x}$ and time t, with the first term on the RHS being restoring and the second term couples to cell length, as $\partial_{\mathbf{x}} \mathbf{r}$ is proportional to the average length claimed by a cell and thus inversely proportional to vertex density. Notably, all three equations are fully local, enabling a pointwise analysis.
The above system (1.15) clearly has a homogeneous fixed point which is static. In this steady state, there is no pattern. Patterns such as wave propagation should arise as instabilities of homogeneous fixed points, where nonzero ERK activity E drives cell deformation $\partial_t l_0$, as was shown in the experiment. The conditions for instabilities should be found out by using linear stability analysis on Equation (1.15). The result should be presented as a dispersion relation in Fourier space. Such a dispersion relation should then admit instabilities at strong enough coupling strengths $\alpha\beta > (\alpha\beta)_{\mathrm{c}}$ between ERK activity and cell length. This predicts the length scale and frequency of patterns. From the length scale and frequency of patterns, one can conclude that the critical shape of patterns is determined by the relaxation time scales $\tau_{\mathbf{r}}, \tau_l, \tau_E$. These predictions were further confirmed by numerical simulations in [51]. Similar strategies of modelling patterns produced by cell contraction have also been adopted in [54–56], etc. The derivation of such continuum models from vertex models was systematically discussed on in [57].

1.1.4 Deforming particles

Vertex models are successful in that they resemble biological tissues composed of cells, while being simple enough to allow dynamic rules to be implemented. In particular, as particle-based models, vertex models can lead to

continuum models at field-theoretic level, which ease the studies of macroscopic patterns as collective behaviours. Instead of looking into microscopic details, continuum models describe their behaviours using a reduced number of macroscopic parameters.

In fact, each vertex may be seen as a particle, the interaction range of which is defined through the shapes and sizes of its neighbouring cells. In this sense, vertices should be seen as *deforming particles*, since the cells are usually deforming. Between these deforming particles, the interactions are *anisotropic*, which is an origin of the large amount of microscopic details. Besides taking the continuum models directly from those vertex models, another approach of simplifying the model is to make the interactions *isotropic*, i.e. to consider *spherical particles*. With the shape being constraint to spheres, the only degrees of freedom for deformation become particle sizes, i.e. the radii of spherical particles.

An advantage of such a simplification is that particle deformation is explicitly separated from particle displacement [17]. Particle positions can be captured by the positions of their centres of mass, whilst their shapes are described only with their radii. These two quantities are well distinguished from each other, allowing the dynamic rules on displacement and deformation to be separately applied, such that their contributions towards the formation of patterns can be further clarified. As a comparison, in vertex models, the dynamic rules moving the vertices translate and deform the particles simultaneously, which is more intuitive and phenomenological but hinders further scrutiny into their respective roles.

Taking advantage of this separation, the physical origins of macroscopic behaviours of dense living tissues can be studied in detail. As an example, in [17], a model composed of a dense assembly of *actively* deforming particles is proposed, aiming at describing dense biological tissues. The particle-based equations of motion read

$$\begin{aligned} \dot{\mathbf{r}}_i &= -\mu \sum_{j \neq i} \partial_{\mathbf{r}_i} U(r_{ij}) \\ \sigma_i(t) &= \sigma_i^0 [1 + a \cos(\omega t + \psi_i)]. \end{aligned} \tag{1.16}$$

In this model, particle radii are driven to oscillate, whilst particles are not self-propelled, such that the effect of *actively* driven deformation could be singled out. Here the repulsive harmonic potential $U(r_{ij}) = \frac{\varepsilon}{2}(1 - r_{ij}/\sigma_{ij})^2 \Theta(\sigma_{ij} - r_{ij})$ has a restricted range defined by a Heaviside kernel Θ, which allows the repulsion to be turned on only when the involved particles overlap. Between particles i and j, the two-body distance $r_{ij} = |\mathbf{r}_i - \mathbf{r}_j|$ is compared to the sum of their radii $\sigma_{ij} = \sigma_i + \sigma_j$ in order to determine whether they overlap or not.

The radius σ_i of each particle i is driven individually to oscillate around σ_i^0 with an amplitude a, at a frequency ω, up to a random phase ψ_i that keeps the total packing fraction $\varphi = \sum_i \frac{\pi\sigma_i^2}{L^2}$ almost constant. With this setup, the solid-liquid transition of this assembly is investigated. The amplitude a, chosen as the main control parameter, determines the largest possible size difference between particles, measuring the effect the active drive ω brings to the system. It was found that the solid-fluid transition occurs at a critical amplitude a_c, below which the assembly remains solid and each particle stays around its original position in the steady state. At large amplitude $a > a_c$, particles are allowed to perform large irreversible displacements that allow local rearrangements of particles. This is clearly a feature of fluids. See Figure 1.10. This result indicates that the active deformations of cells alone are sufficient to realise a solid-fluid transition of dense biological tissue.
Beyond active deformations, the Kuramoto-type interactions [58] can bring spatial correlations propagated via synchronisation between nearest neighbours, such that the effect of local active deformation can potentially lead to large-scale patterns. This was first proposed by Togashi [16] aiming at modelling the crowds of (bio-)molecular machines such as enzymes, the deformations of which are driven by chemical reactions. Here, the chemical reactions are modelled as synchronisation between neighbouring molecules, with the corresponding chemical changes of each molecule described by the deformation of a spherical particle. The model reads

$$\begin{aligned} \dot{\mathbf{r}}_i &= -\mu \sum_{j\neq i} \partial_{\mathbf{r}_i} U(r_{ij}) + \sqrt{2\mu T}\boldsymbol{\xi}_i(t) \\ \dot{\theta}_i &= \omega + \sum_{j\neq i} [\varepsilon \sin(\theta_j - \theta_i)\Theta(\sigma_{ij} - r_{ij}) - \mu_\theta \partial_{\theta_i} U(r_{ij})] + \sqrt{2\mu_\theta T}\eta_i(t). \end{aligned} \tag{1.17}$$

Compared to the model in [17], there are several differences and extensions in the model (1.17):

- The simulations are carried out at *finite* temperature T.
- The repulsion U has a direct impact $\partial_{\theta_i} U$ on particle deformation.
- Neighbouring particles are encouraged to be synchronised in their sizes via $\varepsilon \sin(\theta_j - \theta_i)$.

Besides, here the WCA repulsion $U(r_{ij}) = [(r_{ij}/\sigma_{ij})^{12} - (r_{ij}/\sigma_{ij})^6 + 1/4]\Theta(\sigma_{ij} - r_{ij})$ is used, instead of a harmonic potential. The effect of finite temperature exists as zero-mean Gaussian white noises $\boldsymbol{\xi}_i(t), \eta_i(t)$ with amplitudes measured by diffusion coefficients $D = \mu T$ and $D_\theta = \mu_\theta T$ respectively. With

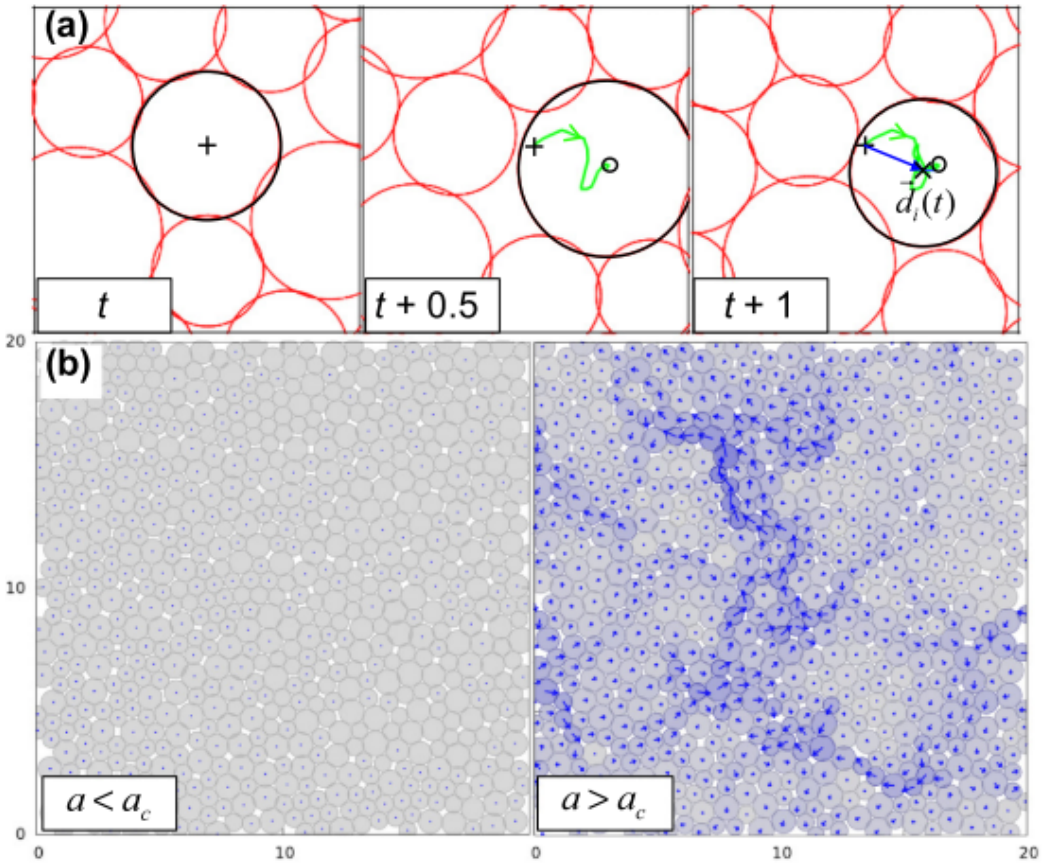

Figure 1.10: Solid-fluid transition realised in a dense assembly of actively deforming particles. (a) Snapshots over a single cycle of active deformation, where a highlighted deforming particle i (black) in the dense assembly moves along the short trajectory marked in green, leading to a displacement $\mathbf{d}_i(t) = \mathbf{r}_i(t+1) - \mathbf{r}_i(t)$ marked in blue. (b) Snapshots of the dense assemblies in steady states, with subcritical (left) and supercritical (right) deformation amplitudes a. Each blue arrow shows the displacement of a particle within a single active deformation cycle. When $a < a_c$ (left), the displacements are tiny, whereas when $a > a_c$ (right), systematic displacements occur in a cycle. Taken from [17].

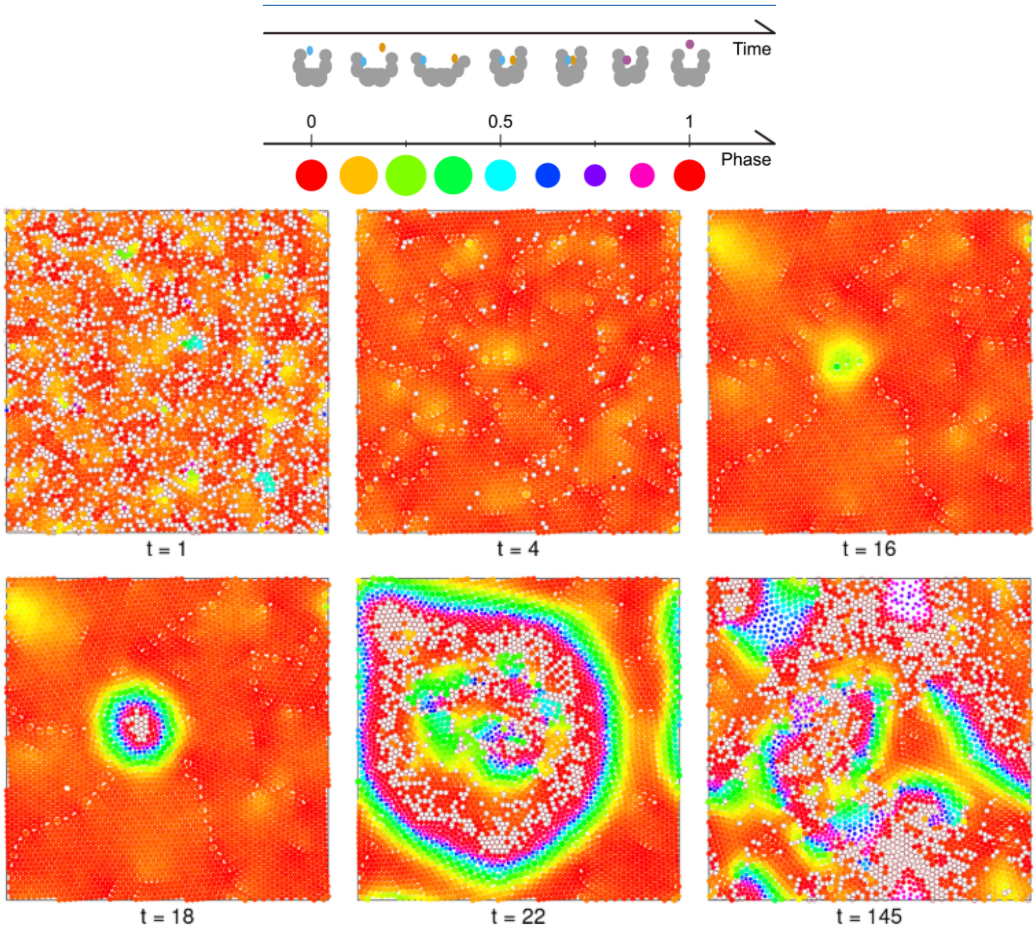

Figure 1.11: Wave propagation via particle deformation observed in particle-based simulations. A cyclic colour scheme is used to denote particles of cyclically changing sizes, which mimics a reaction cycle of enzymes (top). This setup allows the emergence of contraction waves from an almost homogeneous background ($t = 4, 16, 18, 22$). Taken from [16].

this setup, at a strong enough synchronisation strength ε, a dense assembly can exhibit wave propagation originating from a point source. See Figure 1.11. This wave propagation is carried by continuous changes in particle size instead of systematic migration of particles, which resembles the contraction wave patterns in biological tissues reported in [50] and [51].

1.2 From particles to fields

In this Section, we review the analytical and numerical methods used throughout the work in this thesis. In Subsection 1.2.1, we demonstrate the use of field theories in describing collective behaviours, in particular phase transitions. In Subsection 1.2.2, we show a systematic way of deriving field theories from microscopic models through coarse-graining.

1.2.1 Field theories from symmetries

In general, statistical field theories span an important framework of methods treating systems with large or infinitely large number of interacting degrees of freedom [10]. The application of field theories has permeated into statistical physics [59], condensed matter physics [60], random geometry [61], etc. In all these applications, collective modes dominate the system behaviours. The aim of applying field theories is to understand those behaviours, such as phase transitions, in terms of a small number of principles. A simple field-theoretic description usually should be local and is described in terms of an effective free energy

$$\beta\mathcal{F} = \int \mathrm{d}\mathbf{x}\Psi[\{\phi(\mathbf{x})\}], \tag{1.18}$$

with the Ψ-functional explicitly independent of $\mathbf{x}$.

Landau-Ginzburg field theory The form of the functional Ψ of fields $\{\phi(\mathbf{x})\}$, to be made simple, should be a polynomial expansion of fields and their gradients $\{\partial_{\mathbf{x}}\phi(\mathbf{x})\}$ [59]. Based on symmetry arguments, one may construct a field theory by keeping only lowest-order terms satisfying the underlying microscopic symmetries. An example is the renowned scalar *Landau-Ginzburg* (L-G) theory of phase transitions based on $\mathbb{Z}_2$-symmetry. Due to the $\mathbb{Z}_2$-symmetry, the Ψ-functional in L-G theory contains only terms of even powers in fields or their gradients. An isotropic L-G theory thus should bear

the form

$$\Psi[\phi(x)] = \frac{K}{2}(\partial_{\mathbf{x}}\phi(\mathbf{x}))^2 + \frac{t}{2}\phi(\mathbf{x})^2 + u\phi(\mathbf{x})^4 + \mathcal{O}\big(\phi^6\big) \tag{1.19}$$

In fact, to reveal phase transitions, a cutoff at ϕ^4-term is sufficient, thus rendering the L-G theory a so called ϕ^4-*theory*. Such a ϕ^4-theory contains only 3 coupling parameters K, t, u linked to microscopic details. Fixing the 3 parameters then fully characterises an L-G theory. To bound the value of ϕ, the ϕ^4-coupling parameter u has to be positive. Also, inhomogeneities penalises the effective free energy by contributing a positive gradient term and thus should be removed to minimise the effective free energy. It is then the sign of t, the quadratic coupling parameter, that determines the number of minima in the effective free energy. Continuously tuning t-value across 0 leads to a second-order phase transition featuring a change in the number of minima in $\mathcal{F}$. In the picture of a classical magnet system, where the field ϕ measures the global order, the splitting of the minimum at $\phi = 0$ into two minima at $|\phi| > 0$ signals a spontaneous ordering without the help of external fields. Such a spontaneous ordering breaks the underlying symmetry of $\mathcal{F}$ and is thus known as the *spontaneous symmetry breaking* (SSB). See Figure 1.12 (a).

The presence of an external field $h(\mathbf{x})$ amounts to adding a linear term $h(\mathbf{x})\phi(\mathbf{x})$ to the L-G functional $\Psi[\phi(\mathbf{x})]$. In the SSB regime, i.e. $t < 0$, the external field h determines the preferred direction of order. In the absence of inhomogeneities, a positive h stabilises the ordering in the negative direction, whilst a negative h promotes the ordering in the positive direction. Tuning h across 0 leads to an exchange between stabilities of the two minima in $\mathcal{F}$. This is interpreted as a first-order transition. See Figure 1.12 (b).

The L-G theory was first proposed to describe superconductivity transitions [62–64] from a macroscopic point of view, in contrast to the BCS-theory dedicated to microscopic details. In fact, it provides an effective field-theoretic description of a wide class of systems. In general, L-G theory does not have to be a scalar field theory. It also allows vector fields [64], tensor fields [65], etc. A scalar L-G theory describes liquid-gas transitions, binary mixtures and uniaxial magnets, whilst a vector L-G theory can describe superconductivity, superfluidity, planar magnets and classical magnets, depending on the dimension of vector fields [59]. Notably, the correspondence between an L-G theory and an Ising model can be explicitly built via a *Hubbard-Stratonovich* transform of the partition function of Ising model with a cutoff at ϕ^4-order [10].

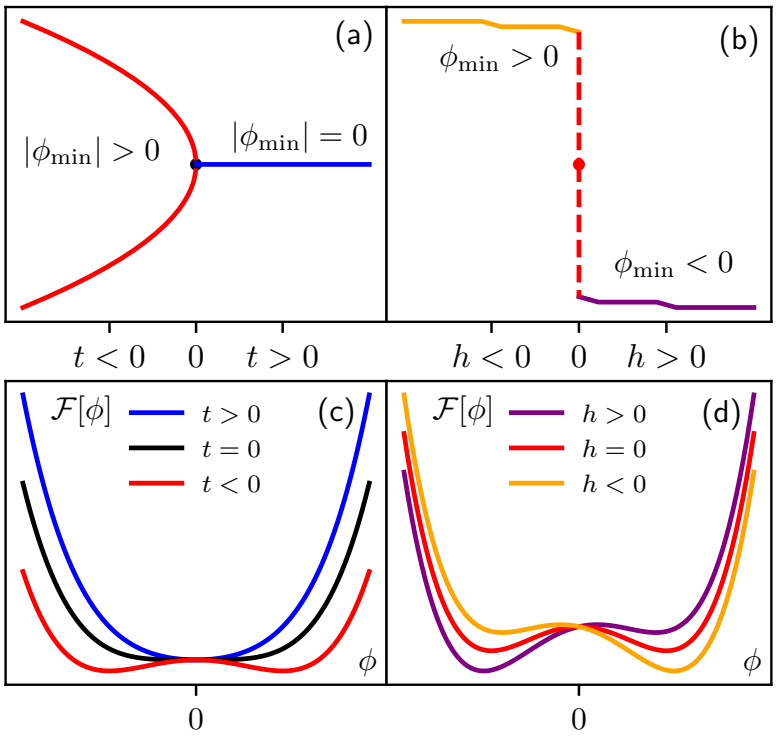

Figure 1.12: Effective free energies $\mathcal{F}$ of homogeneous fields ϕ and their global minima. (a) t determines the positions of minima $\phi_{\min}$. When $t < 0$, $\phi_{\min}$'s are always finite. When $t > 0$, $\phi_{\min}$ is zero. (b) When $t < 0$, the external field determines the sign of $\phi_{\min}$. When $h > 0$, $\phi_{\min}$ is negative. When $h < 0$, $\phi_{\min}$ is positive. (c) t determines the number of minima. When $t < 0$, two minima in $\mathcal{F}$ exist (red). When $t > 0$, only one single minimum occurs in $\mathcal{F}$. (d) When $t < 0$, the external field h determines the relative stabilities of the two minima. When $h > 0$, the minima at $\phi < 0$ is more stable. When $h < 0$, the minima at $\phi > 0$ becomes the global minimum.

Non-conserved and conserved dynamics: Model A and Model B There are two main classes of models describing the phase ordering kinetics of field theories [13]. They can be derived from a coarse-grained free energy $\mathcal{F}$. One is Model A describing non-conserved field dynamics

$$\partial_t \phi(\mathbf{r},t) = -M(\phi)\frac{\delta \mathcal{F}}{\delta \phi}\bigg|_{\phi(\mathbf{r},t)} + \sqrt{2M(\phi)T}\Lambda(\mathbf{r},t), \tag{1.20}$$

with Λ being a scalar field of Gaussian white noise satisfying $\langle \Lambda(\mathbf{r},t)\Lambda(\mathbf{r}',t')\rangle = \delta(\mathbf{r}-\mathbf{r}')\delta(t-t')$ and $M(\phi)$ being the field-dependent mobility. The other is Model B describing the dynamics of a conserved field

$$\partial_t \phi(\mathbf{r},t) = \partial_{\mathbf{r}}\left(M(\phi)\partial_{\mathbf{r}}\frac{\delta \mathcal{F}}{\delta \phi}\bigg|_{\phi(\mathbf{r},t)}\right) + \partial_{\mathbf{r}}\cdot[\sqrt{2M(\phi)T}\boldsymbol{\eta}(\mathbf{r},t)], \tag{1.21}$$

with $\boldsymbol{\eta}$ being a vector field of Gaussian white noise satisfying $\langle \eta^{\mu}(\mathbf{r},t)\eta^{\nu}(\mathbf{r}',t')\rangle = \delta^{\mu\nu}\delta(\mathbf{r}-\mathbf{r}')\delta(t-t')$. In Model B, the field ϕ can be any local order parameter field, such as the local density difference between species in a binary alloy or the local magnetisation in a spin model. Notably, in Model B, the noise field is a vector field, whilst in Model A, the noise field is a scalar field. In both classes of models based on the free energy $\mathcal{F}$, the probability measure of a field configuration ϕ in equilibrium is formally given as a Boltzmann distribution

$$\mathbb{P}[\phi] \propto e^{-\beta \mathcal{F}}, \tag{1.22}$$

where again $\beta = 1/T$ is the inverse temperature.

Pattern formation in field theories The collective macroscopic behaviours emerging from an assembly of microscopic units are often seen as dynamical patterns. The formation of these dynamical patterns exists in many contexts, including morphogenesis [66], colony growth [67], etc. The controls over those patterns are often interesting topics for understanding life processes.

Many patterns can be interpreted as instabilities of reaction-diffusion systems, namely the *Turing patterns* [68]. Turing patterns are common in chemistry and chemical engineering. For instance, in Prigogine's Brusselator model, the autocatalytic reactions give rise to Turing patterns [69]. In fact, autocatalysis often leads to chemical oscillations, namely *chemical waves* as an example of Turing pattern. A typical setup for chemical oscillations is the *Belousov–Zhabotinsky* (B-Z) reaction [70, 71], whose mechanism been intensively studied [72, 73].

In a more general context, the class of reaction-diffusion systems enabling

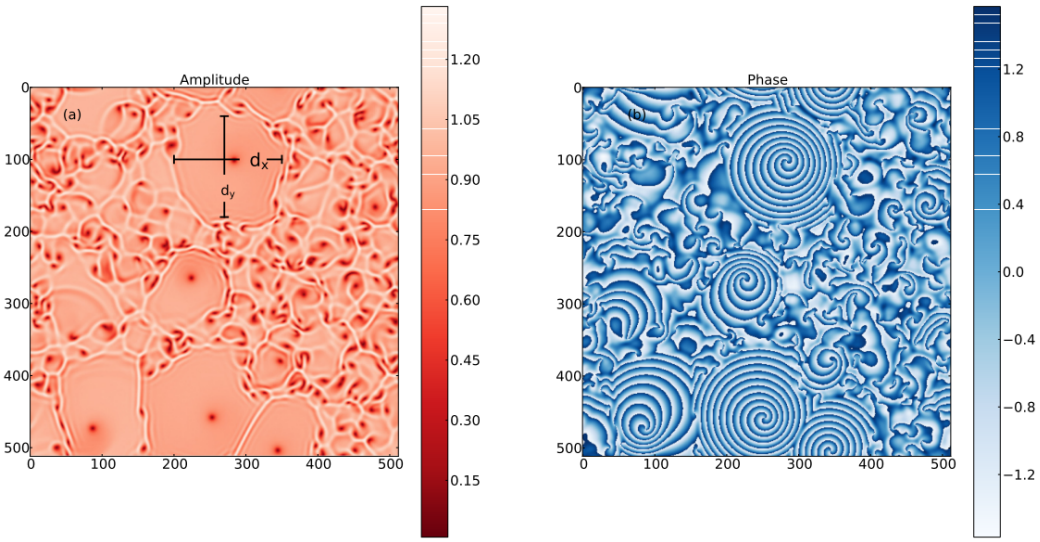

Figure 1.13: Snapshots of the amplitude field $|A|(\mathbf{r}, t)$ (a) and the phase field $\arg A(\mathbf{r}, t)$ (b) showing spiral wave patterns. The topological defects feature vanishing amplitude of A and are thus located at dark points in (a). Here $b = -3.5, c = 0.44$. Taken from [74].

patterns similar to chemical oscillations in the B-Z reaction can be captured under the framework of the *complex Ginzburg-Landau equation* (CGLE) [11]. The CGLE bears the general form

$$\partial_t A = A + (1 + b\mathrm{i})\partial^2_{\mathbf{rr}} A - (1 + c\mathrm{i})|A|^2 A, \tag{1.23}$$

where A is a complex-valued field defined on continuous space and time and $b, c \in \mathbb{R}$. In a bidimensional space with periodic boundary conditions in both dimensions, the nonlinear partial differential equation (PDE) (1.23) can lead to spiral wave patterns in the phase field of A [74]. See Figure 1.13.
The spiral wave patterns in Figure 1.13 exhibit topological defects around which the contour integrals $\oint \mathrm{d}\theta\,(\mathbf{r})$ of local phase increments $\mathrm{d}\theta$ are nonzero. The existence of such topological defects in fact has its origin in the spontaneous breaking of $U(1)$ symmetry $A \to Ae^{\mathrm{i}\Phi}$ of Equation (1.23). The spontaneous breaking of such a symmetry allows metastable interpolations between degenerate vacua distributed along the $U(1)$ group, which are topological defects [75].

1.2.2 Field theories via coarse-graining

Besides the approach adopted in the derivation of L-G theory, there is an exact derivation of field theories from particle-based models, namely a *bottom-up* approach, using the systematic coarse-graining approach *à la* Dean [20]. For simplicity, we begin with the Langevin equation (1.4) describing the motion of an overdamped particle in a many-body potential

$$\dot{\mathbf{r}}_i(t) = -\mu\partial_{\mathbf{r}_i}U + \sqrt{2D}\boldsymbol{\xi}_i(t), \tag{1.24}$$

where $U = \sum_i \sum_{j<i} V[\mathbf{r}_i(t) - \mathbf{r}_j(t)]$ and $\boldsymbol{\xi}_i$ is the noise of the i-th particle satisfying

$$\langle \xi_i^\alpha(t)\xi_j^\gamma(t')\rangle = \delta_{ij}\delta^{\alpha\gamma}\delta(t-t')\,\mathrm{d}t\,, \tag{1.25}$$

where α, γ denotes the vector components of the noise. Also, there is no self-interaction, i.e. $V = 0$ whenever $i = j$.
To find an exact equation describing the dynamics of the stochastic density field $\rho(\mathbf{r}, t)$, we start with an empirical distribution

$$\rho(\mathbf{r}, t) = \sum_i \rho_i(\mathbf{r}, t), \quad \rho_i(\mathbf{r}, t) = \delta(\mathbf{r} - \mathbf{r}_i(t)). \tag{1.26}$$

To find the differential equation of ρ, one has to look at a static macroscopic observable $O(\mathbf{r})$ as a compactly supported, smooth test function. One may find the time derivative of $\overline{O}(t) = \int \mathrm{d}\mathbf{r}\,\rho(\mathbf{r}, t)O(\mathbf{r})$, the average value of O measured by ρ

$$\begin{aligned}\dot{\overline{O}} = (\rho, \dot{O}) &= \sum_i (\rho_i, \dot{\mathbf{r}}\partial_{\mathbf{r}}O|_{\mathbf{r}=\mathbf{r}_i}) \\ &= \sum_i \left(\rho_i, -\mu\sum_{j\neq i}\partial_{\mathbf{r}}V[\mathbf{r} - \mathbf{r}_j(t)]\cdot\partial_{\mathbf{r}}O + D\partial^2_{\mathbf{rr}}O\right) + \sqrt{2D}\sum_i(\rho_i, \partial_{\mathbf{r}}O)\cdot\boldsymbol{\xi}_i,\end{aligned} \tag{1.27}$$

where $(A, B) = \int \mathrm{d}\mathbf{r}\,A(\mathbf{r})B(\mathbf{r})$ is the functional inner product between integrable functions $A(\mathbf{r}), B(\mathbf{r})$ and the last term is interpreted with Itô convention. Using integration by part we transfer the derivatives onto ρ:

$$\dot{\overline{O}} = \sum_i \left(\left[\mu\partial_{\mathbf{r}}\{\rho_i\sum_{j\neq i}\partial_{\mathbf{r}}V[\mathbf{r} - \mathbf{r}_j(t)]\} + D\partial^2_{\mathbf{rr}}\rho_i\right] - \sqrt{2D}\partial_{\mathbf{r}}\rho_i\cdot\boldsymbol{\xi}_i, O\right). \tag{1.28}$$

Another representation of $\dot{\overline{O}}$ formally involves the time derivative of ρ:

$$\dot{\overline{O}} = (\partial_t \rho, O) \tag{1.29}$$

A simple comparison between (1.28) and (1.29) leads to

$$\partial_t \rho = \mu \partial_{\mathbf{r}} \left\{ \rho \int \mathrm{d}\mathbf{R}\, \rho(\mathbf{R}, t) \partial_{\mathbf{r}} V(\mathbf{r} - \mathbf{R}) \right\} + D \partial^2_{\mathbf{rr}} \rho - \sqrt{2D} \sum_i \partial_{\mathbf{r}} \cdot (\rho_i \boldsymbol{\xi}_i). \tag{1.30}$$

The closure of (1.30) entails further treatment on the noise term which still contains information at single-particle level. Hence we define the *noise field*

$$\Lambda(\mathbf{r}, t) = -\sum_i \partial_{\mathbf{r}} \cdot [\rho_i(\mathbf{r}, t) \boldsymbol{\xi}_i]. \tag{1.31}$$

Clearly, the noise defined in (1.31) is Markovian. This is shown in its correlation function

$$\begin{aligned} \langle \Lambda(\mathbf{r}, t) \cdot \Lambda(\mathbf{R}, t') \rangle &= \delta(t - t') \sum_i \partial^2_{\mathbf{rR}} [\rho_i(\mathbf{r}, t) \rho_i(\mathbf{R}, t)] \\ &= \delta(t - t') \partial^2_{\mathbf{rR}} [\delta(\mathbf{r} - \mathbf{R}) \sum_i \rho_i(\mathbf{r}, t)] \end{aligned} \tag{1.32}$$

We then define another noise field

$$\Lambda' = \partial_{\mathbf{r}} \cdot [\boldsymbol{\xi}(\mathbf{r}, t) \rho^{\frac{1}{2}}(\mathbf{r}, t)] \tag{1.33}$$

where $\boldsymbol{\xi}(\mathbf{r}, t)$ is a spatially uncorrelated white noise

$$\langle \xi^\nu(\mathbf{r}, t) \xi^\gamma(\mathbf{R}, t') \rangle = \delta^{\nu\gamma} \delta(t - t') \delta(\mathbf{r} - \mathbf{R}) \tag{1.34}$$

One can immediately find that $\langle \Lambda(\mathbf{r}, t) \Lambda(\mathbf{R}, t') \rangle = \langle \Lambda'(\mathbf{r}, t) \Lambda'(\mathbf{R}, t') \rangle$, i.e. Λ and Λ' have identical spatio-temporal correlation functions. Thus they are equivalent at hydrodynamic level and are interchangeable. To close the hydrodynamic equation (1.30), one apply the hydrodynamic noise defined in (1.33) to arrive at

$$\partial_t \rho = \left(\mu \partial_{\mathbf{r}} \left\{ \rho \int \mathrm{d}\mathbf{R}\, \rho(\mathbf{R}, t) \partial_{\mathbf{r}} U(\mathbf{r} - \mathbf{R}) \right\} + D \partial^2_{\mathbf{rr}} \rho \right) + \sqrt{2D} \Lambda'(\mathbf{r}, t). \tag{1.35}$$

Equation (1.35) is a stochastic differential equation of density field ρ, which

is known at *Dean's equation*. The underlying free energy functional of Dean's equation (1.35) can be written as

$$\mathcal{F}[\rho] = \frac{1}{2}\int \mathrm{d}\mathbf{r}\mathrm{d}\mathbf{R}\rho(\mathbf{r},t)U(\mathbf{r}-\mathbf{R})\rho(\mathbf{R},t) + T\int \mathrm{d}\mathbf{r}\,\rho(\mathbf{r},t)\ln\rho(\mathbf{r},t), \quad (1.36)$$

up to a constant. In terms of the free energy $\mathcal{F}$, the Dean's equation (1.35) can be rewritten as

$$\partial_t\rho(\mathbf{r},t) = \mu\partial_{\mathbf{r}}\cdot\left(\rho(\mathbf{r},t)\partial_{\mathbf{r}}\frac{\delta\mathcal{F}}{\delta\rho}\bigg|_{\rho(\mathbf{r},t)}\right) + \sqrt{2D}\partial_{\mathbf{r}}\cdot(\boldsymbol{\xi}(\mathbf{r},t)\rho(\mathbf{r},t)^{\frac{1}{2}}), \quad (1.37)$$

which immediately reveals the conservation of particle number. In comparison to the conserved dynamics (1.21), one may readily identify that $M(\rho) = \mu\rho$ and recover the Boltzmann distribution (1.22) of the field configurations of ρ. In fact, the probability measure (1.22) can be obtained as the stationary solution of the Fokker-Planck equation of ρ-field configurations.

1.3 Numerical techniques

1.3.1 Particle-based many-body simulations

For each particle, we assume its state is described by a series of variables $\{s_\alpha(t)\}, \alpha = 1, 2, ...$ Each variable of the i-th particle is updated according to an equation of motion

$$\mathrm{d}s_i^\alpha(t) = \mathcal{F}_i^\alpha(\{s_i^\alpha(t)\})\,\mathrm{d}t + \sqrt{2D}\,\mathrm{d}W_i^\alpha\,. \quad (1.38)$$

On the right-hand side, one calculates the deterministic contribution within $\mathrm{d}t$ as the first term. The noise contribution within $\mathrm{d}t$ is calculated by randomly picking a unit-variance, zero-mean Gaussian random value $g_i^\alpha(t) \sim \mathcal{N}(0,1)$, such that $\mathrm{d}W_i^\alpha = g_i^\alpha(t)\sqrt{\mathrm{d}t}$. To efficiently simulate the dynamics without inappropriately large time step $\mathrm{d}t$, we apply an adaptive criterion for the choice of $\mathrm{d}t$: a threshold value Δ_o is chosen such that

$$\mathrm{d}t = \begin{cases} \mathrm{d}t_{\mathrm{input}} & \text{if}\max_{\alpha,i}\mathcal{F}_i^\alpha(\{s_i^\alpha(t)\})\,\mathrm{d}t < \Delta_o \\ \frac{\Delta_o}{\max_{\alpha,i}\mathcal{F}_i^\alpha(\{s^\alpha(t)_i\})} & \text{else} \end{cases}. \quad (1.39)$$

In practice we take $\mathrm{d}t_{\mathrm{input}} = 0.005, \Delta_o = 0.1$.

Force calculation During each step of update (1.38), the assignment of forces $\mathcal{F}_i^\alpha(\{s_i^\alpha(t)\})$, especially its two-body part, claims the most computational cost. To improve the efficiency, we divide the simulation box into square grids, and count only the interactions between particles in the same grid or in nearest-neighbouring grids, since the interactions are short-ranged. To ensure that no interactions are missed, two criteria should be satisfied by the grids:

- Each grid should be able to cover the largest particle existing during the simulation, taking into account that particle radii evolve in time.
- The simulation box should be splitted into **identical** grids.

To safely optimise the simulation performance, we chose the smallest integer $l \in \mathbb{N}_+$ that is no smaller than the largest possible particle radius and a simulation box size $L \in \mathbb{N}_+$ that is divisible by this integer, i.e. $l \equiv 0 \mod L$). Here and below, we assume a square simulation box. With the grid splitting above, the grids can be organised into an $n \times n$ matrix, where $n = L/l$, such that each position (x, y) in the simulation box can be classified into a grid indexed by (I, J), where $(I, J) = (\lfloor x/l \rfloor, \lfloor y/l \rfloor), I, J = 0, 1, 2, ..., n-1$. In this way, each particle $p_i(x_i, y_i)$ belongs to a grid $\mathfrak{g}(I_i, J_i)$, i.e. $p_i(x_i, y_i) \in \mathfrak{g}(I_i, J_i)$, and the whole simulation box becomes a set of grids $\{\mathfrak{g}\}$. The counting of pair interactions can then be demonstrated in Algorithm 1. By doing this the complexity is reduced to $\mathcal{O}(N \ln N)$ instead of $\mathcal{O}(N^2)$ where N is the number of particles in the simulation box [76]. See Figure 1.14.

1.3.2 Field simulations

We consider a reaction-diffusion system composed of hydrodynamic fields $\{f_i(\mathbf{r}, t)\}$ living on a bidimensional flat torus $\mathbb{T}^2$

$$\partial_t f_i = D_i \partial^2_{\mathbf{rr}} f_i + \mathcal{R}_i(\{f_j\}), i = 0, 1, ... \tag{1.40}$$

At each position $\mathbf{r}$, the value of f_i at time t should be updated by $f_i(\mathbf{r}, t+\mathrm{d}t) = f_i(\mathbf{r}, t) + \partial_t f_i \, \mathrm{d}t$. Here we adopt the *pseudo-spectral method*, namely the *spectral method* on a torus, by splitting the timestep $\mathrm{d}t$ into two halves. In the first half $\mathrm{d}t/2$, we consider the diffusion part in Fourier q-space using the *semi-implicit* method.

$$\tilde{f}_i(\mathbf{q}, t + \frac{\mathrm{d}t}{2}) = \tilde{f}_i(\mathbf{q}, t) - D_i q^2 \frac{\tilde{f}_i(\mathbf{q}, t) + \tilde{f}_i(\mathbf{q}, t + \frac{\mathrm{d}t}{2})}{2} \frac{\mathrm{d}t}{2} \tag{1.41}$$

which leads to $\tilde{f}_i(\mathbf{q}, t+\mathrm{d}t/2) = \frac{4 - D_i \mathbf{q}^2 \mathrm{d}t}{4 + D_i \mathbf{q}^2 \mathrm{d}t} \tilde{f}_i(\mathbf{q}, t)$. Then we consider the reaction parts in real space, using the field configurations at time $t + \mathrm{d}t/2$. See Algorithm 3.

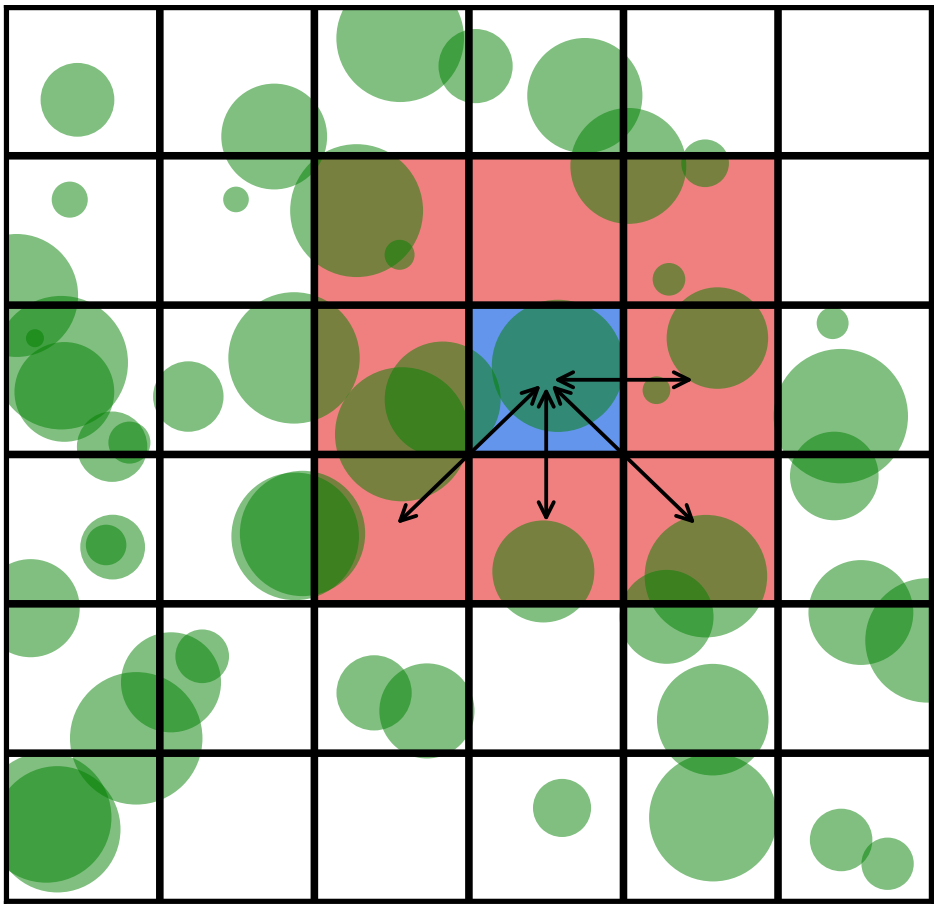

Figure 1.14: Schematic illustration of force assignment in each step of particle-based simulations. The simulation box is divided into identical square grids, which are larger than the largest particle existing during the whole simulation. Complete assignment of pair forces is realised by looping over the grids. For instance, on each particle in the blue grid, pair forces are exerted by particles in half of the neighbouring grids (red) and the other particles in the same grid (blue).

Algorithm 1: Counting of pair interactions

Data: null
Result: Pair interactions $\{\mathcal{F}_{ij}\}$

```
/* Initialise all pair interactions with zeros                    */
{F_ij} ← {0.};
/* Iterate over grids                                             */
for ( g(I, J) ∈ {g} ) {
    /* Iterate over particles in the grid g(I, J)                 */
    for ( p_i ∈ g(I, J) ) {
        /* Iterate over other particles in the same grid          */
        /* The subset {p_j} should be adapted to avoid repeated
           counting                                                */
        for ( p_j ∈ {p_j} ⊂ g(I, J) ) {
            Update F_ij ;                          // See Algorithm 2
        }
        /* Iterate over particles in the right neighbouring grid  */
        for ( p_j ∈ g(I + 1, J) ) {
            Update F_ij ;                          // See Algorithm 2
        }
        /* Iterate over particles in the lower-right neighbouring
           grid                                                    */
        for ( p_j ∈ g(I + 1, J + 1) ) {
            Update F_ij ;                          // See Algorithm 2
        }
        /* Iterate over particles in the lower neighbouring grid  */
        for ( p_j ∈ g(I, J + 1) ) {
            Update F_ij ;                          // See Algorithm 2
        }
        /* Iterate over particles in the lower-left neighbouring
           grid                                                    */
        for ( p_j ∈ g(I − 1, J + 1) ) {
            Update F_ij ;                          // See Algorithm 2
        }
    }
}
```

Algorithm 2: Updating $\mathcal{F}_{ij}$

Data: $p_i, p_j, \mathcal{F}_{ij}$
Result: $\mathcal{F}_{ij}$
$r_{ij}^2 \leftarrow (x_i - x_j)^2 + (y_i - y_j)^2$; // Calculate the pair distance
if $(R_i + R_j)^2 \geq r_{ij}^2$ **then**
  $\mathcal{F}_{ij} \leftarrow \mathcal{F}_{ij} + f(p_i, p_j)$; // Calculate the contribution $f(p_i, p_j)$ iff the particles overlap
else
  continue;
end

Algorithm 3: Updating $\{f_i(\mathbf{r}, t)\}$

Data: $\{f_i(\mathbf{r}, t)\}$
Result: $\{f_i(\mathbf{r}, t + \mathrm{d}t)\}$
/* First halfstep: update with the diffusion parts in q-space */
for ($f_i \in \{f_i\}$) {
  $\tilde{f}_i(\mathbf{q}, t) \leftarrow \int_{\mathbb{T}^2} \mathrm{d}\mathbf{r}\, f_i(\mathbf{r}, t) e^{-\mathrm{i}\mathbf{q}\cdot\mathbf{r}}$;
  $\tilde{f}_i(\mathbf{q}, t + \mathrm{d}t/2) \leftarrow \frac{4 - D_i \mathbf{q}^2 \mathrm{d}t}{4 + D_i \mathbf{q}^2 \mathrm{d}t} \tilde{f}_i(\mathbf{q}, t)$;
  $f_i(\mathbf{r}, t + \mathrm{d}t/2) \leftarrow \int_{\mathbb{T}^2} \mathrm{d}\mathbf{q}\, \tilde{f}_i(\mathbf{q}, t + \mathrm{d}t/2) e^{\mathrm{i}\mathbf{q}\cdot\mathbf{r}}$;
}
/* Second halfstep: update with the reaction parts in real space */
for ($f_i \in \{f_i\}$) {
  $f_i(\mathbf{r}, t + \mathrm{d}t) \leftarrow f_i(\mathbf{r}, t + \mathrm{d}t/2) + \mathcal{R}_i(\{f_i(\mathbf{r}, t + \mathrm{d}t/2)\})\, \mathrm{d}t/2$;
}

Chapter 2

Pulsating Active Matter

In this chapter, we propose a new class of active matter, namely *pulsating active matter* (PAM), as a particle-based scheme that mimics the behaviours of biological cells in living tissues. Being alive, those biological cells repetitively deform, driven and sustained by ATP hydrolysis [77]. In addition to individual deformations, living cells interact with each other, resulting in macroscopic patterns such as contraction waves propagated by cell deformations without prerequisiting significant displacement of cells [9, 50]. We therefore consider a dense assembly of soft repulsive disk particles. Those soft particles are individually driven to deform through their activities. The active drive in particle motility is neglected in our model. Our particle-based simulations reveal that in a dense assembly, the competition between repulsion and size synchronisation between neighbouring particles yields dynamical patterns including planar waves, circular waves, spiral waves and defect turbulence, which are then propagated by active periodic deformation of particles. We investigate the underlying mechanism of these patterns' emergence together with the nature of transitions in detail. In the continuum limit, we systematically derive a field-theoretic description and compare it to reaction-diffusion systems (RDS).
This Chapter is organised as follows: in Section 2.1, we introduce the background of this work. In Section 2.2, we describe our particle-based model. In Section 2.3, we present the dynamic patterns and quantitative measurements in particle-based simulations. In Section 2.4, we derive our field theory and present the results of field-theoretic analysis. In Section 2.5, we discuss our results and provide future extensions of our work.
This work is reported in arXiv:2208.06831

2.1 Introduction

Active matter is a class of systems in non-equilibrium statistical mechanics that is well-known for the energy input that drives the individual members at a microscopic level [29]. The individual activities give rise to interacting many-body dynamics, leading to a non-equilibrium regime where unique collective behaviours emerge, which are not observed in equilibrium.
Very often, activity is interpreted as self-propulsion, where each particle is driven to undergo translational motion. These self-propelled particles can exhibit various collective behaviours such as flocking [34] and/or MIPS [44], to name a few. In dense systems, self-propulsion is found to shift the glass transition [78, 79]. In cellular tissue models, the solid-fluid transition is also regulated by the self-propulsion activities, with the area of each cell being constrained [5, 80].
In biological tissues, unlike bacteria, living cells consume energy for deformation and migration. Through these active deformations, cell sizes repetitively grow and shrink within a bounded range. These deformations are locally correlated: within a short range, cell sizes tend to be close to each other and change over time collectively [48, 81]. In compact spaces, the close packing of cells results in the coexistence of expansion and contraction: Whilst in some regions cells' sizes decrease, in other regions cells have to grow larger. With this origin, contraction waves propagate in living tissues, as have been observed experimentally both *in vivo* [82–84] and *in vitro* [3, 4, 48, 50, 51, 81, 85, 86].
Indeed, contraction waves play a crucial role in biology. During the early stages of embryonic development, morphogenesis is driven by contraction waves, which result from mechanochemical coupling [87–89]. In cardiac tissues, cell contractions triggered by electric signals lead to self-organised patterns facilitated by mechanical interactions [90–92]. Some of these patterns are associated with arrhythmogenesis [93, 94], which is crucial for medical practitioners. In uterine tissues, such contractions occur during labour and are regulated by electromechanical couplings [95, 96]. Understanding the emergence and control of the contraction-induced patterns hence provides a basis for developing advanced techniques of treatment for the corresponding health issues.
Our approach to understanding these patterns involves proposing a simple yet effective model. Indeed, various models have been developed to study these patterns, such as particle-based [54, 86] and continuum [55, 56] models. However, assigning activity drives to both translation and active deformation of cells is non-intuitive, since in a dense tissue, cells seldom migrate. Some preliminary efforts have explored assigning activities to particle deformations

to achieve novel phenomenologies distinct from self-propelled particles [15–17, 97, 98]. These studies indicate that active deformation plays a crucial role in the emergence of collective patterns in living tissues. In our work, we introduce a new class called pulsating active matter (PAM) as an extension of existing active matter classes. Our results reveal that active pulsation at individual level creates a plethora of dynamical patterns.

2.2 Model description

In this work, a dense assembly of N deforming spherical particles in a bidimensional square box of size L with periodic boundary conditions in both dimensions is considered. Each particle is characterised by its position $\mathbf{r}$ together with its phase θ, an internal state. The size σ of each particle is determined by its phase θ

$$\sigma(\theta) = \sigma_0 \frac{1 + \lambda \sin\theta}{1 + \lambda}, \tag{2.1}$$

where $\sigma_0, \lambda > 0$ are input parameters defining the upper bound and range of possible particle sizes respectively.
These particles are subject to short-range two-body repulsions U and synchronisations $\mathcal{T}$ with cutoffs being determined by particle sizes. We then consider a locally rescaled dimensionless two-body distance a_{ij} between particles i and j

$$a_{ij} = \frac{|\mathbf{r}_i - \mathbf{r}_j|}{\sigma(\theta_i) + \sigma(\theta_j)}. \tag{2.2}$$

Locally, between particles i and j, the two-body interactions composed of repulsion and synchronisation, are turned on iff they share a non-vanishing overlap, i.e. $a_{ij} < 1$, see Figure 2.1. With this criterion, the particle-based equations of motion can be written down

$$\begin{aligned} \dot{\mathbf{r}}_i &= -\mu \sum_{j=1}^{N} \partial_{\mathbf{r}_i} U(a_{ij}) + \sqrt{2\mu T}\, \boldsymbol{\xi}_i \\ \dot{\theta}_i &= \omega - \sum_{j=1}^{N} \Big[\mathcal{T}(a_{ij}, \theta_i - \theta_j) + \mu_\theta \partial_{\theta_i} U(a_{ij}) \Big] + \sqrt{2\mu_\theta T}\, \eta_i, \end{aligned} \tag{2.3}$$

in which particle translation follows an overdamped Langevin equation with a unit-variance, zero-mean Gaussian white noise $\boldsymbol{\xi}$ on each particle. More ingredients exist in the phase dynamics where, besides the contribution from

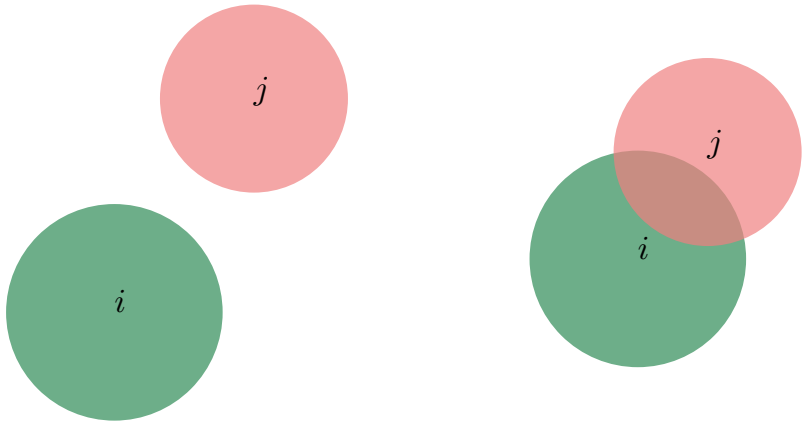

Figure 2.1: Scheme of two particles i and j showing the implications of a_{ij} values. $a_{ij} < 1$ iff particles i and j overlap with each other, which is sufficient and necessary for them to interact with each other.

pair repulsion $\sum_j \mu_\theta \partial_{\theta_i} U(a_{ij})$ and a unit-variance, zero-mean Gaussian white noise η_i, there are synchronisations $\mathcal{T}(a_{ij}, \theta_i - \theta_j)$ driven by phase differences between neighbouring particles i and j, which is intrinsically non-equilibrium since the neighbours alter in time. In this work, the synchronisation bears the form

$$\mathcal{T}(a_{ij}, \theta_i - \theta_j) = \varepsilon \sin(\theta_i - \theta_j)\Theta(1 - a_{ij}), \tag{2.4}$$

such that it encourages the synchronisation in particle sizes $\sigma(\theta_i)$ and $\sigma(\theta_j)$. Notice that $\mathcal{T} = 0$ whenever $i = j$, since there is no self-interaction. The intensity of synchronisation is measured by an input parameter ε. The interaction range is defined by the Heaviside kernel Θ.
Besides, it is the active drive ω exclusively in phase dynamics that highlights the novelty of this class of active matter. As an input parameter, it is in this work fixed and identical for all particles. It is immediate from (2.1) that the active drive ω encourages periodic deformation of particles within a bounded interval $[\sigma_0(1 - \lambda)/(1 + \lambda), \sigma_0]$.
Based on such a setup, the particle-based simulations are performed. Here the Weeks-Chandler-Andersen (WCA) potential is adopted as the pure repulsive potential U in the model

$$U(a) = U_0(a^{-12} - 2a^{-6})\Theta(1 - a), \tag{2.5}$$

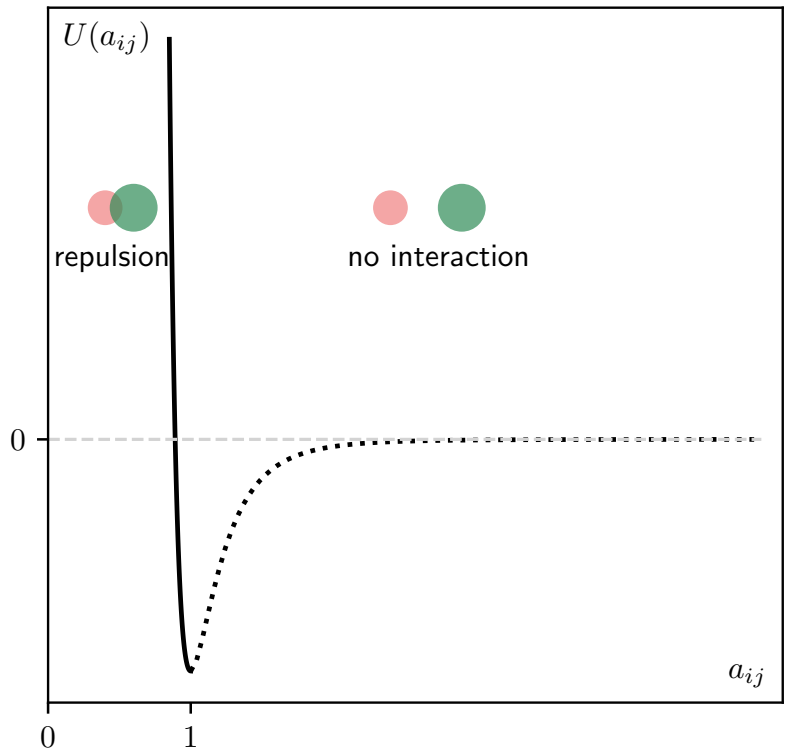

Figure 2.2: Schematic illustration of the WCA potential $U(a_{ij})$. Effectively, its is the repulsive part of a 12-6 Leonard-Jones potential achieved by cutoff at its minimum. This cutoff is set to $a_{ij} = 1$ such that the two particles are just in contact with each other. When the two particles i and j overlap, i.e. $a_{ij} < 1$, they reduce the overlap by both repelling each other and reducing the sizes. When the two particles do not overlap, i.e. $a_{ij} > 1$, there are no interactions between them.

where U_0 measures the strength of repulsion as an input parameter. See Figure 2.2. Again, $U(a_{ii}) = 0$ for all i such that self-interactions are exempted.

2.3 Patterns and phase diagrams

Beyond the initial observation of contraction wave propagation in [16], 4 classes of wave patterns in all are observed in simulations as steady states, see Figure 2.3. The defects are defined as points in space around each of which $\frac{1}{2\pi} \oint_C \mathrm{d}\theta\,(\mathbf{r}) = \pm 1$, with C being any single-loop contour containing no other defect points and $\theta(\mathbf{r})$ the local average phase of particles in the vicin-

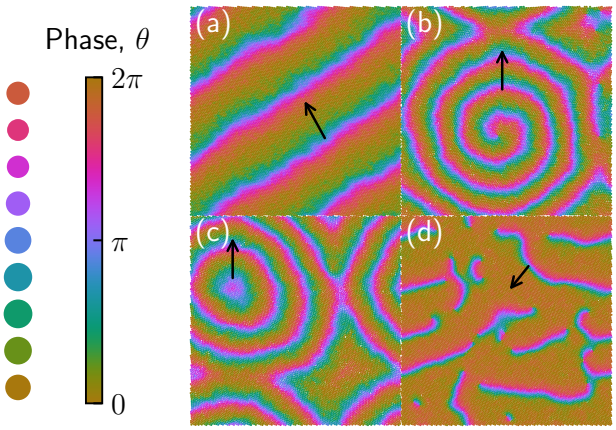

Figure 2.3: A dense assembly of particles with pulsating sizes can yield 4 classes of contraction wave patterns: (a) planar waves, (b) spiral waves, (c) circular waves and (d) turbulent waves. The depicted waves propagate in the directions of black arrows. The underlying particle-based simulations are carried out in a square box of edge length $L = 100\sigma_0$, with $\mu = 1, \mu_\theta = 1, T = 1, \omega = 10, \sigma_0 = 1, U_0 = 1$. The parameter values $\{\rho_0, \varepsilon, \lambda\}$ for the snapshots are (a) $\{1.7, 10, 0.05\}$, (b) $\{1.6, 10, 0.1\}$, (c) $\{1.65, 10, 0.1\}$ and (d) $\{1.8, 16, 0.1\}$. The particle-based systems are all initialised with uniformly distributed particle positions in $[0, L] \times [0, L]$ and uniformly distributed particle phases in $[-\pi, \pi]$.

ity of $\mathbf{r}$. The defects here do not characterise the number of neighbouring particles. Amongst the 4 classes, two of them (planar, circular) are defectless. The spiral waves originate from one defect (source) and are absorbed by the other (sink). In a steady state featuring spiral waves, only a pair defects exist, carrying opposite topological charges, such that they sum up to zero, as is required on a compact surface without boundary. The turbulent waves, unlike the spiral waves and defectless waves, are composed of short wave segments. These wave patterns realised with our model extends the observations by Togashi [16]. Recently, the emergence of wave patterns via mechanochemical coupling are also realised using self-propelled vertex models [9], in which the planar waves are also observed.

These patterns are reminiscent of those in reaction-diffusion systems (RDS), but with a major difference: unlike in RDS, in our model, the wave patterns have only mechanical origin, independent of chemical reactions. In fact, from the particle-based description (2.3) of the model, one can clearly see that the repulsion U reduces the overlap between particles. In the equation of particle positions, it reduces the overlap by driving the overlapping particles

to enlarge the distance between them. In the equation of particle phases, it impedes particles' growth when they are in direct contact. These effects are particularly significant in a dense assembly, where the majority of particles overlap with each other. Whilst synchronisations $\mathcal{T}$ contribute to the unification of particle sizes, the repulsion U would charge the global synchronisation of particle sizes a considerable energy cost if all particles were driven to reach their maximal size σ_0. To reduce the repulsive energy cost to a reasonable level, a compromise that allows partial synchronisation of particle sizes within a finite length scale is reached. This compromise actually leads to wave patterns. The propagation of these wave patterns are driven by ω which leads to the periodic and locally synchronous deformation of particles. In this way, the particles "take turn to grow" instead of growing together.
What are the conditions for this to happen? Answering this question entails exploring the phase diagram. The first phase diagram is measured in terms of the *synchronisation order parameter* r defined as

$$r = \frac{1}{N}\left\| \sum_{j=1}^{N} e^{\mathrm{i}\theta_j} \right\|. \tag{2.6}$$

This order parameter is analogous to the magnetisation moment in spin models, and is broadly used in Kuramoto-type models [58, 99]. In the phase diagram, the averages $\langle r \rangle$ of the synchronisation order parameter are measured in steady states of different input parameters. The main controlling parameters here are the synchronisation strength ε and the number density of particles ρ_0.
The results of measurement are shown in Figure 2.4. In Figure 2.4 (a), the phase diagram is composed of 4 regions as the result of varying the control parameters ε, ρ_0: two regions with $\langle r \rangle$-value close to 1, indicating highly ordered phases [(high ε, low ρ_0) and (high ε, high ρ_0)], one region with $\langle r \rangle$-value close to zero, corresponding to a disordered phase (low ε, low ρ_0), and one region with intermediate $\langle r \rangle$-values, accounting for wave phases (high ε, medium ρ_0). In the context of this model, this intermediate value of r between 0 and 1 means wave propagation which demonstrates local order yet lack of global order.
At low density (typically $\rho_0 < 1.4$) and strong synchronisation strength (typically $\varepsilon > 10$), the highly ordered phase with $\langle r \rangle$-value close to unity features globally synchronised cycling of particle deformation. Driven by a uniform ω, all particles in a dense assembly grow and shrink collectively. This globally ordered *cycling phase* may be broken by increasing the density ρ_0. In this way, the system becomes more packed, with the repulsive energy cost for a globally collective growth of particles being dramatically increased. Besides,

the cycling phase may be reached at low density ρ_0 from the disordered phase by simply increasing the synchronisation strength ε.
The region of the globally cycling phase has a boundary that is non-monotonic in density ρ_0, see the dark red and dark blue lines in Figure 2.4 (a). During the transition from the cycling phase to the phase allowing propagating waves, the competition between synchronisation and repulstion plays the major role. To make qualitatively comparison, one may scale $U \sim \rho_0^6, \mathcal{T}(a_{ij}, \theta_j - \theta_i) \sim \varepsilon$ to reach a qualitative comparison $\varepsilon \sim \rho_0^6$ that indicates a sharp monotonic increase in ρ_0, which is the case for the phase boundary. See the dark red line in Figure 2.4 (a).
At low density, where particle overlaps are minor, the transition between the disordered phase and the cycling phase is the result of the competition between synchronisation and noise. From the equation of motion of phases in Equation (2.3), one may extract a rough scaling argument $\sum_j \mathcal{T}(a_{ij}, \theta_j - \theta_i) \sim \varepsilon\rho_0$ to be compared with the noise, the effect of which is measured by $\mu_\theta T$. The comparison $\varepsilon\rho_0 \sim \mu_\theta T$ qualitatively recovers the monotonically decreasing shape of the phase boundary at low density. See the dark green line in Figure 2.4 (a).
With a further increased density (typically $\rho > 1.85$), the particle assembly becomes globally ordered again. Unlike the cycling phase, here the cyclic deformations of particles are completely hindered by the strong repulsion between neighbouring particles, due to deep overlaps between them. Synchronisation here helps maintain the order by suppressing the effect of noise on particle deformations. This phase is *arrested*. To achieve this phase, any synchronisation strengths above a low threshold value can be sufficient, regardless of the density values as long as the assembly is packed enough. This explains the almost vertical shape of the phase boundary of the arrested phase. See dark blue line in Figure 2.4 (a).
Beyond displaying the phases, we investigate the orders of phase transitions. With different monotonicities of the phase boundary, the underlying mechanisms of transitions are not identical. At high ε, the transition breaking the global order is clearly discontinuous. In Figure 2.4 (b), the probability distribution $\mathcal{P}$ of synchronisation order parameter r in steady states are measured for different ε-values across the phase boundary at a fixed density $\rho_0 = 1.3$. Around the phase boundary, there are clear bimodal patterns in $\mathcal{P}(r)$, indicating the dynamic coexistence of the cycling phase and the wave phase as steady states of different realisations. The discontinuous nature is further confirmed by the strong hysteresis when crossing the phase boundary by slowly tuning ε in steady states. In contrast, at $\rho_0 = 0.8$, the phase transition is continuous, since the unimodel shape of $\mathcal{P}(r)$ is maintained during the transition and no hysteresis exists during the transition. See Figure 2.4

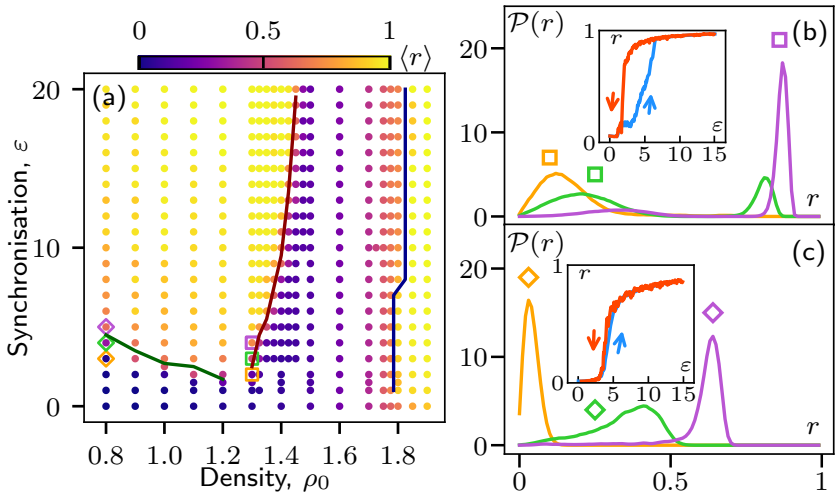

Figure 2.4: Phase diagram and phase transitions in particle-based dynamics. (a) Phase diagram of the synchronisation order parameter $\langle r \rangle$ as a function of synchronisation strength ε and particle number density ρ_0. The $\langle r \rangle$-value at each point is an average over 100 fully relaxed trajectories. Two highly ordered phase with $\langle r \rangle$ close to 1 are detected, with the rest part being disordered or partially ordered. Three phase boundaries are drawn as approximate positions of phase transitions, and are marked in different colours. The propagating wave patterns shown in Figure 2.3 exist between the dark red boundary and the dark blue boundary at high ε. (b) Probability distributions $\mathcal{P}$ of steady-state synchronisation order parameters r at $\rho_0 = 1.3$. During the transition by tuning ε, bimodal shapes of $\mathcal{P}(r)$ exist around the dark red phase boundary. The hysteresis during the transition [inset] further confirms that this transition is discontinuous. (c) Probability distributions $\mathcal{P}$ of steady-state synchronisation order parameters r at $\rho_0 = 0.8$. During the transition by tuning ε, unimodal shapes of $\mathcal{P}(r)$ are maintained when crossing the dark green phase boundary. The lack of hysteresis during the transition [inset] further confirms that this transition is continuous. All measurements are performed in a square box of edge length $L = 100\sigma_0$ with the other parameter values fixed at $\mu = 1, \mu_\theta = 1, T = 1, \omega = 10, \sigma_0 = 1, U_0 = 1$ and $\lambda = 0.05$. The particle-based systems are all initialised with uniformly distributed particle positions in $[0, L] \times [0, L]$ and uniformly distributed particle phases in $[-\pi, \pi]$, and relax for at least $t_{\text{ini}} = 5 \times 10^5\, \mathrm{d}t$. For each point in (a), the $\langle r \rangle$-value is averaged over at least 20 trajectories with a length of $8 \times 10^4\, \mathrm{d}t$ each. Close to the phase boundaries, the averages are over at least 100 trajectories. In (b) and (c), each $\mathcal{P}(r)$ is averaged over 400 trajectories and the hysteresis curves are averaged over 10 long trajectories for each direction.

(c).
The synchronisation order parameter r, as an analogy to magnetisation moment in spin models, characterises only the averaged order of steady-state configurations with a fixed setup. Beyond the ordering, a dimensionless *current* ν is defined to measure the average instantaneous phase speed

$$\nu(t) = \frac{1}{N\omega} \sum_{i=1}^{N} \dot{\theta}_i(t). \tag{2.7}$$

Following the definition of current (2.7), one may plug in the equation of motion of phase to obtain

$$\begin{aligned} \nu(t) &= 1 - \frac{1}{N\omega} \sum_{i=1}^{N} \sum_{j=1}^{N} [\mathcal{T}(a_{ij}, \theta_j - \theta_i) + \mu_\theta \partial_{\theta_i} U(a_{ij})] + \frac{\sqrt{2\mu_\theta T}}{N\omega} \sum_{i=1}^{N} \eta_i \\ &= 1 - \frac{\mu_\theta}{N\omega} \sum_{i=1}^{N} \sum_{j=1}^{N} \partial_{\theta_i} U(a_{ij}) + \frac{\sqrt{2\mu_\theta T}}{N\omega} \sum_{i=1}^{N} \eta_i, \end{aligned} \tag{2.8}$$

where we utilise $\mathcal{T}(a_{ij}, \theta_j - \theta_i) = -\mathcal{T}(a_{ji}, \theta_i - \theta_j)$. From Equation (2.8), it is straightforward that the current magnitude is only influenced by the repulsion between particles. In fact, at low densities where the repulsion is not major, the average values of current are all close to unity, no matter the configuration is ordered or disordered. It is only when the particle assembly becomes highly crowded that the average current becomes lower. In the arrested phase where the system is tightly packed, the average current is reduced to zero. These observations agree with Equation (2.8) in terms of the hindering effect of repulsion U on current. See Figure 2.5.
To extract further insights into the current ν, one may apply the product rule on $\partial_{\theta_i} U$ by introducing the *global packing fraction*

$$\varphi = \pi \sum_{j=1}^{N} \left(\frac{\sigma(\theta_j)}{L} \right)^2 \tag{2.9}$$

as an intermediate variable, such that

$$\partial_{\theta_i} U \simeq (\partial_{\theta_i} \varphi)(\partial_\varphi U). \tag{2.10}$$

At mean-field level, which is a reasonable approximation in the cycling phase, the factor $\partial_\varphi U$ can be approximated to be $\{\theta_i\}$-independent, and is clearly positive definite. Considering the definition of φ and σ in Equations (2.9)

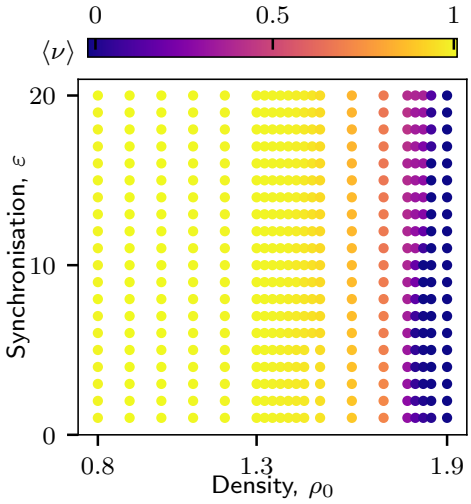

Figure 2.5: Phase diagram of the average current $\langle\nu\rangle$ as a function of synchronisation strength ε and particle number density ρ_0. The $\langle\nu\rangle$-value at each point is an average over 100 fully relaxed trajectories. In the arrested phase, the $\langle\nu\rangle$-value is close to 0. In other phases, $\langle\nu\rangle$-value is close to 1. Entering the arrested phase features a monotonic gradual decrease in $\langle\nu\rangle$-value with increasing density ρ_0. All measurements are performed in a square box of edge length $L = 100\sigma_0$ with the other parameter values fixed at $\mu = 1, \mu_\theta = 1, T = 1, \omega = 10, \sigma_0 = 1, U_0 = 1$ and $\lambda = 0.05$. The particle-based systems are all initialised with uniformly distributed particle positions in $[0, L] \times [0, L]$ and uniformly distributed particle phases in $[-\pi, \pi]$, and relax for at least $t_{\text{ini}} = 5 \times 10^5\, \mathrm{d}t$. For each point , the $\langle\nu\rangle$-value is averaged over at least 20 trajectories with a length of $8 \times 10^4\, \mathrm{d}t$ each.

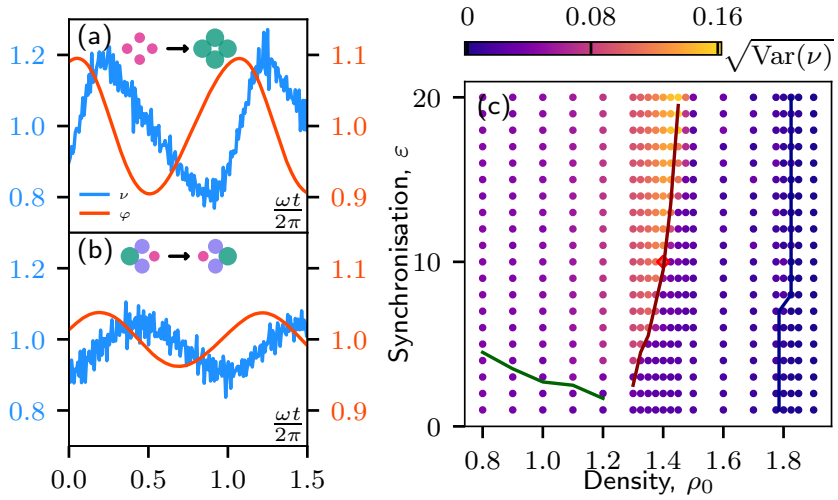

Figure 2.6: (a) Plots of measured current ν (blue) and global packing fraction φ (red) in time in a cycling steady state reached by a point on the phase boundary [red diamond in panel (c)] in a single trajectory. (b) Plots of measured current ν (blue) and global packing fraction φ (red) in time in a steady state with waves reached by a point on the phase boundary [red diamond in panel (c)] in a single trajectory. (c) Phase diagram of $\mathrm{Var}(\nu)$. In both (a) and (b), both ν and φ are oscillating, with a phase shift around $\pi/2$ between them. The oscillation amplitudes in a cycling steady state (a) are larger than in a partially ordered steady state (b). Both (a) and (b) are measured at a same point (red diamond) in the phase diagram (c). In the phase diagram (c), $\sqrt{\mathrm{Var}(\nu)}$ changes abruptly across the phase boundary (dark red) between the cycling phase and the partially ordered phase. All measurements are performed in a square box of edge length $L = 100\sigma_0$ with the other parameter values fixed at $\mu = 1, \mu_\theta = 1, T = 1, \omega = 10, \sigma_0 = 1, U_0 = 1$ and $\lambda = 0.05$. The particle-based systems are all initialised with uniformly distributed particle positions in $[0, L] \times [0, L]$ and uniformly distributed particle phases in $[-\pi, \pi]$, and relax for at least $t_{\mathrm{ini}} = 5 \times 10^5\, \mathrm{d}t$. For each point in (c), the $\sqrt{\mathrm{Var}(\nu)}$-value is averaged over at least 20 trajectories with a length of $8 \times 10^4\, \mathrm{d}t$ each. Close to the phase boundaries, the averages are over at least 100 trajectories.

and (2.1) respectively, one can find that $\partial_{\theta_i} U$ effectively becomes a periodic function of θ_i. The noise term being neglected, the product rule (2.10) together with the mean-field approximation leads to

$$\nu(t) \simeq 1 - \frac{\mu_\theta \partial_\varphi U}{\omega} \sum_{i=1}^{N} \partial_{\theta_i} \varphi \simeq 1 - \frac{\mu_\theta \partial_\varphi U}{\omega^2} \dot{\varphi}. \tag{2.11}$$

Here we also approximated $\partial_{\theta_i} \varphi \simeq (1/N)\dot{\varphi}/\dot{\theta}_i$ at mean-field level, with $\dot{\theta}_i$ being approximated to ω at the zeroth order.
Equation (2.11) can be used to explain the results on current ν shown in Figure 2.6. In Figure 2.6 (a)(b), currents of a cycling steady state (a) and a steady state (b) in which waves emerge are plotted together with the corresponding global packing fractions as functions of the rescaled dimensionless time $\omega t/2\pi$. In both steady states, both ν and φ are oscillating, with an almost constant phase shift of $\pi/2$ between them. This agrees with the linear relationship between $\nu(t)$ and $\dot{\varphi}$. Moreover, when φ is increasing, the repulsion hinders its growth by reducing the current ν, leading to ν-values below 1. This is reflected in Equation (2.11) since whenever $\dot{\varphi} > 0$, $\nu(t) < 1$. On the contrary, the reduction of φ is always encouraged by repulsion U in that it accelerates the shrinkage by increasing the current ν. This is also reflected in Equation (2.11) since whenever $\dot{\varphi} < 0$, $\nu(t) > 1$.
Between Figure 2.6 (a) and (b), the most distinguished differences lie in the oscillation amplitudes of ν and φ. Whilst the average values are almost identical, a cycling steady state leads to significantly higher oscillation amplitudes of ν and φ. Indeed, in a cycling phase, the globally synchronised growth and shrinkage of particles maximises the difference in φ at different times, whilst during the wave propagation a compromise is reached to allow the spatial coexistence of particles' growth and shrinkage, such that less changes in φ are observed. Due to the reduced magnitudes of $\dot{\varphi}$, the deviation of ν from unity is also systematically reduced.
It is then reasonable to regard the oscillation amplitude of ν as a discriminating criterion between the cycling phase and the partially ordered phase. The oscillation amplitude can be captured by the current variance $\mathrm{Var}(\nu) = \langle \nu^2 \rangle - \langle \nu \rangle^2$, the square root of which, i.e. the *standard deviation*, is proportional to the oscillation amplitude of ν up to zero-mean noises. In Figure 2.6 (c), a phase diagram in terms of the standard deviation $\sqrt{\mathrm{Var}(\nu)}$ is measured using the same method as in Figure 2.4(a). An abrupt change in $\sqrt{\mathrm{Var}(\nu)}$ is observed along the boundary between the cycling phase and the partially ordered phase.

2.4 Field-theoretic treatment

2.4.1 Coarse-graining *à la* Dean

Following the procedures of Dean [20], as has been discussed in Subsection 1.2.1, a continuum description of PAM is achieved through coarse-graining the particle-based model (2.3). The empirical distribution of particles $f(\mathbf{r},\theta,t)=\sum_{j=1}^{N}\delta[\mathbf{r}-\mathbf{r}_j(t)]\delta[\theta-\theta_j(t)]$ in the composed space of position $\mathbf{r}\in\mathbb{T}^2$ and phase $\theta\in\mathbb{R}$ becomes the central object of the continuum description.
The derivation starts from the effective particle-based dynamics

$$\begin{aligned}\dot{\mathbf{r}}_i&=\sqrt{2D}\boldsymbol{\xi}_i\\ \dot{\theta}_i&=\omega+\pi\sigma_0^2\sum_j\Big[\varepsilon\sin(\theta_j-\theta_i)-\mu_\theta(\partial_\varphi U)(\partial_{\theta_j}\varphi)\Big]\delta(\mathbf{r}_i-\mathbf{r}_j)+\sqrt{2D_\theta}\eta_i,\end{aligned}\tag{2.12}$$

where we neglect the contribution from repulsion U to the overdamped Langevin dynamics of $\{\mathbf{r}_i\}$ since its effect of homogenising the particle positions can be fully covered by the noises $\{\boldsymbol{\xi}_i\}$. In the equations of $\{\theta_i\}$, we again approximated $\{\partial_{\theta_j}U\}$ by using the product rule (2.10), with an insertion of the global packing fraction φ defined in Equation (2.9). This approximation, after applying Equation (2.1), leads to

$$\begin{aligned}\dot{\mathbf{r}}_i&=\sqrt{2D}\boldsymbol{\xi}_i\\ \dot{\theta}_i&=\omega+\sum_j\Big[\bar{\varepsilon}\sin(\theta_j-\theta_i)-c\cos\theta_j-\frac{\lambda c}{2}\sin(2\theta_j)\Big]\delta(\mathbf{r}_i-\mathbf{r}_j)+\sqrt{2D_\theta}\eta_i,\end{aligned}\tag{2.13}$$

where $\bar{\varepsilon}=\pi\sigma_0\varepsilon, c=\mu_\theta\lambda(\pi\sigma_0\sigma(0)/L)^2(\partial_\varphi U)$.
Coarse-graining Equation (2.13) via the procedures in Subsection 1.2.1 yields the exact field equation

$$\begin{aligned}\partial_t f=-\partial_\theta\Bigg[f(\mathbf{r},\theta,t)\Bigg(\omega+\sum_j\Big[\bar{\varepsilon}\sin(\theta_j-\theta)-c\cos\theta_j-\frac{\lambda c}{2}\sin(2\theta_j)\Big]\\ \delta(\mathbf{r}-\mathbf{r}_j)\Bigg)\Bigg]-\sum_i\Big[\sqrt{2D}\boldsymbol{\xi}_i\cdot\partial_{\mathbf{r}}f_i+\sqrt{2D_\theta}\eta_i\partial_\theta f_i\Big]+(D\partial_{\mathbf{rr}}^2+D_\theta\partial_{\theta\theta}^2)f.\end{aligned}\tag{2.14}$$

Equation (2.14) is a *stochastic partial differential equation* (SPDE) of a density field f on space $\mathbf{r}$ and phase θ, based on which a direct interpretation

is hardly achievable. Technically, such an SPDE is difficult for analytical treatment on its original form. In the following, we further process Equation (2.14) via mode expansion and approximations in order to obtain a closed set of simpler equations.

2.4.2 Derivation of field equations

Since $f(\mathbf{r},\theta,t)$ is periodic in θ, one may perform a Fourier-mode expansion

$$f(\mathbf{r},\theta,t)=\sum_{n=-\infty}^{\infty} f_n(\mathbf{r},t)e^{-\mathrm{i}n\theta}, \tag{2.15}$$

such that one may achieve a hierarchy of equations for each mode

$$\begin{aligned}\partial_t f_n &= (\mathrm{i}n\omega - D_\theta n^2 + D\partial_{\mathbf{rr}}^2)f_n + \frac{n\bar{\varepsilon}}{2}(-f_{n+1}f_1^* + f_{n-1}f_1)\\ &\quad - \mathrm{i}nc\Big[\mathrm{Re}(f_1)+\frac{\lambda}{2}\mathrm{Im}(f_2)\Big]f_n + \Lambda_n,\\ \Lambda_n &= \sum_i e^{\mathrm{i}n\theta_i}\Big[-\sqrt{2D}\boldsymbol{\xi}_i\cdot\partial_{\mathbf{r}}\delta(\mathbf{r}-\mathbf{r}_i) + \mathrm{i}n\sqrt{2D_\theta}\eta_i\delta(\mathbf{r}-\mathbf{r}_i)\Big].\end{aligned} \tag{2.16}$$

In the hierarchical set of equations (2.16), each mode n is coupled to its nearest-neighbouring modes $n+1$ and $n-1$, along with the modes f_1, f_2. In fact, from the definition of modes one may immediately notice that $\forall n \in \mathbb{Z}$, $f_{-n}=f_n^*$ and the first two non-negative modes f_0, f_1 are the local density and the local synchronisation order parameter respectively. The dynamics of f_1 is the central object of interest since it indicates the phases. We write down the equations of the modes around f_1

$$\begin{aligned}\partial_t f_0 &= D\partial_{\mathbf{rr}}^2 f_0,\\ \partial_t f_1 &= (\mathrm{i}\omega - D_\theta + D\partial_{\mathbf{rr}}^2)f_1 + \frac{\bar{\varepsilon}}{2}(-f_2 f_1^* + f_0 f_1) - \mathrm{i}c\Big[\mathrm{Re}(f_1)+\frac{\lambda}{2}\mathrm{Im}(f_2)\Big]f_1,\\ \partial_t f_2 &= (2\mathrm{i}\omega - 4D_\theta + D\partial_{\mathbf{rr}}^2)f_2 + \bar{\varepsilon}(-f_3 f_1^* + f_1^2) - 2\mathrm{i}c\Big[\mathrm{Re}(f_1)+\frac{\lambda}{2}\mathrm{Im}(f_2)\Big]f_2.\end{aligned} \tag{2.17}$$

These equations are not closed as f_2, f_3 are involved. What we aim at is a closed equation of f_1. To this end, one should close the equation for f_1 by truncating the hierarchy (2.16) in the noiseless limit ($\forall n \in \mathbb{Z}, \Lambda_n = 0$). Following the scaling Ansatz [35]

$$f_n \sim \chi^n, \partial_t \sim \partial_{\mathbf{rr}}^2 \sim \chi^2, \tag{2.18}$$

where $\chi \ll 1$, the equations in (2.17) are of χ^2-,χ^3- and χ^4-orders. We then truncate the hierarchy (2.16) at χ^3-order. After setting all $\mathcal{O}(\chi^4)$-terms to zero, one solves f_2 in terms of f_1

$$f_2 = \frac{\bar{\varepsilon} f_1^2}{2(2D_\theta - \mathrm{i}\omega)}. \tag{2.19}$$

Plugging Equation (2.19) back into the equation for f_1 in (2.17) yields the noiseless equations

$$\begin{aligned} \partial_t f_0 &= D\partial_{\mathbf{rr}}^2 f_0 \\ \partial_t f_1 &= \Big(\frac{\bar{\varepsilon}\rho_0}{2} - D_\theta + \mathrm{i}\omega + D\partial_{\mathbf{rr}}^2\Big) f_1 - \frac{\bar{\varepsilon}^2 f_1 |f_1|^2}{4(2D_\theta - \mathrm{i}\omega)} \\ &\quad - \mathrm{i}c f_1 \bigg[\mathrm{Re}(f_1) + \frac{\bar{\varepsilon}\lambda}{4}\mathrm{Im}\Big(\frac{f_1^2}{2D_\theta - \mathrm{i}\omega}\Big)\bigg]. \end{aligned} \tag{2.20}$$

Since f_0 is purely diffusive without the influence by f_1, in a steady state it should always be homogeneous $\forall \mathbf{r} \in \mathbb{T}^2, f_0(\mathbf{r}, t) = \rho_0$. Denoting $A = f_1$ we arrive at a single equation

$$\begin{aligned} \partial_t A &= \Big(\frac{\bar{\varepsilon}\rho_0}{2} - D_\theta + \mathrm{i}\omega + D\partial_{\mathbf{rr}}^2\Big) A - \frac{\bar{\varepsilon}^2 A |A|^2}{4(2D_\theta - \mathrm{i}\omega)} \\ &\quad - \mathrm{i}cA \bigg[\mathrm{Re}(A) + \frac{\bar{\varepsilon}\lambda}{4}\mathrm{Im}\Big(\frac{A^2}{2D_\theta - \mathrm{i}\omega}\Big)\bigg]. \end{aligned} \tag{2.21}$$

Equation (2.21) is formally close to the well-known CGLE (1.23) with a real-valued diffusion coefficient. Nevertheless, unlike CGLE, our Equation (2.21) explicitly breaks the $U(1)$ symmetry $A \to Ae^{\mathrm{i}\Phi}, \Phi \in \mathbb{R}$ due to the term proportional to c. Since c is the only parameter that contains the information of repulsion U and is proportional to $\partial_\varphi U$, one can argue that it is the repulsion U that breaks the $U(1)$ symmetry.
Besides, under the framework of CGLE, a real-valued diffusion coefficient denies the possibility of exhibiting patterns. See [11] for the comprehensive discussion. Therefore, the field-theoretic description of our wave patterns should not be found within standard CGLE-classes, but should rather be considered as stemming from the breaking of $U(1)$ symmetry by repulsion. In the following Subsection, we analyse Equation (2.21) and show the results of numerical simulations.

2.4.3 Analysis and simulations

Homogeneous solutions Analysing the homogeneous steady states requires an amplitude-angle decomposition $A = Re^{\mathrm{i}\psi}$ with $R > 0, \psi \in \mathbb{R}$. This

leads to

$$\begin{aligned}\partial_t R &= \Big(\frac{\bar{\varepsilon}\rho_0}{2} - D_\theta\Big)R - \frac{D_\theta \bar{\varepsilon}^2 R^3}{2(4D_\theta^2+\omega^2)},\\ R\partial_t\psi &= \omega R - \frac{\omega\bar{\varepsilon}^2R^3}{4(4D_\theta^2+\omega^2)} - cR\Bigg[\cos\psi + \frac{\lambda\bar{\varepsilon}R^2(2D_\theta\sin(2\psi)+\omega\cos(2\psi))}{4(4D_\theta^2+\omega^2)}\Bigg].\end{aligned} \tag{2.22}$$

The steady state requires $\partial_t R = 0$, leading to two non-negative roots: $R_h = 0$ or $R_h = \bar{\varepsilon}^{-1}\sqrt{(\bar{\varepsilon}\rho_0/D_\theta - 2)(4D_\theta^2+\omega^2)}$, corresponding to a disordered configuration and an ordered configuration respectively. The stability of the two fixed points are probed by a linear perturbation $R = R_h + \delta R$. This leads to

$$\partial_t \delta R = \Big(\frac{\bar{\varepsilon}\rho_0}{2} - D_\theta + D\partial_{\mathbf{rr}}^2\Big)\delta R - \frac{3D_\theta\bar{\varepsilon}^2R_h^2\delta R}{2(4D_\theta^2+\omega^2)} \tag{2.23}$$

In Fourier q-space it reads

$$\frac{\mathrm{d}}{\mathrm{d}t}\delta\tilde{R}_q = \sigma(q)\,\delta\tilde{R}_q, \quad \sigma(q) = \frac{\bar{\varepsilon}\rho_0}{2} - D_\theta - \frac{3D_\theta\bar{\varepsilon}^2R_h^2}{2(4D_\theta^2+\omega^2)} - Dq^2. \tag{2.24}$$

The disordered configuration $R_h = 0$ is stable iff $\frac{\bar{\varepsilon}\rho_0}{2} - D_\theta < 0$, since in this case $\sigma(q) < 0$ for all q. This agrees with the scaling argument obtained in the analysis of particle-based simulations that explains the monotonic decreasing shape of the boundary between the disordered phase and the cycling phase. See the red dotted line in Figure 2.7 (a) and the dark red line in Figure 2.4 (a). The nonzero root R_h is possible iff $\frac{\bar{\varepsilon}\rho_0}{2} - D_\theta > 0$ since a positive argument is needed under a square root. In this case we plug in the nonzero R_h into $\sigma(q)$ to get

$$\sigma(q) = -2\left(\frac{\bar{\varepsilon}\rho_0}{2} - D_\theta\right) - Dq^2. \tag{2.25}$$

Again, $\sigma(q)$ is negative definite for all q, indicating that the nonzero homegeneous R_h is linearly stable against any linear perturbations.
In an ordered phase $R_h > 0$, the equation of homogeneous collective phase ψ becomes

$$\dot{\psi}_h = \Omega - V'(\psi_h), \tag{2.26}$$

with

$$\begin{aligned}\Omega &= \omega\Big(\frac{3}{2} - \frac{\bar{\varepsilon}\rho_0}{4D_\theta}\Big)\\ V &= c\Bigg[R_h\sin\psi_h + \frac{\lambda}{2\bar{\varepsilon}}\Big(1 - \frac{\bar{\varepsilon}\rho_0}{2D_\theta}\Big)(2D_\theta\cos(2\psi_h) - \omega\sin(2\psi_h))\Bigg].\end{aligned} \tag{2.27}$$

When the tilted potential $V(\psi_h) - \Omega\psi_h$ is strictly monotonic in ψ_h, the ordered phase is cycling. In the cycling phase, the global drive Ω determines whether the cycling is clockwise ($\Omega > 0$) or counter-clockwise ($\Omega < 0$). The counter-clockwise cycling requires $\bar{\varepsilon}\rho > 6D_\theta$ which has no equivalent in the particle-based dynamics. This regime is too far away from the disorder-order transition, around which the coarse-grained description of the particle-based dynamics is effective. Indeed, Equation (2.19) can be regarded as an expansion to the lowest order in f_1.
When a local minimum of $V(\psi_h) - \Omega\psi_h$ exists, one obtains an arrested phase. To leading order in λ, one finds

$$x^2(x-3)^2 - B^2(x-1) < 0, \tag{2.28}$$

with

$$x = \frac{\bar{\varepsilon}\rho_0}{2D_\theta}, \quad B = \frac{c\rho_0}{\omega}\sqrt{2\left[4 + \left(\frac{\omega}{D_\theta}\right)^2\right]}. \tag{2.29}$$

To leading order in $B \sim \mathcal{O}(\lambda)$, the solution to (2.28) reads

$$3 - \frac{\sqrt{2}}{3}B < x < 3 + \frac{\sqrt{2}}{3}B. \tag{2.30}$$

This criterion is depicted with the black dashed line in Figure 2.7(a). In the limit of small ρ_0, the interval (2.30) converges to a single point $x = 3$, which agrees with the condition $\bar{\varepsilon}\rho_0 = 6D_\theta$ leading to $\Omega = 0$.
The stability of homogeneous ψ_h is demonstrated by a linear perturbation $\psi = \psi_h + \delta\psi$. In Fourier q-space, knowing that R_h is anyway linearly stable, this results in

$$\frac{\mathrm{d}}{\mathrm{d}t}\kappa\delta\tilde{\psi}_q = \iota\delta\tilde{R}_q + \upsilon(q)\delta\tilde{\psi}_q, \tag{2.31}$$

where $\upsilon(q) = -V''(\psi_h) - Dq^2$. According to Equations (2.23) and (2.31), the linear stability around a homogeneous solution depends only on $\sigma(q), \upsilon(q)$. At a local minimum ψ_h, $V''(\psi_h) > 0$. Therefore $\forall q \in \mathbb{R}, \upsilon(q) < 0$. Hence the arrested phase at the local minimum ψ_h of the tilted hydrodynamic potential $V - \Omega\psi$ is always linearly stable. In fact, the existence of a stable arrested phase is caused by the term proportional to c in Equation (2.21). This term explicitly breaks the $U(1)$ symmetry. Since $c \propto \partial_\varphi U$ is the only source of repulsion in Equation (2.21), it is the repulsion between particles that lifts the $U(1)$ symmetry. This physical interpretation is immediately clear in particle-based dynamics. Indeed, a globally synchronised growth of all particles leads to a higher repulsive energy cost than a globally synchronised shrinkage.

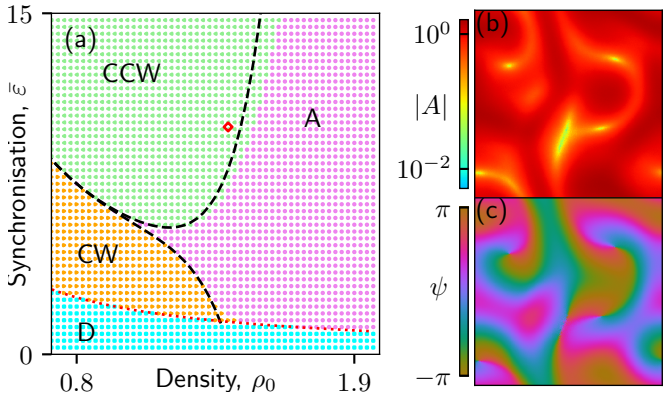

Figure 2.7: (a) Phase diagram of the noiseless continuum dynamics (2.21) obtained with A being initialised in homogeneous ordered state. Four homogeneous phases are observed in steady states: disordered phase (D), clockwise cycling phase (CW), counter-clockwise cycling phase (CCW) and arrested phase (A). The boundary between the cycling phase and the arrested phase (black dashed) is recovered analytically by (2.30). The boundary between disordered phase and ordered phases (red dotted) is described by $\bar{\varepsilon}\rho_0 = 2D_\theta$ obtained from linear stability analysis. (b,c) Dynamical patterns with motile defects realised by adding a noise to (2.21) at a point in a cycling phase (red diamond) obtained with A being randomly initialised. Both the amplitude (b) and the phase (c) of the local synchronisation order parameter A show such dynamical patterns that are reminiscent of defect turbulence in Figure 2.3(d). All simulations are performed with the other parameter values being fixed at $c = \lambda\rho_0^{12}/(1+\lambda)^2, D = 4000, D_\theta = 1, \omega = 10, \lambda = 0.05, \mathrm{d}t = 0.01$. Each trajectory relaxes during $t_{\mathrm{ini}} = 4 \times 10^4\,\mathrm{d}t$.

Noise fields All the analytical analysis in terms of linear stabilities of homogeneous solutions successfully agrees perfectly with the observations in numerical simulations of Equation (2.21) with homogeneous initial configurations. The phase diagram is then measured in terms of the stationary values of R_h and the existence of stationary ψ_h based on Equation (2.26). See Figure 2.7(a). However, no inhomogenities are involved here, allowing no room for wave patterns. Further numerical simulations show that the lack of inhomogeneities holds true even with truncations of the hierarchy (2.16) at higher orders in χ. To open a window for wave patterns between the cycling phase and the arrested phase, introducing the noise fields is necessary.
Here, only the noise Λ_1 on the mode f_1 is considered. To further constrain the role of noise, the contribution from D, i.e. the noise in translation, is neglected. Hence according to Equation (2.16) one can write

$$\Lambda_1 = \sqrt{2D_\theta}(u_1 + \mathrm{i}v_1), \tag{2.32}$$

with $[u_1, v_1] = \sum_i [\sin\theta_i, -\cos\theta_i]\eta_i\delta(\mathbf{r} - \mathbf{r}_i)$. The noise components $\{u_1, v_1\}$ are Gaussian and have zero means, with spatio-temporal correlations

$$\begin{aligned}
&\big\langle [u_1, v_1]^{\mathrm{T}}(\mathbf{r}, t)[u_1, v_1](\mathbf{r}', t')\big\rangle \\
&= \sum_{jk} \begin{bmatrix} \sin(\theta_j(t))\sin(\theta_k(t')) & -\sin(\theta_j(t))\cos(\theta_k(t')) \\ -\cos(\theta_j(t))\sin(\theta_k(t')) & \cos(\theta_j(t))\cos(\theta_k(t')) \end{bmatrix} \\
&\delta(\mathbf{r} - \mathbf{r}_j(t))\delta(\mathbf{r}' - \mathbf{r}_k(t'))\langle \eta_j(t)\eta_k(t')\rangle \\
&= \frac{1}{2}\delta(\mathbf{r} - \mathbf{r}')\delta(t - t') \sum_j \begin{bmatrix} 1 - \cos(2\theta_j(t)) & -\sin(2\theta_j(t)) \\ -\sin(2\theta_j(t)) & 1 + \cos(2\theta_j(t)) \end{bmatrix} \delta(\mathbf{r} - \mathbf{r}_j(t)) \\
&= \frac{1}{2}\delta(\mathbf{r} - \mathbf{r}')\delta(t - t') \begin{bmatrix} f_0(\mathbf{r}, t) - \mathrm{Re}\{f_2(\mathbf{r}, t)\} & -\mathrm{Im}\{f_2(\mathbf{r}, t)\}) \\ -\mathrm{Im}\{f_2(\mathbf{r}, t)\} & f_0(\mathbf{r}, t) + \mathrm{Re}\{f_2(\mathbf{r}, t)\}) \end{bmatrix}.
\end{aligned} \tag{2.33}$$

For simplicity, the f_2-contribution to the noise is neglected. In this way there is no cross correlation between u_1 and v_1. Noticing that in the steady state $f_0 = \rho_0$ everywhere, one may arrive at a diagonal correlation matrix

$$\big\langle u_1(\mathbf{r}, t)u_1(\mathbf{r}', t')\big\rangle = \big\langle v_1(\mathbf{r}, t)v_1(\mathbf{r}', t')\big\rangle = \frac{\rho_0}{2}\delta(\mathbf{r} - \mathbf{r}')\delta(t - t'). \tag{2.34}$$

Such a correlation, according to Equation (2.32), should be realised by a noise term $\sqrt{\rho_0 D_\theta}\Lambda(\mathbf{r}, t)$ added to the RHS of the noiseless equation (2.21) which leads to

$$\begin{aligned}
\partial_t A = &\Big(\frac{\bar{\varepsilon}\rho_0}{2} - D_\theta + \mathrm{i}\omega + D\partial^2_{\mathbf{rr}}\Big)A - \frac{\bar{\varepsilon}^2 A|A|^2}{4(2D_\theta - \mathrm{i}\omega)} \\
&- \mathrm{i}cA\Big[\mathrm{Re}(A) + \frac{\bar{\varepsilon}\lambda}{4}\mathrm{Im}\Big(\frac{A^2}{2D_\theta - \mathrm{i}\omega}\Big)\Big] + \sqrt{\rho_0 D_\theta}\Lambda,
\end{aligned} \tag{2.35}$$

with

$$\Lambda = u + \mathrm{i}v, \langle u(\mathbf{r},t)u(\mathbf{r}',t')\rangle = \langle v(\mathbf{r},t)v(\mathbf{r}',t')\rangle = \frac{1}{2}\delta(\mathbf{r}-\mathbf{r}')\delta(t-t'). \quad (2.36)$$

In the presence of noise at continuum level, between the cycling phase and the arrested phase in Figure 2.7(a), a window accommodating steady states with dynamical patterns emerges, with examples shown in Figure 2.7(b)(c). With the noisy continuum description (2.35), only these dynamical patterns associated with the birth and merging of motile defects can be realised, which are reminiscent of the defect turbulence observed in particle-based simulations shwon in Figure 2.3(d). The other wave patterns without motile defects are not observed at continuum level. Remembering that the dynamical patterns at continuum level are realised only by adding an approximated additive noise to the noiseless dynamics of the model f_1 with a constant density in steady states, one may expect the missing dynamical patterns to be stabilised by recovering the fluctuations in density field in steady states.

2.5 Discussions and outlooks

In this work, PAM is proposed as a novel class of active matter that leads to patterns at continuum level that are similar to RDS. This is striking as PAM is based on a minimised setup that does not even include reactions, whilst spatial diffusion is suppressed at high densities where wave patterns exist. Although in [16], the individual pulsations of particles were seen as mimicking chemical reactions, with particle phases being reaction coordinates, our work extends its description power to include non-reactive processes such as cell deformation. With this non-reactive setup, contractile wave propagation in biological tissues as dense assemblies of cells is mimiced as a compromise between particle size synchronisation and inter-particle repulsion.

At the continuum level, the two-body interactions introduce nonlinearities in Equations (2.21) and (2.36). Specifically, the nonlinear $A|A|^2$-term introduced by a nonzero $\bar{\varepsilon}$, preserving the $U(1)$ symmetry, stabilises the ordered cycling phase. On the other hand, the nonlinear term introduced by c breaks the $U(1)$ symmetry and fixes the ordered phase to a preferred collective phase ψ_h relative to a tilted potential. All the essential elements play their respective roles correctly, even in the continuum model, although an intermediate phase with dynamical patterns between the cycling phase and the arrested phase was absent in the noiseless limit. Further refinements of the continuum description, such as incorporating fluctuating density, local coupling between density and order, etc., can be pursued to more accurately capture

the phenomenologies observed in particle-based simulations. Additionally, the detailed role of noise in the formation of wave patterns, which is currently absent in this study, warrants further investigation. All these efforts can contribute to the development of a class of field theories for pulsation waves.

In general, the paradigm of deforming spherical particles is a powerful tool for simulating complex many-body structures with changing interaction ranges between nearest neighbours, such as biological tissues. Compared to models of spherical particles with fixed sizes, the deforming particles introduce polydispersity to a particle assembly that enlarges the range of potential phenomenologies in a spherical particle assembly.

Using such powerful yet simple models, one can expect to describe further real systems beyond epithelial tissues. In our model, the existence of different wave patterns is shown to be controllable by system density and synchronisation strength. This warrants further investigation, as in cardiac tissues, spiral waves and turbulence are also propagated through cell deformation without significant cell migration, resulting in fibrillation, a fatal pattern of cardiac dynamics that disrupts the directional pumping of blood [93]. Clinically, defibrillators are used in first-aid to apply high voltages to the living heart to eliminate such disruptive wave patterns, although such drastic treatment can cause damage. Current ongoing studies are exploring gentle treatments that can mitigate fibrillation [100, 101] without significant side effects. In this context, it would be interesting to explore the crossover between different wave patterns in relation to the work presented in this Chapter.

To this end, one may consider introducing further elements to engineer the wave patterns. For instance, to mimic fibrillation, one could consider incorporating inhomogeneities in particle size intervals or adjusting the active drive ω. Nonetheless, the current piece of work takes the initial step in understanding the mechanism of the emergence of different wave patterns. Within this framework, an immediate extension to our work would be the examination of defect statistics. For example, conducting systematic investigations into the number of defects and the typical distances between defects as functions of system size L, density ρ_0 and synchronisation strength ε would contribute to a deeper understanding of the emergence and disappearance of defects. Also, the interplay between the defects defined in this work and *structural defects* defined as irregular number of neighbouring particles in a crystallised region would deserve further scrutiny.

Chapter 3

Species Interconversion through Particle Deformations

In this chapter, we investigate the emergence of transient *liquid-liquid phase separation* (LLPS) resulting from particle conversions. We propose a model that comprises a dense assembly of repulsive deforming particles. The sizes of these particles are determined by their internal states subject to a one-body potential landscape and non-equilibrium synchronisation interactions. The one-body potential features three local minima, classifying the particles into three distinct species based on their internal states. One of the three species is metastable. We report in this Chapter the conditions for transient LLPS between two species. Besides, via the systematic coarse-graining procedures and various approximations, we obtain a Model-A-type continuum description and subsequently investigate the continuum model. We find that the numerically measured phase diagram based on the continuum model qualitatively captures the phenomenologies of the particle-based model. In addition, we clarified the different natures of transitions via a free-energetic approach.
This Chapter is organised as follows: in Section 3.1, we introduce the background of this work. In Section 3.2, we describe our particle-based model. In Section 3.3, we present the relaxation procedures observed in particle-based simulations with a symmetric one-body potential. In Section 3.4, we measure the phase diagrams as functions of different asymmetric one-body potentials. In Section 3.5, we derive the field theories and present the results of field-theoretic studies. In Section 3.6, we summarise the work in this Chapter.

3.1 Introduction

Liquid-liquid phase separations (LLPS) occur in liquid mixtures in which the affinity between different components is weak compared to that within the same component [102], such as water-oil mixtures [103] in equilibrium. In a reactor, where chemical reactions take place at a large scale, however, the chemical composition of the liquid mixture is altered constantly, which is described in terms of RDS [104].

As has been mentioned in Chapter 2, RDS are known for exhibiting a richness of patterns and have been intensively studied. Besides dynamical patterns such as B-Z chemical oscillations, many stationary patterns are also found to exist in the framework of RDS. These stationary patterns are sometimes considered as phase separations. The phase-separated configuration may have multiple regions rich in one species or the other. In this case, such phase separations are known as microphase separations. Examples include the stripe patterns on animal skins [105], block copolymers [106], etc. When the phase-separated configuration features only two regions rich in different species, the phase separation is seen as macroscopic. Examples include the phase separation between water and oil, the phase separation between species in auto-catalysed electrochemical processes [107], etc. Recently, such stationary patterns have been systematically discussed in terms of instabilities in non-ideal RDS [108]. In those discussions, phase separations are classified into two types of instabilities. Either it is the intermolecular interactions that leads to a macrophase separation, or the multimolecular reactions out of equilibrium cause microphase separation [108].

Binary mixtures are widely found across different domains, from natural science, such as metallic [109–111] and glassy [112, 113] alloys, copolymers [114, 115] and curved biomembranes as lipid mixtures [116–120], and social science, such as human populations [121]. This minimal setup encompasses a broad range of features of mixtures, including phase separations. Yet, phase separations in mixtures include much more than the equilibrium water-oil separation. In fact, using the agent-based Schelling's segregation model, one may obtain a phase separation between communities of agents holding different stances, which mimics the political polarisation [122] in real world. In non-reactive mixtures, the phase separation upon temperature quench has typically been ascribed to *spinodal decomposition* [123], as a result of the miscibility gap between the two components and thus the instability of the monophase configuration. Later studies on reactive binary mixtures added chemical conversions into the framework of spinodal decomposition [124–128]. In living biological cells, membraneless organelles self-organise via phase separation to constrain biochemical processes spatially [18, 129, 130].

The classical Ising model, although initially motivated for studying ferromagnetism in solid crystals [131], is a paradigmatic model of binary mixtures exhibiting phase separations. Within the framework of finite-sized systems, in Kawasaki dymamics, a conserved global magnetisation maintains a phase separation as the steady state [132], whereas in Glauber dynamics, starting from a disordered configuration, transient phase separations occur *en route* towards fully ordered steady states [133]. These phase separations are induced purely by spin flips on immobile regular lattice points.

An example of off-lattice dynamics akin to the Ising model is the study on the *chiral symmetry breaking* (CSB) in a binary mixture of enantiomers [134]. In such a system, the interconversion between enantiomers are mimicked with mechanical deformations of simplified molecules composed of rods and spheres. A degenerate double-well potential landscape is used to accommodate enantiomers with different chiralities and the transition state conformations between them. Starting from a disordered configuration, the relaxation of the binary mixture experiences a transient phase separation between domains of different chiralities, which finally disappears to realise a complete CSB.

Beyond a single elementary reaction, many chemical reactions, especially biochemical processes involving a plethora of species, contains extensive elementary reactions organised into *chemical reaction networks* (CRNs) [135–137]. CRNs capture essential dynamical properties, such as steady states (number and stabilities) [138, 139], initial reactants' persistence [140], periodicity [141], to name a few, using simple descriptions [142, 143]. However, a complete CRN-description of a complex reaction system is hardly achievable, due to unknown elementary reactions involved and difficulties in measuring all rate constants experimentally. Furthermore, not all details in a CRN are relevant for the features of interest. Intensive effort has thus been paid towards reducing CRNs for a renormalised simpler descriptions with less building blocks whilst still capturing essential properties [144–151].

Whilst for reactive dynamics, the non-conservation of total particle number is common in open systems, it is difficult to implement for diffusive dynamics. Typically, one has to model the "void states" mimicking the particle number reduction during a reaction collision. Such void states exist in an extensive class of lattice-based models capturing the non-equilibrium physics of systems, which can be regularised into field theories [152, 153]. In particular, the "A+B$\to \varnothing$"-type models allows particle annihilation upon collision, which effectively introduces an absorbing particle reservoir. In such models at criticality, particle numbers decay with time, following a universal power law in the late stage in particular. Some of such models allow both particle creation and annihilation, motivated by surface catalysis [154] where a solid

catalyst is placed in a reaction system to reversibly absorb and desorb reactants and products.
In our work, we consider using point particles with vanishing size to effectively represent the void states in diffusive systems. Particles can in general change their sizes, and are subject to a one-body potential which constrains size fluctuations. This one-body potential contains multiple minima associated to distinct "species", thus playing the role of an effective reaction landscape. The void state is placed in one of our one-body potential wells as a metastable state. We find multi-step relaxation processes leading to homogeneous steady states containing only one species. We add asymmetries to the one-body potential and find the steady states depend on these asymmetries. Like in the "A+B$\rightarrow \varnothing$"-type models, we derive a field-theoretic description of our diffusive model. Our field-theoretic description involves a mapping towards an effective equilibrium, and turns out to be a Model-A-type field theory. We perform further analysis using tools from equilibrium field theories. In the framework of field theories, we predict the steady states associated to given asymmetries in the one-body potential.

3.2 Model description

In this work, we consider a dense assembly composed of N deforming soft disks at temperature T in a bidimensional square box of edge L, with periodic boundary conditions being applied in both dimensions. These deforming soft disks repell each other and homogenise their sizes via synchronisation. The dynamics of this many-particle assembly is described by the following particle-based equations of motion

$$\begin{aligned}
\dot{\mathbf{r}}_i &= -\mu \sum_{j=1}^{N} \partial_{\mathbf{r}_i} U(a_{ij}) + \sqrt{2\mu T}\, \boldsymbol{\xi}_i, \\
\dot{\sigma}_i &= -\sum_{j=1}^{N} \Big[\mathcal{T}(a_{ij}, \sigma_j - \sigma_i) + \mu_\sigma \partial_{\sigma_i} U(a_{ij}) \Big] - \mu_\sigma V'(\sigma_i) + \sqrt{2\mu_\sigma T}\eta_i,
\end{aligned} \tag{3.1}$$

where μ, μ_σ are spatial mobility and σ-mobility respectively, $V'(\sigma_i) = \mathrm{d}V \,/\, \mathrm{d}\sigma \,|_{\sigma_i}$, U is the WCA repulsive potential with the form in Equation (2.5) taking the rescaled distance a_{ij} as the argument, $\mathcal{T}$ is the synchronisation interaction and V is the one-body potential in σ-space. The translation of particles still follows overdamped Langevin dynamics similar to PAM. Both $\{\mathbf{r}_i\}$ and $\{\sigma_i\}$ carry zero-mean, unit-variance Gaussian white noises $\{\boldsymbol{\xi}_i\}$ and $\{\eta_i\}$ respectively. To avoid self-interactions, $\mathcal{T}$ and U are both zero whenever $i = j$.

In a dense assembly, the two-body repulsion U and synchronisation $\mathcal{T}$ have major effects on particle sizes due to strong overlap between particles. Similar to PAM, the two-body interactions have short interaction ranges restricted by a Heaviside kernal $\Theta(1-a_{ij})$, where the rescaled dimensionless distance between particles i and j is measured as

$$a_{ij}=\frac{|\mathbf{r}_i-\mathbf{r}_j|}{|\sigma_i|+|\sigma_j|}, \tag{3.2}$$

i.e. the interparticle distances are rescaled with the sum of the sizes of the two particles. Unlike PAM, here the synchronisation $\mathcal{T}$ bears the form

$$\mathcal{T}(a_{ij},\sigma_j-\sigma_i)=\varepsilon(\sigma_j-\sigma_i)\Theta(1-a_{ij}), \tag{3.3}$$

i.e. instead of synchronising particle sizes, $\mathcal{T}$ synchronises the reaction coordinates of two overlapping particles.
Again, similar to PAM (see Section 2.2), each particle is described by its position $\mathbf{r}$ and an internal state σ. The internal state σ, unlike that in PAM, determines the particle size with its absolute value $|\sigma|$. Thus in principle, a particle in our model can be as small as a point particle with vanishing size, or infinitely large. Compared to Equation (2.3), there is no active drive in the dynamics of the internal state in Equation (3.1), whilst a one-body potential V exists to set a soft bound for particle sizes from above. The one-body potential in fact mimics a chemical reaction landscape with the internal state σ_i being a reaction coordinate of particle i. We adopt here a triple-well potential V with point particles $\sigma=0$ being metastable. The metastability of the state $\sigma=0$ is supposed to make point particles mimic a particle reservoir. We begin with a symmetric potential such that two degenerate local minima lie in $\pm\sigma_0$, with $\sigma_0>0$ being the stable particle size. See Figure 3.1 for a schematic example. A polynomial realisation of such a potential entails a σ^6-model with the shape

$$V(\sigma)=v_0(\sigma^6-a\sigma^4+b\sigma^2), \tag{3.4}$$

with $v_0>0$ measuring the intensity of V. The parameters a,b are determined by the stable particle size σ_0 and the unstable particle size $\sigma_{\neq}$ as the local maximum between 0 and σ_0. In such a scheme, one may classify the particles into 3 species based on their σ-values: A-particles ($\sigma>\sigma_{\neq}$), B-particles ($\sigma<-\sigma_{\neq}$) and $\varnothing$-particles ($-\sigma_{\neq}<\sigma<\sigma_{\neq}$).
Knowing that $V'(\pm\sigma_0)=V'(\pm\sigma_{\neq})=0$, one has

$$\begin{aligned}6\sigma_0^5-4a\sigma_0^3+2b\sigma_0&=0\\ 6\sigma_{\neq}^5-4a\sigma_{\neq}^3+2b\sigma_{\neq}&=0.\end{aligned} \tag{3.5}$$

Solving Equation (3.5) leads to

$$a = \frac{3}{2}(\sigma_0^2 + \sigma_{\neq}^2), b = 3\sigma_0^2\sigma_{\neq}^2. \tag{3.6}$$

Moreover, to ensure that $\pm\sigma_0$ are local minima and $\pm\sigma_{\neq}$ are local maxima, one should have $V''(\pm\sigma_0) > 0, V''(\pm\sigma_{\neq}) < 0$. This leads to

$$\begin{aligned} 30\sigma_0^4 - 18(\sigma_0^2 + \sigma_{\neq}^2)\sigma_0^2 + 6\sigma_0^2\sigma_{\neq}^2 > 0 \\ 30\sigma_{\neq}^4 - 18(\sigma_0^2 + \sigma_{\neq}^2)\sigma_{\neq}^2 + 6\sigma_0^2\sigma_{\neq}^2 < 0, \end{aligned} \tag{3.7}$$

which is automatically satisfied by $0 < \sigma_{\neq} < \sigma_0$. Importantly, to ensure that $\sigma = 0$ is metastable, one should ensure $V(\pm\sigma_{\neq}) > V(0) > V(\pm\sigma_0)$. This leads to

$$\sigma_{\neq}^6 - \frac{3}{2}(\sigma_0^2 + \sigma_{\neq}^2)\sigma_{\neq}^4 + 3\sigma_0^2\sigma_{\neq}^4 > 0 > \sigma_0^6 - \frac{3}{2}(\sigma_0^2 + \sigma_{\neq}^2)\sigma_0^4 + 3\sigma_0^4\sigma_{\neq}^2. \tag{3.8}$$

Solving the Inequality (3.8) gives

$$3\sigma_{\neq}^2 < \sigma_0^2. \tag{3.9}$$

Inequality (3.9) sets a tighter upper bound for $\sigma_{\neq}$ which is $\sigma_{\neq} < \sigma_0/\sqrt{3}$. This condition may be further checked by the metastability coefficient defined as

$$\begin{aligned} \alpha &= \frac{V(\sigma_{\neq}) - V(0)}{V(\sigma_{\neq}) - V(\sigma_0)} \\ &= \frac{1}{1 + \frac{1-3\gamma}{3\gamma^2 - \gamma^3}}, \end{aligned} \tag{3.10}$$

with $\gamma = \sigma_{\neq}^2/\sigma_0^2$. The range (3.9) clearly ensures $\alpha < 1$.

3.3 Relaxation towards steady states

3.3.1 The role of the particle reservoir: insights from equilibrium ($\varepsilon = 0$)

The synchronisation $\mathcal{T}$ between neighbouring particles is the only non-conservative interaction in our model, since the neighbours a particle synchronise with change in time. Turning off the synchronisation by setting $\varepsilon = 0$ makes the steady states of the model (3.1) in equilibrium. The resulting equilibrium configurations are disordered mixtures of particles with different σ-values. In particular, in the absence of repulsion, i.e. $U = 0$, the distribution of

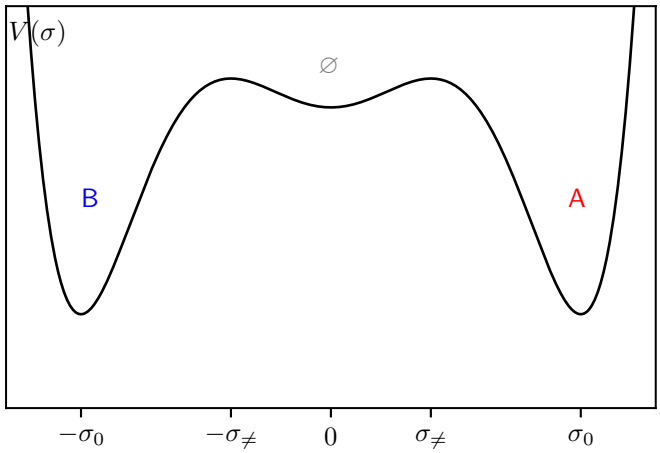

Figure 3.1: Symmetric triple-well one-body potential $V(\sigma)$, with $\sigma = 0$ being metastable and $|\sigma| = \sigma_0$ being stable. The local maxima $\pm\sigma_{\neq}$ divide the σ-values into 3 regions corresponding 3 species: A-particles (red, $\sigma > \sigma_{\neq}$), B-particles (blue, $\sigma < -\sigma_{\neq}$) and ∅-particles (gray, $|\sigma| < \sigma_{\neq}$)

σ-values $\mathcal{P}[\sigma]$ exactly follows the Boltzmann distribution with respect to the one-body potential V

$$\mathcal{P}[\sigma] \propto e^{-\beta V(\sigma)}, \tag{3.11}$$

as is reflected in Figure 3.2, since in this special case the model (3.1) has been reduced to N decoupled one-body dynamics. When $U > 0$, in a dense assembly the ∅-particles are overpopulated. This overpopulation increases with density ρ, as is shown in Figure 3.2, since higher densities lead to more repulsive energy costs, driving more particles to the metastable state. It is then tempting to regard the metastable state as an effective particle reservoir in contact with A- and B-particles. Indeed, in a dense assembly the repulsion U also contributes to changes in σ-values of particles, since more particles' being converted to ∅ reduces the repulsive energy cost.

3.3.2 Relaxation towards non-equilibrium steady states in multiple steps ($\varepsilon > 0$)

Turning on the synchronisation makes the model (3.1) out of equilibrium. With significant synchronisation between neighbouring particles, a disordered configuration can no longer be maintained since large difference in σ-values between neighbouring particles is not favoured. As a result, the steady states have to be homogeneous, containing only one single species. Whether a steady state is composed of A-, B- or ∅-particles depends on the

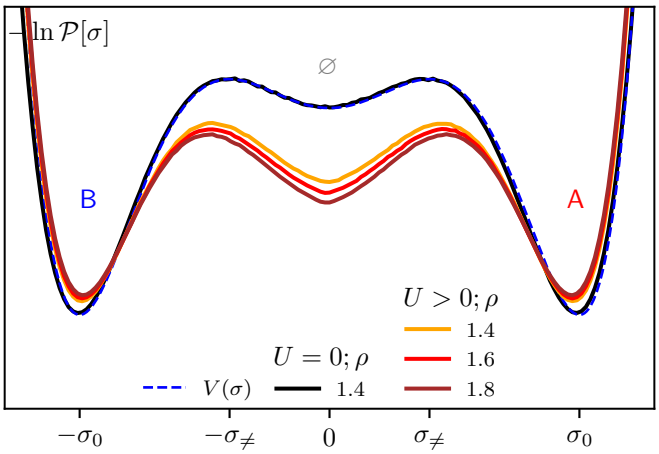

Figure 3.2: Negative log statistical distributions $-\ln \mathcal{P}[\sigma]$ (solid lines) of σ-values in fully-relaxed configurations at $\varepsilon = 0$. At $U = 0$, an exact match between $-\ln \mathcal{P}[\sigma]$ (black) and $V(\sigma)$ (blue dashed line) is reached up to an inverse temperature prefactor β and a global shift. At $U > 0$, $-\ln \mathcal{P}[\sigma]$ deviates from $V(\sigma)$ by overpopulating $\varnothing$. Increasing the density (yellow, red, brown) leads to larger populations of $\varnothing$ amongst a fixed total number N of particles. All measurements are performed in a square box of edge size $L = 100\sigma_0$ with $\sigma_0 = 1, \sigma_{\neq} = 0.4\sigma_0, v_0 = 60, T = 5, \mu = 1, \mu_\sigma = 0.1$. For $U > 0$, $u_0 = 0.0001$.

relative stabilities of those species and the relaxation process.
Under a symmetric one-body potential $V(\sigma)$, the probabilities of relaxing towards the steady state full of A-particles and that full of B-particles should be degenerate. However, a strong metastability leads to a steady state full of $\varnothing$-particles due to strong synchronisation. Starting from disordered initial configurations composed of equal number of A- and B-particles, the relaxation following Equation (3.1) leads to a steady state full of A- or B-particles at low α-values, typically $\alpha < 0.34$. Above that value of α, there starts to be a significant probability that the steady state may be full of $\varnothing$-particles. In particular, at large α-values, especially those close to unity, the steady state full of $\varnothing$-particles is more probable to exist. In fact, strengthening the metastability makes $\varnothing$-particles the third stable species, which is difficult to escape from under strong synchronisation. In the following discussions, we will be focusing on small α-values that will not lead to a steady state full of $\varnothing$-particles. See Figure 3.3.
At small α-values, the relaxation starting from a disordered mixture has three stages: (I) Shrinkage: particles of different species overlapping with each other are both quickly converted into $\varnothing$-particles, leading to a configuration with most particles being $\varnothing$ and an acute drop in the global packing fraction-Figure 3.4 (a,b). (II) Domain growth: the remaining tiny clusters of A- and B-particles surviving the shrinkage grow into large homogeneous domains by converting their neighbouring $\varnothing$-particles into the species in the clusters. This leads to a growth in the global packing fraction and finally a phase-separated configuration with $\varnothing$-particles only surviving between the domains of different species-Figure 3.4 (b,c,d). (III) Coarsening: one of the two species forming domains in phase separation is converted to the other, finally leading to a homogeneous steady state containing only one single species, either A- or B-particles. The timescale of relaxation and the steady state depends on the shape and topology of the transient phase separation. The species in a bubble will not survive during the coarsening and is quickly converted to the species outside-Figure 3.4 (d,f), while bands are long-lived and give no predictions on the species in the steady state-Figure 3.4 (c,e,f). During coarsening, the fraction of $\varnothing$-particles gradually decrease due to shrinking domain boundaries.
Since only the synchronisation $\mathcal{T}$ is non-conservative, its non-conservative work leads to irreversibility of the relaxation. The non-zero non-conservative work keeps the system out of equilibrium. We therefore use the non-conservative work rates $\{\langle\dot{\Sigma}_i\rangle\}$ as measures of irreversibilities [155, 156] at single-particle

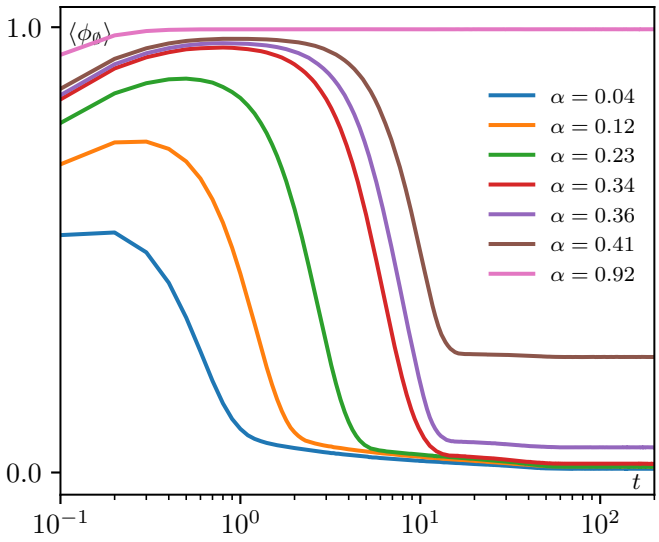

Figure 3.3: Average fractions of $\varnothing$-particles as functions of time under different metastabilities measured as over 100 trajectories for each α-value. Small α-values ensure that the steady state are not full of $\varnothing$-particles. Starting from $\alpha = 0.36$, there can be trajectories leading to the steady state full of $\varnothing$-particles. Our scope of binary mixtures is therefore restricted to $\alpha \leq 0.34$. All measurements are performed in a square box of edge size $L = 100\sigma_0$ initialised with equal amount of particles with $\sigma = \pm 1$ uniformly distributed in the square box in the absence of particles of other σ-values, with $\sigma_0 = 1, \sigma_{\neq} = 0.4\sigma_0, \rho = 1.4, v_0 = 60, T = 5, \mu = 1, \mu_\sigma = 0.1$ and $u_0 = 0.0001$.

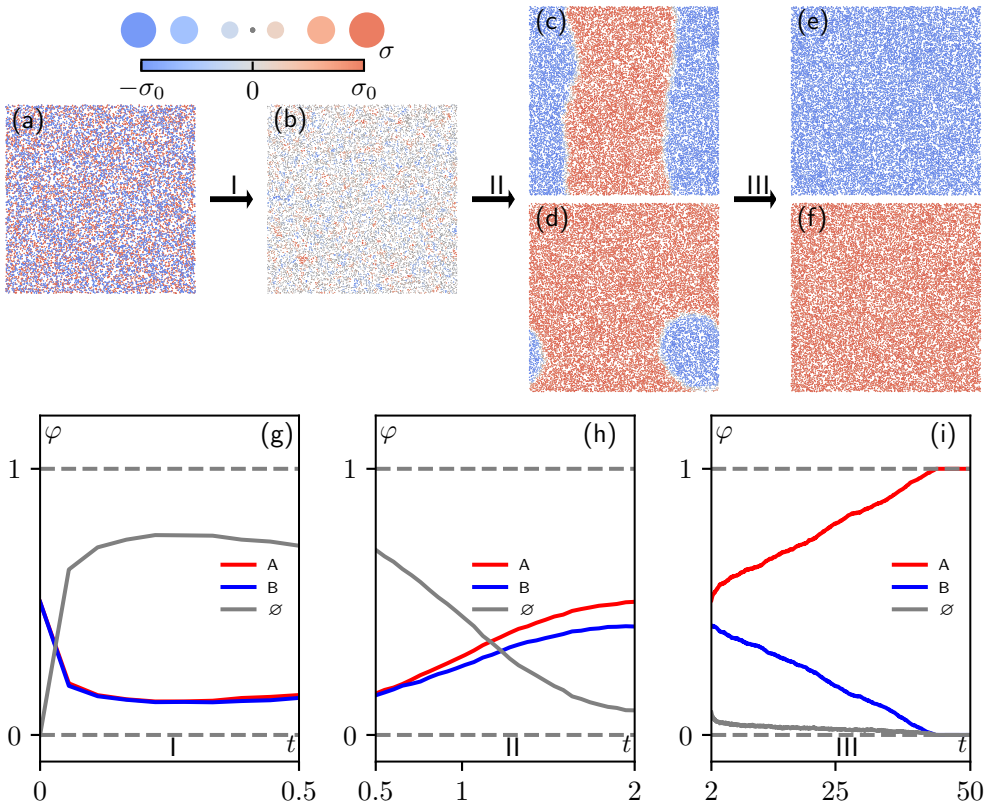

Figure 3.4: 3 stages of the relaxation following (3.1) starting from a disordered initial configuration (a): (I) Shrinkage: particles with opposite σ signs overlapping with each other are both quickly converted into $\varnothing$-particles due to synchronisation, resulting in a configuration (b) with most particles belonging to $\varnothing$ and a sharp drop in number fractions of A and B(g); (II) Domain growth: The point particles are converted back to A- and B-particles if they are immediately neighbouring to the clusters of surviving A- and B-particles, finally leading to a phase-separated configuration (c) or (d) with point particles only living on domain boundaries. The number fraction of $\varnothing$ decreases to reach a level close to 0; (III) Coarsening: The phase-separated configuration relaxes to a homogeneous steady state (e) or (f). Phase separation with a band shape (c) is long-lived and may end up with either (e) or (f) after a long relaxation, while the phase separation with B-particles in a bubble immediately leads to the steady state (f) full of A-particles. All simulations are performed in a square box of edge size $L = 100\sigma_0$ initialised with equal amount of particles with $\sigma = \pm 1$ uniformly distributed in the square box in the absence of particles of other σ-values, with $\sigma_0 = 1, \sigma_{\neq} = 0.4\sigma_0, \rho = 1.4, v_0 = 60, T = 5, \mu = 1, \mu_\sigma = 0.1$ and $u_0 = 0.0001$.

level

$$\begin{aligned}
\langle \dot{\Sigma}_i \rangle &= \langle F_{\mathrm{nc},i} \circ \dot{\sigma}_i \rangle = \langle \mu_\sigma F_{\mathrm{nc},i}(F_{\mathrm{nc},i} + F_{\mathrm{c},i}) + D_\sigma \partial_{\sigma_i} F_{\mathrm{nc},i} \rangle \ , \\
F_{\mathrm{nc},i} &= \sum_{j \neq i} \mathcal{T}(a_{ij}, \sigma_j - \sigma_i) \ , \\
F_{\mathrm{c},i} &= -\sum_{j \neq i} \partial_{\sigma_i} U(a_{ij}) - V'(\sigma_i) \ ,
\end{aligned} \tag{3.12}$$

where $\circ$ is the Stratonovich product, $D_\sigma = \mu_\sigma T$ is the diffusion coefficient in σ-space and the noise in σ_i contributes to the non-conservative work rate on particle i in the form of an Itô-term proportional to the number of its neighbours:

$$\begin{aligned}
D_\sigma \partial_{\sigma_i} F_{\mathrm{nc},i} &= D_\sigma \partial_{\sigma_i} \sum_{j \neq i} \mathcal{T}(a_{ij}, \sigma_j - \sigma_i) = -\varepsilon D_\sigma n_i \\
n_i &= \sum_{j \neq i} \Theta(1 - a_{ij}).
\end{aligned} \tag{3.13}$$

During a phase separation, particles on the domain boundaries often carry higher non-conservative work rates since the differences between σ-values of neighbouring particles are more likely to be larger than within homogeneous domains, i.e. stronger synchronisation occurs on domain boundaries. To demonstrate this, we calculate the non-conservative work rates in a phase-separated configuration with a band shape. The non-conservative work rates in the unit of εD_σ are shown in Figure 3.5 (b) as average values of $\{\langle \dot{\Sigma}_i \rangle\}$ along the y-direction in the continuum limit

$$\dot{S}(x) = \frac{\int \mathrm{d}y \, p(x,y) \dot{\Sigma}(x,y)}{\int \mathrm{d}y \, p(x,y)}, \tag{3.14}$$

where $p(x, y)$ is the probability of finding a particle at (x, y) and $\dot{\Sigma}(x, y)$ is the non-conservative work rate there, such that the average non-conservative work rate $\dot{S}(x)$ is a function of x, the horizontal dimension in Figure 3.5 (a), a snapshot of a phase-separated configuration. A comparison between Figure 3.5 (a),(b) immediately shows that in x-direction, the averaged non-conservative work rate $\dot{S}(x)$ shoots up around the two domain boundaries. Besides, the averaged non-conservative work rates in the homogeneous regions are negligible compared to the boundaries, but are nonzero, since the non-conservative synchronisation maintains the homogeneity within the domain in the presence of noise.

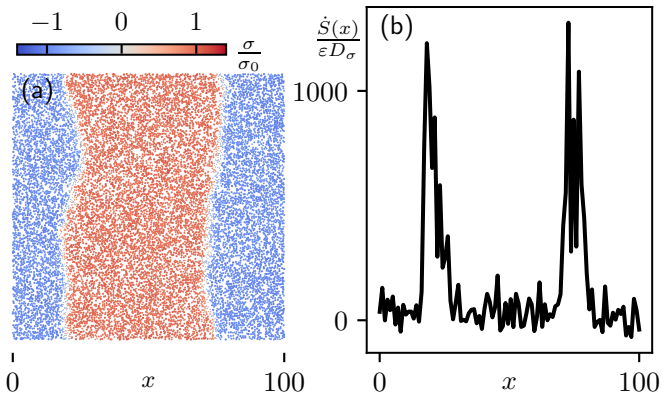

Figure 3.5: Non-equilibrium nature of phase separation: the non-conservative synchronisation creates and maintains a phase separation at transient level as a result of species interconversion through particle deformation during the domain growth procedure, see (a). The non-equilibrium nature is measured with the local non-conservative work rate $\dot{S}(x, y)$ at each point (x, y) in space. In (b), we show the rescaled average non-conservative work rate $\dot{S}(x)/\varepsilon D_\sigma$ over y as a function of x, the horizontal dimension in (a). Clearly, on the boundary of phase separation, one observes ultrahigh positive non-conservative work rate as a result of strong local synchronisation between particles carrying drastically different σ-values.

3.4 Asymmetric $V(\sigma)$: non-equilibrium phase diagrams

Having known the 3 stages of the relaxation from a disordered initial configuration, one would be interested in the effect of an asymmetric one-body potential on each relaxation stage and thus the steady state. Under strong synchronisation between neighbouring particles in the presence of repulsion between them, it is the shape of the one-body potential $V(\sigma)$ that determines the steady states. A simple way of tuning the shape of $V(\sigma)$ is to introduce *asymmetries* by rescaling. Instead of the symmetric one-body potential $V(\sigma)$, in the following the rescaled asymmetric potential

$$V_{\lambda_V,\lambda_\sigma}(\sigma) = \begin{cases} V(\sigma) & \sigma < 0 \\ \lambda_V V(\lambda_\sigma \sigma) & \sigma > 0 \end{cases} \tag{3.15}$$

is applied in the model (3.1). Its shape is shown in Figure 3.6. In $V_{\lambda_V,\lambda_\sigma}(\sigma)$, the stable radius and energetic stability of A-particles are made different from those of B-particles by simply setting $\lambda_\sigma \neq 1$ and $\lambda_V \neq 1$ respectively. Amongst the 3 stages of relaxation, we observe from simulations that both domain growth and coarsening are affected by the asymmetries in $V_{\lambda_V,\lambda_\sigma}$, leading to preferences for different steady states.

3.4.1 Domain growth: Kramer's escape

As is shown in Figure 3.7, during the domain growth stage, clusters of A- and B-particles expand without splitting or systematic displacement. Clearly, the dynamics in σ-space is much faster than particle displacement. In this context, we assume the dynamics in σ-space to be predominant and model the domain growth converting $\varnothing$-particles to either A- or B-particles using Kramers' escape problem [157, 158].
With fixed rescaling factors $\lambda_V, \lambda_\sigma$, one may compare the *net* conversion rate from $\varnothing$-particles to A-particles $k_{\varnothing A} - k_{A\varnothing}$ with that to B-particles $k_{\varnothing B} - k_{B\varnothing}$ by calculating the ratio

$$\begin{aligned} \frac{k_{\varnothing A} - k_{A\varnothing}}{k_{\varnothing B} - k_{B\varnothing}} &= \frac{\sqrt{\omega_{\varnothing,A}\omega_{\neq,A}}e^{-\beta(V_\varnothing - V_{\neq,A})} - \sqrt{\omega_A \omega_{\neq,A}}e^{-\beta(V_{\neq,A} - V_A)}}{\sqrt{\omega_{\varnothing,B}\omega_{\neq,B}}e^{-\beta(V_\varnothing - V_{\neq,B})} - \sqrt{\omega_B \omega_{\neq,B}}e^{-\beta(V_{\neq,B} - V_B)}} \\ &= \lambda_V \lambda_\sigma^2 e^{-\beta\Delta V(\lambda_V - 1)} \frac{\sqrt{2[(\sigma_0/\sigma_\neq)^2 - 1]} - e^{-\beta\Delta V \lambda_V (1-\alpha)}}{\sqrt{2[(\sigma_0/\sigma_\neq)^2 - 1]} - e^{-\beta\Delta V(1-\alpha)}}, \end{aligned} \tag{3.16}$$

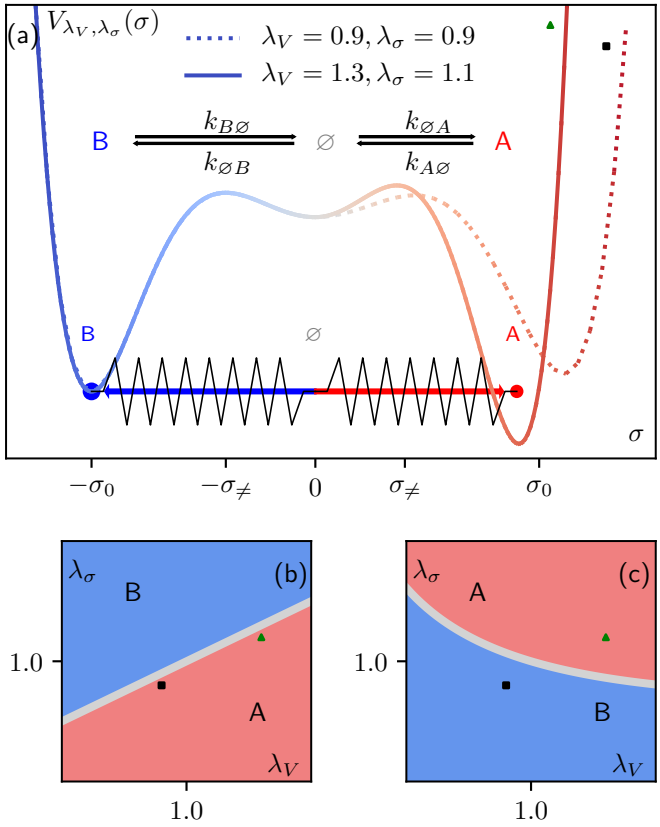

Figure 3.6: (a) Two examples of the asymmetric one-body potential $V_{\lambda_V,\lambda_\sigma}$ with rescaling factors $\lambda_V = 0.9, \lambda_\sigma = 0.9$ (dotted) and $\lambda_V = 1.3, \lambda_\sigma = 1.1$ (solid). The reversible conversion between $\varnothing$-particles and A- or B-particles during domain growth is modelled using classical Kramer's escape problem. The asymmetry in $V_{\lambda_V,\lambda_\sigma}$ creates a difference between the net rates of conversion to A- and B-particles, leading to a bipartite schematic phase diagram (c). During coarsening, the energetic advantage created by $\lambda_V \neq 1$ together with the advantage of large particles resulting from $\lambda_\sigma \neq 1$ leads to another bipartite schematic phase diagram (b). The spring represents the effective restoring force in σ-dynamics, due to synchronisation of σ-values between neighbouring particles: the strength of this force depends on the location difference between the minima in the one-body potential landscape $V_{\lambda_V,\lambda_\sigma}$. The combination of schemes (b) and (c) is expected to qualitatively reproduce the shape of the phase diagram and understand the effect of asymmetries in $V_{\lambda_V,\lambda_\sigma}$.

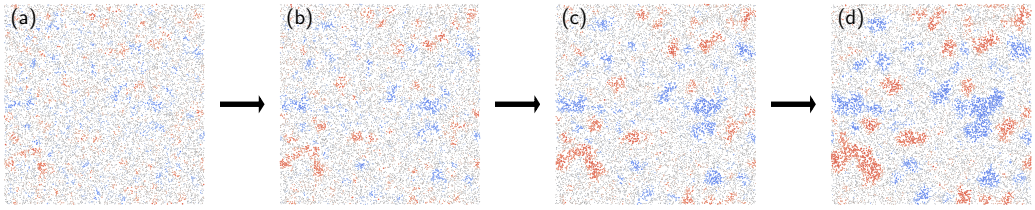

Figure 3.7: Snapshots (a)-(d) during the domain growth stage. Clusters of A- and B-particles grow without splitting or significant migration.

where

$$\begin{aligned} \omega_A &= V''_{\lambda_V,\lambda_\sigma}\left(\frac{\sigma_0}{\lambda_\sigma}\right), \qquad \omega_B = V''_{\lambda_V,\lambda_\sigma}(-\sigma_0), \\ \omega_{\varnothing,A} &= V''_{\lambda_V,\lambda_\sigma}(0_+), \qquad \omega_{\varnothing,B} = V''_{\lambda_V,\lambda_\sigma}(0_-), \\ \omega_{\neq,A} &= V''_{\lambda_V,\lambda_\sigma}\left(\frac{\sigma_{\neq}}{\lambda_\sigma}\right), \quad \omega_{\neq,B} = V''_{\lambda_V,\lambda_\sigma}(-\sigma_{\neq}), \end{aligned} \tag{3.17}$$

and

$$\begin{aligned} V_{\neq,A} &= V_{\lambda_V,\lambda_\sigma}\left(\frac{\sigma_{\neq}}{\lambda_\sigma}\right), \quad V_{\neq,B} = V_{\lambda_V,\lambda_\sigma}(-\sigma_{\neq}), \\ V_{\varnothing} &= V_{\lambda_V,\lambda_\sigma}(0), \qquad V_A = V_{\lambda_V,\lambda_\sigma}\left(\frac{\sigma_0}{\lambda_\sigma}\right), \\ V_B &= V_{\lambda_V,\lambda_\sigma}(-\sigma_0), \qquad \Delta V = V_{\varnothing} - V_B = \frac{3v_0\sigma_0^4}{2}(\sigma_0^2 - 3\sigma_{\neq}^2). \end{aligned} \tag{3.18}$$

The calculation of the ratio (3.16) between net conversion rates leads to a qualitative phase diagram Figure 3.6 (c). On the gray hyperbola, the net conversion rates $k_{\varnothing A} - k_{A\varnothing}, k_{\varnothing B} - k_{B\varnothing}$ are equal. This hyperbola separates the phase diagram into two regions. Above the hyperbola, the net conversion rate to A-particles is larger than to B-particles, whereas below is the conversion to B-particles relatively faster. The slower the conversion is, the more likely the final species will be in a bubble, which is expected to be unstable under the symmetric one-body potential V.

3.4.2 Coarsening: stabilising bubbles

Interestingly, the instability of bubbles can be lifted by asymmetries in $V_{\lambda_V,\lambda_\sigma}$. This involves the coarsening stage into the determination of steady states, as now bubbles are no longer necessarily unstable. Also, while bands are long-lived under symmetric one-body potentials, they can be short-lived when asymmetries occur in $V_{\lambda_V,\lambda_\sigma}$.

To examine the stability of bubbles, we perform particle-based simulations starting from phase-separated configurations. In each of these initial configurations, a bubble of an initial radius R_{ini} exists to contain A-particles (resp. B-particles). Outside the bubble are B-particles (resp. A-particles). Through such simulations, the stabilities of bubbles of different sizes under different asymmetries are investigated by measuring the probability of different steady states respectively.

Figure 3.8 depicts the results of those simulations. By tuning λ_σ with $\lambda_\sigma = 1$ being fixed, one can easily tell from Figure 3.8 (a,b) that energetic advantage can stabilise bubbles. When $\lambda_V < 1$, B-particles are energetically more stable, enabling large bubbles of B-particles to expand by converting the A-particles and ∅-particles outside the bubble into B-particles. When $\lambda_V > 1$, A-particles are energetically more stable, driving the expansion of sufficiently large bubbles of A-particles. In both cases, $|\lambda_V - 1|$ measures the deviation from energetic degeneracy between A- and B-particles. The larger its value is, the more energetic difference there is and a smaller radius is required, above which the bubbles can be stable and expand.

Moreover, fixing $\lambda_V = 1$, simulations at different λ_σ-values show an unexpected effect: the advantage of larger particles that can stabilise bubbles. As is shown in Figure 3.8 (c,d), when $\lambda_\sigma > 1$, B-particles are in general larger than A-particles, which can stabilise a sufficiently large bubble of B-particles by making it expand. When $\lambda_\sigma < 1$, A-particles are in general larger than B-particles, allowing sufficiently large bubble of A-particles to expand and not to shrink. This advantage of larger particles has its origin in the strong synchronisation $\mathcal{T}$. On the domain boundary, the ∅-particles bear synchronisation interactions from particles inside and outside the bubble. Since the magnitude of synchronisation interaction is proportional to the difference in σ-values, larger particles can exert stronger synchronisation interaction on ∅-particles, making them more likely to be converted into the species with larger stable size.

Unlike the effect of energetic advantages, the effect of the advantage of larger particles is not symmetric with respect to the symmetric one-body potential. More specifically, when $\lambda_\sigma < 1$, this effect can saturate and thus become non-monotonic. See Figure 3.8 (d). Since the advantage of larger particles is induced by synchronisation, converting ∅-particles into the species with a larger stable size increases the global packing fraction and thus leads to a higher repulsive energy cost, which is unfavoured. Since λ_σ only controls the stable size of A-particles, the global packing fraction is higher at $\lambda_\sigma < 1$ than at $\lambda_\sigma > 1$. A higher global packing fraction enlarges the effect of repulsion in hindering the advantage of larger particles.

Based on the above results about the effect of asymmetric energetics ($\lambda_V \neq 1$)

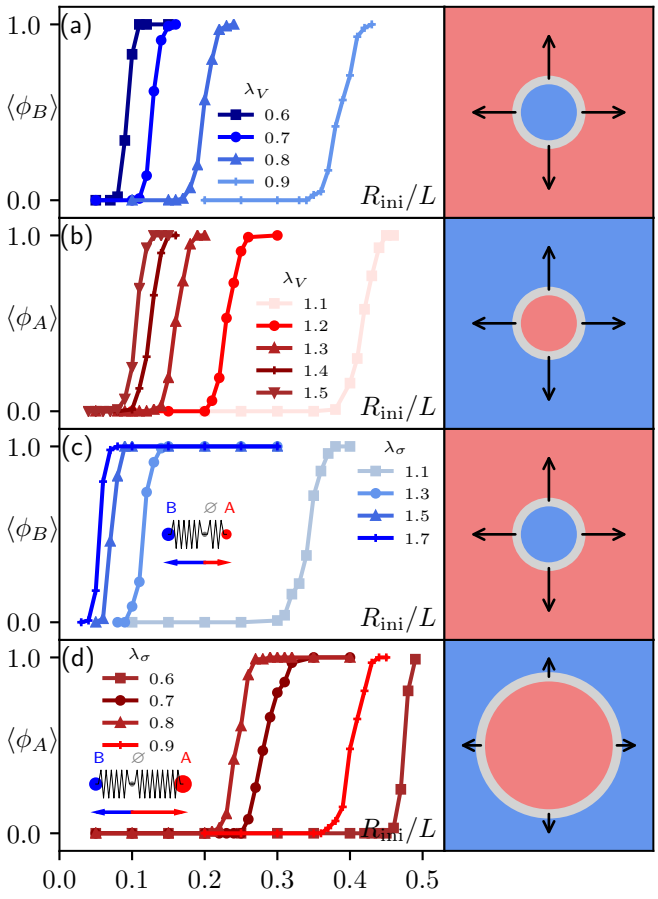

Figure 3.8: Fractions of trajectories in which bubbles expand. (a,b) Bubbles of energetically favoured particles with radii larger than a critical radius become stable with $\lambda_\sigma = 1$ being fixed. (c,d) Besides, bubbles of particles with larger stable sizes can be stable if they are sufficiently large, with $\lambda_V = 1$ being fixed. Such an advantage of large particle can be hindered by large repulsive energy cost, thus can reach a saturation when $\lambda_\sigma < 1$. All measurements are performed in a square box of edge size $L = 100\sigma_0$ initialised to be phase-separated, with bubbles containing only particles with (a,c) $\sigma = -1$ (b,d) $\sigma = 1$ and particles of (a,c) $\sigma = 1$, (b,d) $\sigma = -1$ outside the bubbles, in the absence of particles of other σ-values, with $\sigma_0 = 1, \sigma_{\neq} = 0.4\sigma_0, \rho = 1.4, v_0 = 60, T = 5, \mu = 1, \mu_\sigma = 0.1$ and $u_0 = 0.0001$.

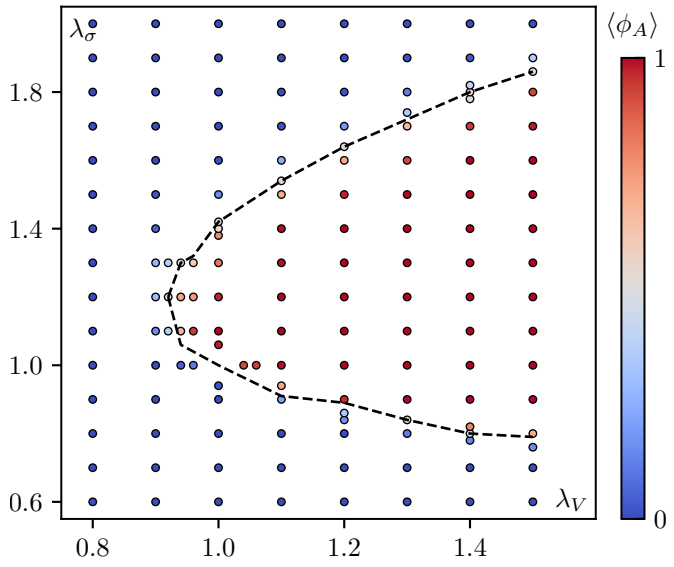

Figure 3.9: Phase diagram measured by particle-based simulations in terms of the fraction of trajectories $\langle\phi_A\rangle$ ending up with a steady state full of A-particles. Each point is measured as an average over 100 trajectories with identical setup. A convex phase boundary (black dashed) separates the phase diagram into a phase favouring the steady state full of B-particles (left, blue) and a phase favouring the steady state full of A-particles (right, red). All measurements are performed in a square box of edge size $L = 100\sigma_0$ initialised with equal amount of particles with $\sigma = \pm 1$ uniformly distributed in the square box in the absence of particles with other σ-values, with $\sigma_0 = 1, \sigma_{\neq} = 0.4\sigma_0, \rho = 1.4, v_0 = 60, T = 5, \mu = 1, \mu_\sigma = 0.1$ and $u_0 = 0.0001$. Here $\alpha = 0.12$.

and the advantage of larger particles ($\lambda_\sigma \neq 1$), a qualitative phase diagram Figure 3.6 (b) can be sketched. This phase diagram features a tilted gray line separating the phase diagram into two regions. Above this line, sufficiently large bubbles of B-particles can be stable, whereas below this line, sufficiently large bubbles of A-particles can expand. This phase diagram sketches the effect of coarsening on determining the steady states.

3.4.3 Phase diagrams of steady states

A combination of the two phase diagrams Figure 3.6 (b,c) should in principle qualitatively predict the shape of the phase diagram measured by particle-based simulations. To confirm this, a phase diagram is measured at $\alpha = 0.12$,

which is shown in Figure 3.9. This phase diagram features a phase boundary separating the two phases. On the right of the boundary, A-particles are more likely to be in the steady state, whereas on the left, steady states full of B-particles are more probable. The shape of this phase boundary can be understood as a combination of the phase boundaries in Figure 3.6 (b,c). The comparison shows that the upper half is mainly controlled by coarsening, whilst the lower half is predominantly controlled by domain growth. Since the advantage of larger particles can saturate when $\lambda_\sigma < 1$, the weight of coarsening in determining the steady state should be reduced in the lower half. In the upper half, bubbles can be stable even at very small sizes under strong asymmetries, thus coarsening outweighs domain growth there.

The role of metastabilities: varying α Within the regime of binary mixtures ($\alpha < 0.34$), the influence of different metastabilities is another essential aspect of the one-body potential, since the stability of $\varnothing$-particles measures the strength of absorption of the effective particle reservoir. To probe its effect, a phase diagram is measured with particle-based simulations at $\alpha = 0.23$, see Figure 3.10 (a). Clearly, the upper half of the phase boundary is shifted to higher λ_σ-values and lower λ_V-values, whilst the lower half rises to higher λ_σ-values. It is natural to investigate how a higher α-value impacts domain growth and coarsening. The effect of higher α-values on domain growth can be read off from Equation (3.16). Plugging larger α-values into Equation (3.16) recovers the rise of the lower half of the phase boundary. Besides, the effect of larger α on coarsening is reflected by the stability of bubbles at $\alpha = 0.23$ in comparison to that at $\alpha = 0.12$, see Figure 3.10 (b,c). Again, energetic difference and the advantage of larger particles can stablise bubbles, with critical radii almost unchanged. To maintain a compromise with domain growth, the upper half of the phase boundary has to be shifted towards higher λ_σ-values.

3.5 Field-theoretical treatment

3.5.1 Effective dynamics via mean-field approximations

Like for PAM (see Section 2.4), one should work with an effective model of particle-based dynamics, which is an approximate model of (3.1), in order to circumvent the WCA-type repulsion U.
Starting from (3.1), the contribution from U to particle translation is neglected, as it homogenises the configuration like a zero-mean noise does. The

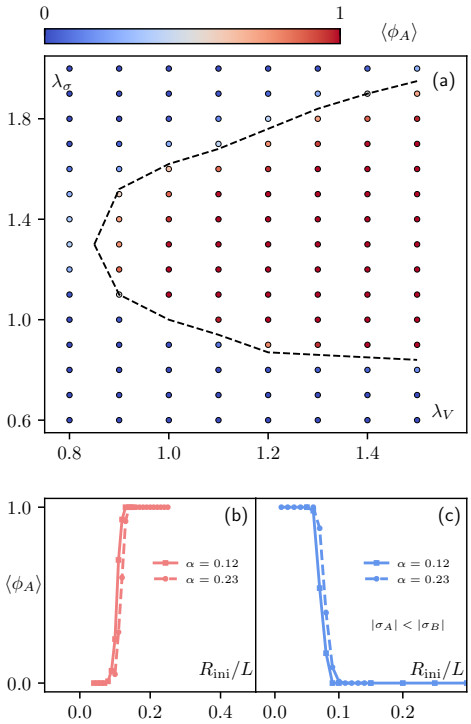

Figure 3.10: (a) Phase diagram measured by particle-based simulations in terms of the fraction of trajectories $\langle\phi_A\rangle$ reaching a steady state full of A-particles. Each point is measured as an average over 100 parallel trajectories. A phase boundary (black dashed) separates the phase diagram into a phase favouring the steady state full of B-particles (left, blue) and a phase favouring the steady state full of A-particles (right, red). All measurements are performed in a square box of edge size $L = 100\sigma_0$ initialised with equal amount of particles with $\sigma = \pm 1$ uniformly distributed in the square box in the absence of particles with other σ-values, with $\sigma_0 = 1, \sigma_{\neq} = 0.45\sigma_0, \rho = 1.4, v_0 = 60, T = 5, \mu = 1, \mu_\sigma = 0.1$ and $u_0 = 0.0001$. Here $\alpha = 0.23$. (b) Fractions of trajectories $\langle\phi_A\rangle$ reaching a steady state with A-particles over 100 parallel trajectories for each initial radius of bubble composed of A-particles at $\lambda_V = 1.5, \lambda_\sigma = 1$, showing the stabilities of bubbles with different initial radii composed of energetically favoured particles. (c) Fractions of trajectories $\langle\phi_A\rangle$ reaching a steady state with A-particles over 100 parallel trajectories for each initial radius of bubble composed of B-particles at $\lambda_V = 1, \lambda_\sigma = 1.5$, illustrating the stabilities of bubbles with different initial radii composed of larger particles. Both the energetic preference and advantage of larger particles are almost unchanged by stabilising ∅-particles.

resulting particle translation thus becomes purely noisy

$$\dot{\mathbf{r}}_i = \sqrt{2\mu T}\boldsymbol{\xi}_i. \tag{3.19}$$

On the other hand, the contribution of U to particle deformation should be approximated using the product rule, such that one obtains

$$\sum_j \partial_{\sigma_i} U(a_{ij}) \simeq (\partial_\varphi U) \sum_j (\partial_{\sigma_j}\varphi)\,\Theta(1-a_{ij}), \tag{3.20}$$

where $\varphi = \pi \sum_i \sigma_i^2/L^2$ is the packing fraction. In a dense synchronised assembly, like in PAM, the factor $\partial_\varphi U$ may be approximated to be a constant. Also, $\partial_{\sigma_i}\varphi$ brings a σ_i-linear factor. By evaluating $\partial_{\sigma_i}\varphi$ at particle j's position, we arrive at

$$\sum_j \partial_{\sigma_i} U(a_{ij}) \simeq C \sum_j \sigma_j \Theta(1-a_{ij}) \tag{3.21}$$

with $C = 2\pi\partial_\varphi U/L^2$ being a constant factor. Applying the approximated contribution (3.21) of U to the model (3.1) leads to the following dynamics

$$\begin{aligned}\dot{\sigma}_i = &\sum_{j\neq i} \mu_\sigma \Big[\varepsilon(\sigma_j - \sigma_i) - C\sigma_j\Big]\Theta(1-a_{ij}) \\ &- \mu_\sigma \frac{\mathrm{d}}{\mathrm{d}\sigma_i} V_{\lambda_V,\lambda_\sigma}(\sigma_i) + \sqrt{2\mu_\sigma T}\eta_i\end{aligned} \tag{3.22}$$

In the continuum limit, the Heaviside kernel may be approximated by a delta-kernel $\delta(\mathbf{r}_j - \mathbf{r}_i)$. We here define two hydrodynamic fields that are central to the continuum model

$$\begin{aligned}\rho(\mathbf{r},t) &= \sum_i \delta(\mathbf{r}-\mathbf{r}_i) \\ \overline{\sigma}(\mathbf{r},t) &= \sum_i \sigma_i \delta(\mathbf{r}-\mathbf{r}_i),\end{aligned} \tag{3.23}$$

namely the local density field ρ and the local magnetisation field $\overline{\sigma}$. The approximation in Equation (3.21) in fact maps the dynamics into an effective equilibrium

$$\begin{aligned}\dot{\sigma}_i &= \sum_{j\neq i} \mu_\sigma \Big[\varepsilon(\sigma_j - \sigma_i) - C\sigma_j\Big]\delta(\mathbf{r}_j - \mathbf{r}_i) \\ &\quad - \mu_\sigma \frac{\mathrm{d}}{\mathrm{d}\sigma_i} V_{\lambda_V,\lambda_\sigma}(\sigma_i) + \sqrt{2\mu_\sigma T}\eta_i \\ &= \mu_\sigma \Big[\varepsilon(\overline{\sigma} - \rho\sigma_i) - C\overline{\sigma}\Big] - \mu_\sigma \frac{\mathrm{d}}{\mathrm{d}\sigma_i} V_{\lambda_V,\lambda_\sigma}(\sigma_i) + \sqrt{2\mu_\sigma T}\eta_i \\ &= -\mu_\sigma \partial_{\sigma_i} \tilde{V}_{\lambda_V,\lambda_\sigma}(\sigma_i;\overline{\sigma}) + \sqrt{2\mu_\sigma T}\eta_i,\end{aligned} \tag{3.24}$$

which is subject to an effective one-body potential

$$\tilde{V}_{\lambda_V,\lambda_\sigma}(\sigma;\overline{\sigma}) = V_{\lambda_V,\lambda_\sigma}(\sigma) + \frac{\varepsilon\rho}{2}\sigma^2 - (\varepsilon - C)\overline{\sigma}\sigma. \tag{3.25}$$

In the following, the particle-based model (3.19),(3.24) in an effective equilibrium is coarse-grained to achieve a continuum description.

3.5.2 Derivation of field equations

Similar to the coarse-graining procedure of PAM, we introduce an empirical distribution

$$f(\mathbf{r},\sigma,t) = \sum_i \delta(\mathbf{r} - \mathbf{r}_i(t))\delta(\sigma - \sigma_i(t)) \tag{3.26}$$

as the central object of a continuum description. The equation it satisfies should be derived systematically *à la Dean*[20]. The resulting equation reads

$$\begin{aligned}\partial_t f(\mathbf{r},\sigma,t) = {}& \mu_\sigma\partial_\sigma[f\partial_\sigma\tilde{V}_{\lambda_V,\lambda_\sigma}(\sigma;\overline{\sigma})] + \mu_{\mathbf{r}}T\partial^2_{\mathbf{rr}}f + \mu_\sigma T\partial^2_{\sigma\sigma}f \\ & + \partial_{\mathbf{r}}\cdot[\sqrt{2\mu_{\mathbf{r}}Tf}\Lambda_{\mathbf{r}}] + \partial_\sigma[\sqrt{2\mu_\sigma Tf}\Lambda_\sigma].\end{aligned} \tag{3.27}$$

To follow the line of mean-field dynamics, one should neglect the noises $\Lambda_{\mathbf{r}}, \Lambda_\sigma$ here, rendering Equation (3.27) deterministic:

$$\partial_t f(\mathbf{r},\sigma,t) = \mu_\sigma\partial_\sigma[f\partial_\sigma\tilde{V}_{\lambda_V,\lambda_\sigma}(\sigma;\overline{\sigma})] + \mu_{\mathbf{r}}T\partial^2_{\mathbf{rr}}f + \mu_\sigma T\partial^2_{\sigma\sigma}f \tag{3.28}$$

In a continuum model, the hydrodynamic fields defined in Equation (3.23) are recasted in terms of f:

$$\begin{aligned}\rho &= \int \mathrm{d}\sigma\, f(\mathbf{r},\sigma,t)\ , \\ \overline{\sigma} &= \int \mathrm{d}\sigma\, \sigma f(\mathbf{r},\sigma,t)\ .\end{aligned} \tag{3.29}$$

Plugging the definitions (3.29) into the noiseless hydrodynamic equation (3.28) gives the field equations

$$\begin{aligned}\partial_t\rho &= D\partial^2_{\mathbf{rr}}\rho \\ \partial_t\overline{\sigma} &= D\partial^2_{\mathbf{rr}}\overline{\sigma} - \mu_\sigma\overline{\partial_\sigma\tilde{V}_{\lambda_V,\lambda_\sigma}},\end{aligned} \tag{3.30}$$

where $D = \mu T$ is the diffusion coefficient and $\overline{O} = \int \mathrm{d}\sigma\, O f(\mathbf{r},\sigma,t)$ for a generic observable O. The density field obeys purely diffusive dynamics without coupling with other fields. In a steady state it should be seen as homogeneous and takes the system density value everywhere. Hence only the

field equation of $\overline{\sigma}$, which is explicitly of non-conserved type (Model A, see Subsection 1.2.1), deserves further attention. The reaction term $\overline{\partial_\sigma \tilde{V}_{\lambda_V,\lambda_\sigma}}$, however, involves the information about higher moments $\overline{\sigma^{n>1}}$, keeping the field equation unclosed. Closing the field equation through truncation would at least require a non-vanishing $\overline{\sigma^5}$-field to be involved in order to preserve the triple-well shape of $V_{\lambda_V,\lambda_\sigma}$. This would be computationally expensive, whilst still not ensured to be effective.
Remembering that the particle-based model have been mapped to an effective equilibrium before coarse-graining, one may apply a *biased local-equilibrium Ansatz*

$$\begin{aligned} f &\simeq \mathcal{Z}^{-1}(\overline{\sigma}) e^{-\beta(\tilde{V}_{\lambda_V,\lambda_\sigma}(\sigma;\overline{\sigma})-\lambda(\overline{\sigma})\sigma)} \\ \mathcal{Z}(\overline{\sigma}) &= \int \mathrm{d}\sigma\, e^{-\beta(\tilde{V}_{\lambda_V,\lambda_\sigma}(\sigma;\overline{\sigma})-\lambda(\overline{\sigma})\sigma)}, \end{aligned} \tag{3.31}$$

in which the empirical distribution f bears the form of a Gibbs measure with respect to $\tilde{V}_{\lambda_V,\lambda_\sigma}$ linearly biased by $\lambda(\overline{\sigma})\sigma$. Through this Ansatz, one writes down a self-consistent definition of $\overline{\sigma}$

$$\overline{\sigma} = \mathcal{Z}^{-1}(\overline{\sigma}) \int \mathrm{d}\sigma\, \sigma e^{-\beta(\tilde{V}_{\lambda_V,\lambda_\sigma}(\sigma;\overline{\sigma})-\lambda(\overline{\sigma})\sigma)}, \tag{3.32}$$

through which the shape of $\lambda(\overline{\sigma})$ is implicitly determined.
Applying this Ansatz to the evaluation of the reaction term $\overline{\partial_\sigma \tilde{V}_{\lambda_V,\lambda_\sigma}}$ gives

$$\overline{\partial_\sigma \tilde{V}_{\lambda_V,\lambda_\sigma}} = \int \mathrm{d}\sigma\, \partial_\sigma \tilde{V}_{\lambda_V,\lambda_\sigma} \mathcal{Z}^{-1}(\overline{\sigma}) e^{-\beta(\tilde{V}_{\lambda_V,\lambda_\sigma}(\sigma;\overline{\sigma})-\lambda(\overline{\sigma})\sigma)} = \lambda(\overline{\sigma}), \tag{3.33}$$

which fully closes the field equation of $\overline{\sigma}$

$$\partial_t \overline{\sigma} = D\partial^2_{\mathbf{rr}} \overline{\sigma} - \mu_\sigma \lambda(\overline{\sigma}), \tag{3.34}$$

The fully closed field equation (3.34), $\lambda(\overline{\sigma})$ being determined by Equation (3.32), gives the field dynamics to be examined in the following free-energetic analysis.

3.5.3 Effective free energy

In an effective equilibrium, the field equation (3.34) indicates an underlying *effective free energy* of Model-A type

$$\mathcal{F}[\overline{\sigma}] = \int \mathrm{d}\mathbf{r} \left(\frac{D}{2\mu_\sigma} (\partial_\mathbf{r} \overline{\sigma})^2 + F(\overline{\sigma}) \right). \tag{3.35}$$

By penalising inhomogeneties, the Model-A-like free energy (3.35) promotes homogeneous steady-state configurations. Hence only the homogeneous free energy $F(\overline{\sigma})$ should be investigated for steady states.
This homogeneous free energy F, compared to the field equation (3.34), is exclusively determined by $\lambda(\overline{\sigma})$

$$F(\overline{\sigma}) = \int_{-\infty}^{\overline{\sigma}} \lambda(\sigma')\,\mathrm{d}\sigma'\,. \tag{3.36}$$

Knowing that the steady states are homogeneous, analysing the field equation (3.34) is then reduced to analysing the shape of $F(\overline{\sigma})$. This requires the determination of $\lambda(\overline{\sigma})$ beforehand, which can be done numerically using Equation (3.32).
At each $\overline{\sigma}$-value, the solution starts with an initial guess $\lambda = \lambda_0$. Through a standard Gradient Descent (GD) Algorithm 4, the bias $\lambda_n \to \lambda_{n+1}$ should be updated. A cost function $\mathcal{L}_\lambda$ is calculated to quantify the distance of the $\overline{\sigma}$-value computed with λ away from the true value of $\overline{\sigma}$. This iterative process stops when λ reaches the true $\lambda(\overline{\sigma})$-value at the given $\overline{\sigma}$-value through gradient descent, up to a small threshold of the cost function, *i.e.* when $\mathcal{L} < \mathcal{L}_{\text{threshold}}$. At $\overline{\sigma} = 0$, the effective potential $\tilde{V}$ is an even function of σ. Immediately, one knows $\lambda(0) = 0$. Therefore, at small $\overline{\sigma}$, one may start the numerical iteration from $\lambda_0 = 0$. Assuming the continuity of $\lambda(\overline{\sigma})$, we use the final value of λ computed at $\overline{\sigma}$ as the initial guess at $\overline{\sigma} + \mathrm{d}\overline{\sigma}$. Looping over all $\overline{\sigma}$-values in a chosen range determines the shape of $\lambda(\overline{\sigma})$ in the corresponding $\overline{\sigma}$-interval. Integrating the obtained $\lambda(\overline{\sigma})$ according to (3.36) gives the shape of the homogeneous free energy F.

3.5.4 Phase transitions

The shape of F is subjected to the asymmetries in V. In terms of global minima $\overline{\sigma}_{\min} = \arg\min F(\overline{\sigma})$, which is a function of the rescaling factors $\lambda_V, \lambda_\sigma$, a phase diagram is plotted at $\alpha = 0.12$. Remarkably, the phase diagram Figure 3.11 (a) qualitatively reproduces the shape of the phase diagram Figure 3.9 measured by particle-based simulations, with A-rich and B-rich phases corresponding here respectively to $\sigma_{\min} > 0$ and $\sigma_{\min} < 0$.
Based on the phase diagram, the natures of transitions across different segments of the phase boundary can be investigated, since the number of local minima in F can be readily seen. This is done by measuring the shapes of F at the points along a line across the phase boundary. The results are shown in Figure 3.11 (b,c). Along the red arrow, the transition is clearly discontinuous in $\sigma_{\min}$-value, as the homogeneous free energy F has two minima around

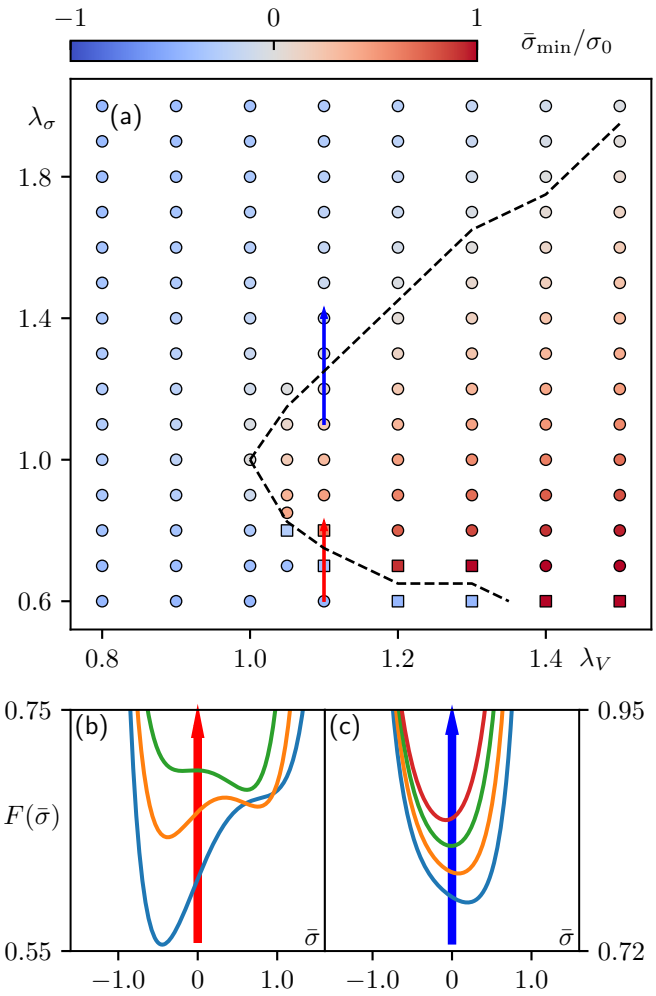

Figure 3.11: (a) The underlying phase diagram of Equation (3.34) at $\alpha = 0.12$ in terms of the global minimum $\overline{\sigma}_{\min}$ of the homogeneous free energy $F(\overline{\sigma})$ as a function of rescaling factors $\lambda_V, \lambda_\sigma$. Here, circles and squares refer to effective free energies with single or double local minima. The dashed line separates the region of $\overline{\sigma}_{\min} > 0$ from $\overline{\sigma}_{\min} < 0$. (b) Homogeneous free energy plots $F(\overline{\sigma})$ of points in the phase diagram (a) along the red arrow. (c) Homogeneous free energy plots $F(\overline{\sigma})$ of points in phase diagram (a) along the blue arrow. All predictions are performed with $\sigma_0 = 1, \sigma_{\neq} = 0.4\sigma_0, C = 0, \varepsilon = 1, v_0 = 60$, and $\mu_\sigma = 0.1$.

Algorithm 4: GD algorithm determining $\lambda(\overline{\sigma})$

Data: $\overline{\sigma}$
Result: $\lambda(\overline{\sigma})$
$\overline{\sigma} \leftarrow \overline{\sigma}$;
$\lambda \leftarrow \lambda_0$;
$\mathcal{L}_\lambda \leftarrow 1$;
while $\mathcal{L}_\lambda \geq \mathcal{L}_{\text{threshold}}$ **do**
  $\lambda \leftarrow \lambda - \alpha \partial_\lambda \mathcal{L}_\lambda$;
  $\mathcal{Z}_\lambda \leftarrow \int \mathrm{d}\sigma \, e^{-\beta(\tilde{V}(\sigma;\overline{\sigma})-\lambda\sigma)}$;
  $\langle\sigma\rangle \leftarrow \mathcal{Z}_\lambda^{-1} \int \mathrm{d}\sigma \, \sigma e^{-\beta(\tilde{V}(\sigma;\overline{\sigma})-\lambda\sigma)}$;
  $\mathcal{L}_\lambda \leftarrow \frac{1}{2}(\langle\sigma\rangle - \overline{\sigma})^2$;
end
$\lambda(\overline{\sigma}) \leftarrow \lambda$;

the phase boundary and their relative stabilities exchange when crossing the phase boundary-Figure 3.11 (b). In contrast, along the blue arrow, the shape of F is convex, featuring a single minimum which changes its sign across the phase boundary via continuous shifts-Figure 3.11 (c). This is quantitatively reflected by the smooth evolution of $\overline{\sigma}_{\text{min}}$-value along the blue arrow in the phase diagram.
Similar to the L-G scheme discussed in Subsection 1.2.1, the transition along the red arrow featuring a discontinuous shift in $\overline{\sigma}_{\text{min}}$-value should be first-order, since the underlying double-well homogeneous free energy F undergoes an exchange of local minima stabilities. Such a scheme of transition occurs across the phase boundary in the region where F has two local minima. This region is upper-bounded in the positive $\overline{\sigma}_{\text{min}}$ region and lower-bounded in the negative $\overline{\sigma}_{\text{min}}$ region. Beyond this upper- and lower-bounded region F has only a single minimum. The upper- and lower-boundaries of the region allowing double minima in F merge at a critical point. See Figure 3.12. From Figure 3.11 (a) one may roughly recognise that this point lies around $(\lambda_V, \lambda_\sigma) = (1.05, 0.8)$. Locating the point more precisely requires a zoom-in of the phase diagram. Here, the region $[1.0, 1.1] \times [0.7, 0.9]$ is chosen for finer measurement, see Figure 3.12. In this region of phase diagram, a region featuring double minima in F is lower- and upperbounded, with the two boundaries approaching each other. The intersection point of these two boundaries closes such a region, and thus is the critical point being looked for, which is located at $(\lambda_V, \lambda_\sigma) = (1.025 \pm 0.005, 0.869 \pm 0.007)$.

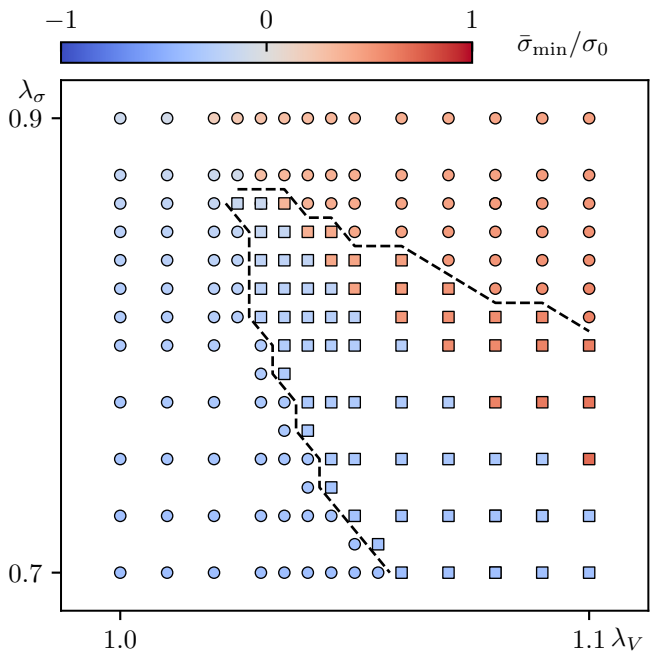

Figure 3.12: Zoom-in of the phase diagram Figure 3.11 (a) in the region $[1.0, 1.1]\times[0.7, 0.9]$. First-order phase transitions are observed only within the region in which the homogeneous free energy $F(\overline{\sigma})$ has two minima (square points). This region is closed at $(\lambda_V, \lambda_\sigma) = (1.025 \pm 0.005, 0.869 \pm 0.007)$ where its upper and lower boundaries (black dashed lines) intersect at a critical point. All predictions are performed with $\sigma_0 = 1, \sigma_{\neq} = 0.4\sigma_0, C = 0, \varepsilon = 1, v_0 = 60$, and $\mu_\sigma = 0.1$.

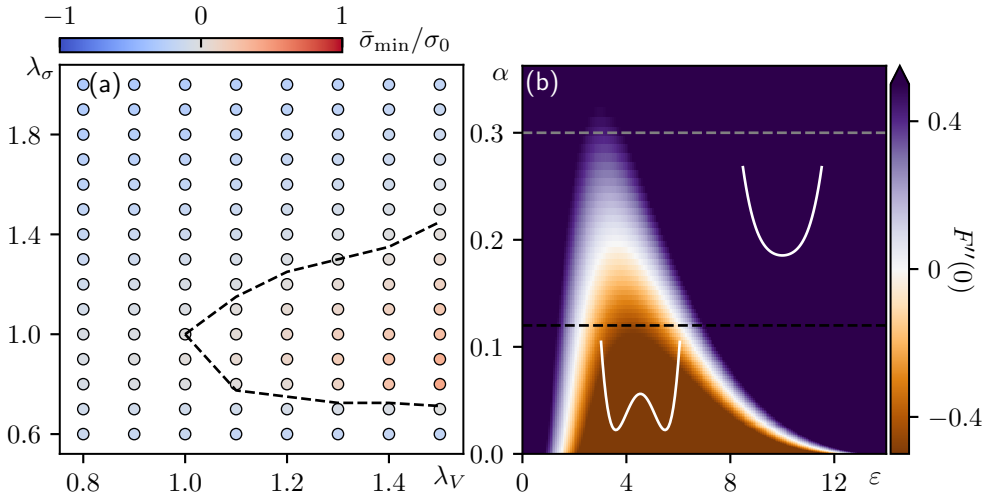

Figure 3.13: (a) The underlying phase diagram of Equation (3.34) at $\alpha = 0.3$. The rise of the lower branch of the boundary together with the reduced slope of the upper branch makes the region favouring $\overline{\sigma}_{\min} > 0$ narrower compared to $\alpha = 0.12$. The first-order phase transition disappears within the range of this phase diagram. (b) Colour map of the linear coefficient $F''(0) = \lambda'(0)$ of as a function of ε and α measured numerically at $C = 0$. In the bounded region where $F''(0) < 0$, the free energy F has two local minima. Outside this region, the free energy has only one single minimum. The points satisfying $F''(0) = 0$ spans the boundary line which is a critical line (white). It is clear that large α and large ε both lead to positive $F''(0)$. At $\alpha = 0.12$ (black dashed line), $F''(0) < 0$ roughly within $2 < \varepsilon < 6$. At $\alpha = 0.3$ (gray dashed line), the range of ε allowing double minima in F is closed. All predictions for $\alpha = 0.3$ are performed with $\sigma_0 = 1, \sigma_{\neq} = 0.473\sigma_0, C = 0, \varepsilon = 1, v_0 = 60$, and $\mu_\sigma = 0.1$.

3.5.5 The role of metastability

In the context of field theories, we are also interested in the effect of changing α-values, in parallel with particle-based simulations. The change it brings to the phase diagram measures the descriptive power of the field-theoretic model. In Figure 3.13 (a), a phase diagram is measured at $\alpha = 0.3$, a higher α-value. One may still claim that it qualitatively recovers the phase diagram of particle-based simulations. In particular, the rise of the lower branch of the boundary agrees with the observation in particle-based simulations when strengthening the stablising $\varnothing$-particles. However, the upper branch of the boundary in Figure 3.13 (a) has a reduced slope compared to $\alpha = 0.12$, which does not agree with the observations in particle-based simulations.

Moreover, within the range of λ_V under investigation, F is always convex, i.e. only crossovers take place.
Understanding the disappearance of first-order phase transitions entails figuring out the conditions of double minima in F. For simplicity, the discussion is restricted to the symmetric one-body potential with $\lambda_V = \lambda_\sigma = 1$. Under this condition, one can immediately find a root $\lambda(0) = 0$ of the self-consistent relation (3.32) analytically using symmetry arguments. Thus $\overline{\sigma} = 0$ is a stationary point of F. To allow double minima, it has to be a local maxima, i.e. $F''(0) = \lambda'(0) < 0$.
To find the conditions for $\lambda'(0) < 0$, the effective equilibrium potential in the Ansatz (3.31) should be regrouped:

$$\tilde{V}_{1,1}(\sigma;\overline{\sigma}) - \lambda(\overline{\sigma})\sigma = \mathcal{V}_\varepsilon(\sigma) - \nu(\overline{\sigma})\sigma \ , \tag{3.37}$$

where an effective σ-symmetric potential

$$\mathcal{V}_\varepsilon(\sigma) = \tilde{V}_{1,1}(\sigma;\overline{\sigma}) + \frac{\varepsilon\rho\sigma^2}{2} \tag{3.38}$$

is introduced, such that $\lambda(\overline{\sigma})$ is linearly biased to be

$$\nu(\overline{\sigma}) = \lambda(\overline{\sigma}) + (\varepsilon - C)\overline{\sigma}. \tag{3.39}$$

We plug Equation (3.37) into the self-consitent definition (3.32) of $\overline{\sigma}$ to obtain

$$\overline{\sigma} = \frac{\int \mathrm{d}\sigma\, \sigma e^{-\beta(\mathcal{V}_\varepsilon(\sigma) - \nu(\overline{\sigma})\sigma)}}{\int \mathrm{d}\sigma\, e^{-\beta(\mathcal{V}_\varepsilon(\sigma) - \nu(\overline{\sigma})\sigma)}} \tag{3.40}$$

Around $\overline{\sigma} = 0$, the above equation can be further linearised into

$$\overline{\sigma} \simeq \frac{\int \mathrm{d}\sigma\, \sigma(1 + \beta\nu'(0)\overline{\sigma}\sigma)e^{-\beta\mathcal{V}_\varepsilon(\sigma)}}{\int \mathrm{d}\sigma\, (1 + \beta\nu'(0)\overline{\sigma}\sigma)e^{-\beta\mathcal{V}_\varepsilon(\sigma)}} \tag{3.41}$$

Since $\mathcal{V}_\varepsilon$ is symmetric in σ, the integrals can be easily reduced to

$$\overline{\sigma} \simeq \beta\nu'(0)\overline{\sigma}\frac{\int \mathrm{d}\sigma\, \sigma^2 e^{-\beta\mathcal{V}_\varepsilon(\sigma)}}{\int \mathrm{d}\sigma\, e^{-\beta\mathcal{V}_\varepsilon(\sigma)}} \tag{3.42}$$

Since $\lambda'(0) = F''(0) = \nu'(0) - (\varepsilon - C)$, $\nu(\overline{\sigma})$ can be linearly approximated around $\overline{\sigma} = 0$ to be

$$\nu(\overline{\sigma}) \simeq [F''(0) - (\varepsilon - C)]\overline{\sigma} + \mathcal{O}\big(\overline{\sigma}^2\big). \tag{3.43}$$

This approximation leads to

$$F''(0) \simeq \frac{\int \mathrm{d}\sigma\, e^{-\beta\mathcal{V}_\varepsilon(\sigma)}}{\beta\int \mathrm{d}\sigma\, \sigma^2 e^{-\beta\mathcal{V}_\varepsilon(\sigma)}} - (\varepsilon - C)\ , \tag{3.44}$$

which allows the numerical measurement of the range of ε satisfying $F''(0) = \lambda'(0) < 0$ at a given constant parameter C according to Equation (3.44). The result is shown in Figure 3.13 (b). From there, at $\alpha = 0.12$, one may read off an approximate range $2 < \varepsilon < 6$ allowing double minima in F. If the synchronisation is too weak, the system should be kept disordered with a global magnetisation close to 0, thus leading to a single minimum corresponding to a crossover scheme. If the synchronisation is too strong, the effect of the one-body potential $V_{\lambda_V,\lambda_\sigma}$ should be diluted, with $\varnothing$-particles being predominant in steady states due to difficulties with domain growth. This is also hindering the double-minima scheme. This can also be caused by increasing α, which is shown in Figure 3.3 and is reflected in field theories by (3.25), in that both ε and α stabilise the minima of the σ-symmetric potential $\mathcal{V}_\varepsilon(\sigma)$ at $\sigma = 0$. The larger α is, the smaller the range of ε allowing a double-well F is.

3.6 Summary and outlooks

Above, we discussed the rich phenomenologies encoded in the proposed particle-based model (3.1) which includes particles' inter-conversion through their deformations. The one-body potential $V_{\lambda_V,\lambda_\sigma}$, which mimics a chemical reaction landscape, tunes the probabilities of different steady states via its asymmetry in the presence of synchronisation between the reaction coordinates of neighbouring particles and the effect of repulsion on reaction coordinates. Although the steady states are always homogeneously ordered, the transient phase separation induced by particle deformation is non-trivial. We measured phase diagrams of steady states via particle-based simulations, which were later qualitatively recovered and further investigated at hydrodynamic level.

In fact, the probabilities of a steady state at different points in a phase diagram indicates the tendency of coarsening there. A higher probability of the steady state full of A-particles (B-particles) shows that the domain of A-particles (B-particles) are promoted during coarsening. In this sense, it is the transient LLPS that is under scrutiny, in that in a phase diagram we actually summarised the tendencies of spontaneous relaxations of phase-separated configurations under different asymmetric one-body potentials. In particular, under a symmetric V, the topology and shape of transient LLPS

determine the relaxation and the steady states: Bands are long-lived, whilst bubbles are unstable and shrink quickly to vanish. Under an asymmetric V, sufficiently large bubbles in which particles benefit from either energetic advantage or size advantage, which is due to stronger synchronisation by larger particles in the bubble, may be stable, and expands to dominate the steady state configuration.

As a motivation of our approach towards LLPS, recent studies have shown that phase separations between liquid components in biological cells may probably be transient states maintained by environments that periodically change in time rather than steady states [19]. In the framework of our work, the periodically changing environment may be mimicked by time-periodic changes of the asymmetries of the one-body potential. Our phase diagram, by indicating the fates of phase-separated configurations under different one-body potentials, provides a reference for potential ranges of rescaling factor pairs $(\lambda_V, \lambda_\sigma)$ involved in protocols of their time-periodic changes to be designed in the future, which bound the bubble sizes both from bottom and above.

Besides, rational insights into the maintained transient LLPS, in particular the evaluations of the future control protocols, entails a field-theoretic description framework. Since the phase separation in our scope is not steady, no conservation of global order (magnetisation) is needed. Being analogous to the Ising model with Glauber dynamics, our framework uses a Model-A-type field theory, which finally leads to homogeneous configurations as steady states. Without changes of rescaling factors $\lambda_V, \lambda_\sigma$ in time, our approach of analysing the field theory is limited to qualitatively reproducing the phase diagrams and understanding the stabilities of different homogeneous steady states by analysing the shape of the homogeneous part of the effective free energy $F(\overline{\sigma})$ along with its minima. Future evaluations of control protocols maintaining LLPS, in contrast, must consider inhomogeneities, i.e. the $(\partial_{\mathbf{r}}\overline{\sigma})^2$-terms should be included into the free energy being considered.

Moreover, by mapping the synchronisation interaction, the only source of non-equilibrium nature in our model, to an effective equilibrium, our mean-field approach has wiped out the entropy productions in a homogeneous block being maintained. This is not true in particle-based simulations as the ordering is due to the non-equilibrium synchronisation. The absence of entropy production is the consequence of a plethora of approximations we made during the derivation of the field theory. Substantially recovering this feature requires further refinement of our field theory.

Despite the limitations, we have still provided new theoretical possibilities that use Model A for maintained transient LLPS, in contrast to the usual approaches for steady-state LLPS conserving the global order (magnetisation),

such as Model B and its extensions [12, 159–161], and thus treating LLPS as steady states in an static environment. By introducing time-periodic control protocols to the asymmetric one-body potential, the LLPS achieved via particle inter-conversions can potentially be maintained in a periodically driven steady state, which is important for reactive systems.

Conclusion

Many-body dynamics often exhibits collective behaviours that are less sensitive to microscopic details than to some "collective modes" in larger scales. This fact motivates the use of field theories, which are meant for systems with a large number of degrees of freedom, as simplified models with a drastically reduced number of relevant degrees of freedom. In the framework of field theories, a richness of collective behaviours, such as pattern formation, defect formation, phase separation, etc., can be systematically studied or even predicted. For instance, the Turing patterns in various different contexts may be universally realised by the CGLE, as is shown in Chapter 1.

An advantage of using field theories often lies in their simple construction. Quite often, based on phenomenologies of collective behaviours, especially symmetries, one can argue for the relative terms in a field theory. For instance, as is shown in Chapter 1, the ϕ^4-form of the L-G theory is constructed via removing all odd order terms of ϕ due to the $\mathbb{Z}_2$-symmetry and keeping the ϕ^4-term with positive coefficient to bound the ϕ-values whilst allowing phase transitions by changing the coefficient of the ϕ^2-term. This simplest construction, without being extended to higher orders of ϕ, has already been sufficient for describing a wide range of phase transitions.

However, many patterns of biological relevance, such as contraction wave propagation, do not have clear symmetries, and are therefore difficult to be captured by simple field theories constructed via the top-down approach like in the L-G theory. Studies on these patterns should then start from reproductions of these patterns using microscopic models. In Chapter 2, we propose a simple model effectively reproducing the propagation of contraction waves in living biological tissues, which goes beyond former realisations by other researchers using vertex models [9]. The use of deforming spherical particles in our model replaces the cells in vertex models to mimic living biological cells. This replacement reduces the complexity of vertex models coming from irregular shapes of cells, thus enabling further extensive studies of our model as a novel class of active matter, namely PAM.

Further studies on PAM may propose lattice-based models that reproduce

the travelling contraction waves in our particle-based simulations and deriving a field theory via coarse-graining of the proposed lattice models. With a comparison to our field theory, the essential parts and their roles in wave pattern formation may be identified. Also, more details about wave patterns in particle-based simulations, such as defect formation and motility, deserve further attention.

Inspired by the patterns in PAM, in Chapter 3, we extend the model to allow particle sizes to vanish in order to realise LLPS. We remove the activity and bound the particle sizes with a triple-well one-body potential. By regarding the particles whose internal states are in different one-body potential wells as different species, we build a particle-based model of dense assemblies accommodating LLPS. Using particle-based simulations, we observe that the LLPS occuring in our model is a transient state during a multistep relaxation towards a homogeneous steady state. The transient LLPS is formed by species interconversion from a disordered initial configuration, and coarsens into a homogeneous steady state. By adding asymmetries to the one-body potential, we find that steady states of different species exist with different probabilities. This is caused by the impact of asymmetries in the one-body potential on the formation of transient LLPS and the coarsening of LLPS.

Like for PAM, we systematically coarse-grain the particle-based model allowing transient LLPS into a field theory of Model-A type, which is consistent with the transient nature of LLPS in our particle-based model. This field theory maps our model to an effective equilibrium. Tuning the asymmetries in the one-body potential leads to a qualitatively similar shape of the phase diagram to that in particle-based simulations. In the framework of field theories, we investigate the phase transitions when tuning the asymmetries in the one-body potential via a free-energetic approach. Based on our systematic study on the impact of asymmetric one-body potentials, future efforts can be devoted to designing control protocols over asymmetries in the one-body potential to maintain a transient LLPS [19].

In this thesis, we present two examples of the use of deforming spherical particles to compose particle-based models giving rise to collective behaviours induced by particle deformation. Based on these models, field theories can be subsequently derived to indicate the essential ingredients of a field theory giving rise to such collective behaviours. Finding convincing links between models of deforming spherical particles [15, 16, 162], and vertex models [6, 7, 9, 163] would be an expected further extension. Also, one may take inspiration from our field theories to try building simpler field-theoretic descriptions via a top-down approach. Overall, reliably reproducing and understanding collective behaviours in experiments and building up simple yet effective field theories should be the long-standing goal of the research work in our line.

Bibliography

[1] R. Alert and X. Trepat, "Physical models of collective cell migration", Annual Review of Condensed Matter Physics **11**, 77–101 (2020).

[2] D. Gross, A. Sevrin, and B. Shraiman, *The physics of living matter: space, time and information* (World Scientific, 2020).

[3] X. Serra-picamal, V. Conte, R. Vincent, E. Anon, D. Tambe, E. Bazellieres, J. Butler, J. Fredberg, and X. Trepat, "Mechanical waves during tissue expansion", Nature Physics **8**, 1–7 (2012).

[4] S. Tlili, E. Gauquelin, B. Li, B. Ladoux, H. Delanoë-ayari, and F. Graner, "Collective cell migration without proliferation: density determines cell velocity and wave velocity", Royal Society Open Science **5**, 172421 (2018).

[5] D. Bi, X. Yang, C. Marchetti, and L. Manning, "Motility-driven glass and jamming transitions in biological tissues", Physical Review X **6**, 021011 (2016).

[6] T. Nagai and H. Honda, "A dynamic cell model for the formation of epithelial tissues", Philosophical Magazine B **81**, 699–719 (2001).

[7] A. Fletcher, M. Osterfield, R. Baker, and S. Shvartsman, "Vertex models of epithelial morphogenesis", Biophysical Journal **106**, 2291–2304 (2014).

[8] A. Amiri, C. Duclut, F. Jülicher, and M. Popović, "Random traction yielding transition in epithelial tissues", arXiv: 2211.02159 (2022).

[9] D. Boocock, T. Hirashima, and E. Hannezo, "Interplay between mechanochemical patterning and glassy dynamics in cellular monolayers", PRX Life **1**, 013001 (2023).

[10] D. Bernard, "Statistical field theory and applications: an introduction for (and by) amateurs", 1–167 (2019).

[11] I. Aranson and L. Kramer, "The world of the complex Ginzburg-Landau equation", Reviews of Modern Physics **74**, 99–143 (2002).

[12] P. Hohenberg and B. Halperin, "Theory of dynamic critical phenomena", Reviews of Modern Physics **49**, 435–479 (1977).

[13] A. Bray, "Theory of phase-ordering kinetics", Advances in Physics **51**, 481–587 (1993).

[14] L. Manning, "Essay: Collections of Deformable Particles Present Exciting Challenges for Soft Matter and Biological Physics", Physical Review Letters **130**, 130002 (2023).

[15] E. Tjhung and T. Kawasaki, "Excitation of vibrational soft modes in disordered systems using active oscillation", Soft Matter **13**, 111–118 (2017).

[16] Y. Togashi, "Modeling of nanomachine/micromachine crowds: Interplay between the internal state and surroundings", Journal of Physical Chemistry B **123**, 1481–1490 (2019).

[17] E. Tjhung and L. Berthier, "Discontinuous fluidization transition in time-correlated assemblies of actively deforming particles", Physical Review E **96**, 050601(R) (2017).

[18] Y. Shin and C. Brangwynne, "Liquid phase condensation in cell physiology and disease", Science **357** (2017).

[19] G. Charras and M. Lenz, "A biochemical timer phases condensates in and out in cells", Nature **609**, 469–470 (2022).

[20] D. Dean, "Langevin equation for the density of a system of interacting Langevin processes", Journal of Physics A: Mathematical and General **29**, L613 (1996).

[21] R. Brown, "A brief account of microscopical observations made in the months of June, July and August 1827, on the particles contained in the pollen of plants; and on the general existence of active molecules in organic and inorganic bodies ", The Philosophical Magazine **4**, 161–173 (1828).

[22] P. van der Pas, "The discovery of the brownian motion", Scientiarum Historia **13**, 27–35 (1971).

[23] A. Einstein, "Über die von der molekularkinetischen Theorie der Wärme geforderte Bewegung von in ruhenden Flüssigkeiten suspendierten Teilchen", Annalen der Physik **322**, 549–560 (1905).

[24] P. Langevin, "Sur la théorie du mouvement brownien", Comptes Rendus de l'Académie des Sciences **146**, 530–533 (1908).

[25] J. Perrin, "Mouvement brownien et molécules", Journal de Physique Théorique et Appliquée **9**, 5–39 (1910).

[26] J. Perrin, "L'agitation moléculaire et le mouvement brownien", Comptes Rendus de l'Académie des Sciences **146**, 967–970 (1908).

[27] C. Gardiner, *Handbook of stochastic methods for physics, chemistry, and the natural sciences* (Springer-Verlag, Berlin, Heidelberg, New York, 1985).

[28] C. Marchetti, J. Joanny, S. Ramaswamy, T. Liverpool, J. Prost, M. Rao, and R. Simha, "Hydrodynamics of soft active matter", Reviews of Modern Physics **85**, 1143–1189 (2013).

[29] M. Das, C. Schmidt, and M. Murrell, "Introduction to active matter", Soft Matter **16**, 7185–7190 (2020).

[30] M. Cates and J. Tailleur, "Motility-induced phase separation", Annual Review of Condensed Matter Physics **6**, 219–244 (2015).

[31] A. Cavagna and I. Giardina, "Bird Flocks as Condensed Matter", Annual Review of Condensed Matter Physics **5**, 183–207 (2014).

[32] O. Reichhardt and C. Reichhardt, "Ratchet effects in active matter systems", Annual Review of Condensed Matter Physics **8**, 51–75 (2017).

[33] R. Alert, J. Casademunt, and J. Joanny, "Active turbulence", Annual Review of Condensed Matter Physics **13**, 143–170 (2022).

[34] T. Vicsek, A. Czirók, E. Ben-Jacob, I. Cohen, and O. Shochet, "Novel type of phase transition in a system of self-driven particles", Physical Review Letters **75**, 1226–1229 (1995).

[35] H. Chaté, "Dry Aligning Dilute Active Matter", Annual Review of Condensed Matter Physics **11**, 189–212 (2020).

[36] D. Chowdhury, L. Santen, and A. Schadschneider, "Statistical physics of vehicular traffic and some related systems", Physics Report **329**, 199–329 (2000).

[37] H. Wagner, "Long-wavelength excitations and the Goldstone theorem in many-particle systems with "broken symmetries"", Zeitschrift für Physik **195**, 273–299 (1966).

[38] N. Mermin, "Crystalline order in two dimensions", Physical Review **176**, 250–254 (1968).

[39] J. Toner and Y. Tu, "Long-range order in a two-dimensional dynamical XY model: How birds fly together", Physical Review Letters **75**, 4326–4329 (1995).

[40] J. Toner and Y. Tu, "Flocks, herds, and schools: A quantitative theory of flocking", Physical Review E **58**, 4828–4858 (1998).

[41] J. Toner, Y. Tu, and R. Sriram, "Hydrodynamics and phases of flocks", Annals of Physics **318**, 170–244 (2005).

[42] B. Mahault, F. Ginelli, and H. Chaté, "Quantitative Assessment of the Toner and Tu Theory of Polar Flocks", Physical Review Letters **123**, 1–6 (2019).

[43] J. Palacci, S. Sacanna, A. Steinberg, D. Pine, and P. Chaikin, "Living crystals of light-activated colloidal surfers", Science **339**, 936–940 (2013).

[44] M. Cates and J. Tailleur, "When are active Brownian particles and run-and-tumble particles equivalent? Consequences for motility-induced phase separation", Europhysics Letters **101** (2013).

[45] S. Jose, "First passage statistics of active random walks on one and two dimensional lattices", Journal of Statistical Mechanics: Theory and Experiment **2022**, 113208 (2022).

[46] E. Moen, K. Olsen, J. Rønning, and L. Angheluta, "Trapping of active Brownian and run-and-tumble particles: A first-passage time approach", Physical Review Research **4**, 1–8 (2022).

[47] P. Friedl and D. Gilmour, "Collective cell migration in morphogenesis, regeneration and cancer", Nature Reviews Molecular Cell Biology **10**, 445–457 (2009).

[48] S. Zehnder, M. Suaris, M. Bellaire, and T. Angelini, "Biophysical Letter Cell Volume Fluctuations in MDCK Monolayers", Biophysical Journal **108**, 247–250 (2015).

[49] R. Mueller, J. Alessandro, S. Begnaud, P. Marcq, J. Yeomans, and A. Doostmohammadi, "Sustained Oscillations of Epithelial Cell Sheets", Biophysical Journal **117**, 464–478 (2019).

[50] M. Matsuda, "ERK-Mediated Mechanochemical Waves Direct Collective Cell Polarization ERK-Mediated Mechanochemical Waves Direct Collective Cell Polarization", Developmental Cell **53**, 1–15 (2020).

[51] D. Boocock, N. Hino, N. Ruzickova, T. Hirashima, and E. Hannezo, "Theory of mechanochemical patterning and optimal migration in cell monolayers", Nature Physics **17**, 267–274 (2021).

[52] M. Weliky and G. Oster, "Dynamical models for cell rearrangement during morphogenesis", in *Gastrulation: Movements, Patterns and Molecules*, edited by R. Keller, W. Clark, and F. Griffin (Springer US, Boston, MA, 1991), pp. 135–146.

[53] S. Banerjee and C. Marchetti, "Continuum Models of Collective Cell Migration", Advances in Experimental Medicine and Biology **1146**, 45–66 (2019).

[54] S. Armon, M. Bull, A. Moriel, H. Aharoni, and M. Prakash, "Modeling epithelial tissues as active-elastic sheets reproduce contraction pulses and predict rip resistance", Communications Physics **4**, 1–9 (2021).

[55] S. Banerjee, K. Utuje, and C. Marchetti, "Propagating stress waves during epithelial expansion", Physical Review Letters **114**, 228101 (2015).

[56] K. Dierkes, A. Sumi, J. Solon, and G. Salbreux, "Spontaneous oscillations of elastic contractile materials with turnover", Physical Review Letters **113**, 1–5 (2014).

[57] P. Lötstedt, "Derivation of continuum models from discrete models of mechanical forces in cell populations", Journal of Mathematical Biology **83**, 1–31 (2021).

[58] Y. Kuramoto, "Self-entrainment of a population of coupled non-linear oscillators", in International symposium on mathematical problems in theoretical physics, edited by H. Araki (1975), pp. 420–422.

[59] M. Kardar, *Statistical physics of fields* (Cambridge University Press, 2007).

[60] A. Altland and B. Simons, *Condensed matter field theory*, 2nd ed. (Cambridge University Press, 2010).

[61] E. Peltola, "Toward a conformal field theory for Schramm-Loewner evolutions", Journal of Mathematical Physics **60**, 103305 (2019).

[62] L. Landau, "On the theory of phase transitions", Journal of Experimental and Theoretical Physics **1**, 234–252 (1937).

[63] V. Ginzburg and L. Landau, "On the theory of superconductivity", Journal of Experimental and Theoretical Physics **20**, 1064 (1950).

[64] V. Ginzburg, "Nobel lecture: on superconductivity and superfluidity (what i have and have not managed to do) as well as on the "physical minimum" at the beginning of the xxi century", Reviews of Modern Physics **76**, 981–998 (2004).

[65] C. Chang, S. Colin-Ellerin, and M. Rangamani, "Supersymmetric Landau-Ginzburg tensor models", Journal of High Energy Physics **2019**, 7 (2019).

[66] M. Tyler and D. Cameron, "Cellular pattern formation during retinal regeneration: A role for homotypic control of cell fate acquisition", Vision Research **47**, 501–511 (2007).

[67] S. Duran-Nebreda, J. Pla, B. Vidiella, J. Piñero, N. Conde-Pueyo, and R. Solé, "Synthetic Lateral Inhibition in Periodic Pattern Forming Microbial Colonies", ACS Synthetic Biology **10**, 277–285 (2021).

[68] A. Turing, "The chemical basis of morphogenesis", Philosophical Transactions of the Royal Society B: Biological Sciences **237**, 37–72 (1952).

[69] I. Prigogine and G. Nicolis, "Self-organisation in nonequilibrium systems: towards a dynamics of complexity", in *Bifurcation analysis: principles, applications and synthesis*, edited by M. Hazewinkel, R. Jurkovich, and J. H. P. Paelinck (Springer Netherlands, Dordrecht, 1985), pp. 3–12.

[70] B. Belousov, "A periodic reaction and its mechanism", in *Collection of short papers on radiation medicine for 1958* (Meditsina Publishers, Moscow, 1958).

[71] A. Zhabotinsky, "Periodic oxidizing reactions in the liquid phase", Doklady Akademii Nauk SSSR **157**, 392–395 (1964).

[72] R. Field and H. Foersterling, "On the oxybromine chemistry rate constants with cerium ions in the field-koeroes-noyes mechanism of the Belousov-Zhabotinskii reaction: the equilibrium HBrO2 + BrO3- + H+ -> 2BrO2- + H2O", The Journal of Physical Chemistry **90**, 5400–5407 (1986).

[73] L. Gyorgyi, T. Turanyi, and R. Field, "Mechanistic details of the oscillatory Belousov-Zhabotinskii reaction", The Journal of Physical Chemistry **94**, 7162–7170 (1990).

[74] W. Liu and U. Täuber, "Nucleation of spatiotemporal structures from defect turbulence in the two-dimensional complex Ginzburg-Landau equation", Physical Review E **100**, 1–15 (2019).

[75] M. Shifman, "Before supersymmetry", in *Advanced Topics in Quantum Field Theory: A Lecture Course* (Cambridge University Press, 2012), pp. 9–10.

[76] D. Frenkel and B. Smit, "Appendix F - Saving CPU Time", in *Understanding molecular simulation (second edition)*, Second Edition (Academic Press, San Diego, 2002), pp. 545–558.

[77] J. Maloney, E. Lehnhardt, A. Long, and K. van Vliet, "Mechanical fluidity of fully suspended biological cells", Biophysical Journal **105**, 1767–1777 (2013).

[78] R. Ni, M. Stuart, and M. Dijkstra, "Pushing the glass transition towards random close packing using self-propelled hard spheres", Nature Communications **4**, 1–7 (2013).

[79] L. Berthier, E. Flenner, and G. Szamel, "Glassy dynamics in dense systems of active particles", The Journal of Chemical Physics **150**, 200901, 10.1063/1.5093240 (2019).

[80] D. Bi, J. Lopez, J. Schwarz, and L. Manning, "A density-independent rigidity transition in biological tissues", Nature Physics **11**, 1074–1079 (2015).

[81] R. Thiagarajan, A. Bhat, G. Salbreux, M. Inamdar, and D. Riveline, "Pulsations and flows in tissues as two collective dynamics with simple cellular rules", iScience **25**, 105053 (2022).

[82] A. Martin, M. Kaschube, and E. Wieschaus, "Pulsed contractions of an actin-myosin network drive apical constriction", Nature **457**, 495–499 (2009).

[83] J. Solon, A. Kaya-Çopur, J. Colombelli, and D. Brunner, "Pulsed forces timed by a ratchet-like mechanism drive directed tissue movement during dorsal closure", Cell **137**, 1331–1342 (2009).

[84] S. Armon, M. Bull, A. Aranda-Diaz, and M. Prakash, "Ultrafast epithelial contractions provide insights into contraction speed limits and tissue integrity", Proceedings of the National Academy of Sciences of the United States of America **115**, E10333–E10341 (2018).

[85] G. Peyret, R. Mueller, J. d'Alessandro, S. Begnaud, P. Marcq, R. Mège, J. Yeomans, A. Doostmohammadi, and B. Ladoux, "Sustained oscillations of epithelial cell sheets", Biophysical Journal **117**, 464–478 (2019).

[86] V. Petrolli, M. Le Goff, M. Tadrous, K. Martens, C. Allier, O. Mandula, L. Hervé, S. Henkes, R. Sknepnek, T. Boudou, G. Cappello, and M. Balland, "Confinement-induced transition between wavelike collective cell migration modes", Physical Review Letters **122**, 168101 (2019).

[87] C. Heisenberg and Y. Bellaiche, "Forces in tissue morphogenesis and patterning", Cell **153**, 948–962 (2013).

[88] A. Bailles, C. Collinet, J. Philippe, P. Lenne, E. Munro, and T. Lecuit, "Genetic induction and mechanochemical propagation of a morphogenetic wave", Nature **572**, 467–473 (2019).

[89] A. Bailles, E. Gehrels, and T. Lecuit, "Mechanochemical principles of spatial and temporal patterns in cells and tissues", Annual Review of Cell and Developmental Biology **38**, 321–347 (2022).

[90] A. Karma, "Spiral breakup in model equations of action potential propagation in cardiac tissue", Physical Review Letters **71**, 1103–1106 (1993).

[91] J. Christoph, M. Chebbok, C. Richter, J. Schröder-Schetelig, P. Bittihn, S. Stein, I. Uzelac, F. Fenton, G. Hasenfuß, R. Gilmour, and S. Luther, "Electromechanical vortex filaments during cardiac fibrillation", Nature **555**, 667–672 (2018).

[92] A. Molavi Tabrizi, A. Mesgarnejad, M. Bazzi, S. Luther, J. Christoph, and A. Karma, "Spatiotemporal organization of electromechanical phase singularities during high-frequency cardiac arrhythmias", Physical Review X **12**, 021052 (2022).

[93] A. Karma, "Physics of cardiac arrhythmogenesis", Annual Review of Condensed Matter Physics **4**, 313–337 (2013).

[94] W. Rappel, "The physics of heart rhythm disorders", Physics Reports **978**, The physics of heart rhythm disorders, 1–45 (2022).

[95] J. Xu, S. Menon, R. Singh, N. Garnier, S. Sinha, and A. Pumir, "The role of cellular coupling in the spontaneous generation of electrical activity in uterine tissue", PLOS ONE **10**, 1–23 (2015).

[96] K. Myers and D. Elad, "Biomechanics of the human uterus", WIREs Systems Biology and Medicine **9**, e1388 (2017).

[97] Y. Koyano, H. Kitahata, and A. Mikhailov, "Diffusion in crowded colloids of particles cyclically changing their shapes", Europhysics Letters **128**, 40003 (2020).

[98] N. Oyama, T. Kawasaki, H. Mizuno, and A. Ikeda, "Glassy dynamics of a model of bacterial cytoplasm with metabolic activities", Physical Review Research **1**, 032038 (2019).

[99] S. Shinomoto and Y. Kuramoto, "Phase Transitions in Active Rotator Systems", Progress of Theoretical Physics **75**, 1105–1110 (1986).

[100] S. Luther, F. Fenton, B. Kornreich, A. Squires, P. Bittihn, D. Hornung, M. Zabel, J. Flanders, A. Gladuli, L. Campoy, E. Cherry, G. Luther, G. Hasenfuss, V. Krinsky, A. Pumir, R. Gilmour, and E. Bodenschatz, "Low-energy control of electrical turbulence in the heart", Nature **475**, 235–239 (2011).

[101] N. DeTal, A. Kaboudian, and F. Fenton, "Terminating spiral waves with a single designed stimulus: Teleportation as the mechanism for defibrillation", Proceedings of the National Academy of Sciences of the United States of America **119**, 1–8 (2022).

[102] P. Atkins, *Physical chemistry* (Oxford University Press, Oxford, United Kindom, 2022).

[103] G. Solomons and C. Fryhle, *Organic chemistry* (Wiley, Hoboken, NJ, 2017).

[104] I. Stakgold, "Reaction-diffusion problems in chemical engineering", in *Nonlinear diffusion problems: lectures given at the 2nd 1985 session of the centro internazionale matermatico estivo (c.i.m.e.) held at montecatini terme, italy june 10 – june 18, 1985*, edited by A. Fasano and M. Primicerio (Springer-Verlag, Berlin, Heidelberg, 1986), pp. 119–152.

[105] S. Kondo and T. Miura, "Reaction-Diffusion model as a framework for understanding biological pattern formation", Science **329**, 1616–1620 (2010).

[106] Y. Matsushita, "Microphase separation (of block copolymers)", in *Encyclopedia of polymeric nanomaterials*, edited by S. Kobayashi and K. Müllen (Springer-Verlag, Berlin, Heidelberg, 2014), pp. 1–6.

[107] M. Bazant, "Thermodynamic stability of driven open systems and control of phase separation by electro-autocatalysis", Faraday Discussions **199**, 423–463 (2017).

[108] T. Aslyamov, F. Avanzini, É. Fodor, and M. Esposito, "Non-ideal reaction-diffusion systems: Multiple routes to instability", arXiv: 2304.06394 (2023).

[109] K. Morita and N. Sano, in *Fundamentals of metallurgy*, Woodhead Publishing Series in Metals and Surface Engineering (Woodhead Publishing, 2005), pp. 82–108.

[110] J. Bocquet, G. Brebec, and Y. Limoge, in *Physical metallurgy (fourth edition)*, Fourth Edition (North-Holland, Oxford, 1996), pp. 535–668.

[111] J. De Hosson and B. Kooi, in *Handbook of surfaces and interfaces of materials* (Academic Press, Burlington, 2001), pp. 1–113.

[112] B. Bernu, J. Hansen, Y. Hiwatari, and G. Pastore, "Soft-sphere model for the glass transition in binary alloys: pair structure and self-diffusion", Physical Review A **36**, 4891–4903 (1987).

[113] T. Grigera and G. Parisi, "Fast monte carlo algorithm for supercooled soft spheres", Physical Review E **63**, 045102 (2001).

[114] A. Rudin and P. Choi, in *The elements of polymer science & engineering (third edition)*, Third Edition (Academic Press, Boston, 2013), pp. 391–425.

[115] L. Wilbraham, R. S. Sprick, K. Jelfs, and M. Zwijnenburg, "Mapping binary copolymer property space with neural networks", Chemical Science **10**, 4973–4984 (2019).

[116] E. Gutlederer, T. Gruhn, and R. Lipowsky, "Polymorphism of vesicles with multi-domain patterns", Soft Matter **5**, 3303–3311 (2009).

[117] T. Taniguchi, M. Yanagisawa, and M. Imai, "Numerical investigations of the dynamics of two-component vesicles", Journal of Physics: Condensed Matter **23** (2011).

[118] D. Marenduzzo and E. Orlandini, "Phase separation dynamics on curved surfaces", Soft Matter **9**, 1178–1187 (2013).

[119] M. Mercker, D. Hartmann, and A. Marciniak-Czochra, "A mechanochemical model for embryonic pattern formation: Coupling tissue mechanics and morphogen expression", PLoS ONE **8**, 1–6 (2013).

[120] G. Gueguen, N. Destainville, and M. Manghi, "Mixed lipid bilayers with locally varying spontaneous curvature and bending", European Physical Journal E **37**, 1–13 (2014).

[121] T. Schelling, "Dynamic models of segregation", The Journal of Mathematical Sociology **1**, 143–186 (1971).

[122] N. Annet and J. Naranjo, "Political Polarization in the American Public", Applied Microbiology and Biotechnology **85**, 2071–2079 (2014).

[123] K. Binder, C. Billotet, and P. Mirold, "On the theory of spinodal decomposition in solid and liquid binary mixtures", Zeitschrift für Physik B: Condensed Matter **30**, 183–195 (1978).

[124] S. Glotzer, E. di Marzio, and M. Muthukumar, "Reaction-Controlled Morphology ofPhase-Separating Mixtures Sharon", Physical Review Letters **73**, 1919–1922 (1994).

[125] J. Christensen, K. Elder, and H. Fogedby, "Phase segregation dynamics of a chemically reactive binary mixture", Physical Review E **54**, 2212–2215 (1996).

[126] M. Motoyama and T. Ohta, "Morphology of phase-separating binary mixtures with chemical reaction", Journal of the Physical Society of Japan **66**, 2715–2725 (1997).

[127] A. Lamorgese and R. Mauri, "Spinodal decomposition of chemically reactive binary mixtures", Physical Review E **94**, 1–9 (2016).

[128] M. Cotton, R. Golestanian, and J. Agudo-Canalejo, "Catalysis-Induced Phase Separation and Autoregulation of Enzymatic Activity", Physical Review Letters **129** (2022).

[129] B. Parry, I. Surovtsev, M. Cabeen, C. O'Hern, E. Dufresne, and C. Jacobs-Wagner, "The bacterial cytoplasm has glass-like properties and is fluidized by metabolic activity", Cell **156**, 183–194 (2014).

[130] A. Hyman, C. Weber, and F. Jülicher, "Liquid-liquid phase separation in biology", Annual Review of Cell and Developmental Biology **30**, 39–58 (2014).

[131] E. Ising, "Beitrag zur Theorie des Ferromagnetismus", Zeitschrift für Physik **31**, 253–258 (1925).

[132] K. Kawasaki, "Diffusion constants near the critical point for time-dependent Ising models. I", Physical Review **145**, 224–230 (1966).

[133] R. Glauber, "Time-Dependent Statistics of the Ising Model", Journal of Mathematical Physics **4**, 294–307 (1963).

[134] "Molecular model for chirality phenomena", Journal of Chemical Physics **145** (2016).

[135] T. Schmiedl and U. Seifert, "Stochastic thermodynamics of chemical reaction networks", The Journal of Chemical Physics **126**, 044101 (2007).

[136] R. Rao and M. Esposito, "Nonequilibrium thermodynamics of chemical reaction networks: wisdom from stochastic thermodynamics", Physical Review X **6**, 041064 (2016).

[137] M. Feinberg, *Foundations of chemical reaction network theory* (Springer Cham, Berlin, 2019).

[138] V. Bykov, V. Elokhin, and G. Yablonskii, "The simplest catalytic mechanism permitting several steady states of the surface", Reaction Kinetics and Catalysis Letters **4**, 191–198 (1976).

[139] P. Yu, "Multiplicity of steady states in oxidative heterogeneous catalysis", Theoretical and Expeimental Chemistry **28**, 225–237 (1993).

[140] C. Pantea, "On the persistence and global stability of mass-action systems", SIAM Journal on Mathematical Analysis **44**, 1636–1673 (2012).

[141] V. Bykov, G. Yablonskii, and V. Kim, "About a simple model of kinetics self-oscillations for the catalytic reaction of the oxidation of CO", Doklady Akademii Nauk USSR **242**, 637–639 (1978).

[142] G. Craciun and M. Feinberg, "Multiple equilibria in complex chemical reaction networks: semiopen mass action systems", SIAM Journal on Applied Mathematics **70**, 1859–1877 (2010).

[143] A. van der Schaft, S. Rao, and B. Jayawardhana, "On the mathematical structure of balanced chemical reaction networks governed by mass action kinetics", SIAM Journal on Applied Mathematics **73**, 953–973 (2013).

[144] M. Okino and M. Mavrovouniotis, "Simplification of mathematical models of chemical reaction systems", Chemical Reviews **98**, 391–408 (1998).

[145] T. Snowden, P. van der Graaf, and M. Tindall, "Methods of model reduction for large-scale biological systems: a survey of current methods and trends", Bulletin of Mathematical Biology **79**, 1449–1486 (2017).

[146] Z. Zi, "Sensitivity analysis approaches applied to systems biology models", English, IET Systems Biology **5**, 336–346(10) (2011).

[147] D. Degenring, C. Froemel, G. Dikta, and R. Takors, "Sensitivity analysis for the reduction of complex metabolism models", Journal of Process Control **14**, Dynamics, Monitoring, Control and Optimization of Biological Systems, 729–745 (2004).

[148] M. Apri, M. de Gee, and J. Molenaar, "Complexity reduction preserving dynamical behavior of biochemical networks", Journal of Theoretical Biology **304**, 16–26 (2012).

[149] S. Danø, M. Madsen, H. Schmidt, and G. Cedersund, "Reduction of a biochemical model with preservation of its basic dynamic properties", The FEBS Journal **273**, 4862–4877 (2006).

[150] Y. Hirono, T. Okada, H. Miyazaki, and Y. Hidaka, "Structural reduction of chemical reaction networks based on topology", Physical Review Research **3** (2021).

[151] F. Avanzini, N. Freitas, and M. Esposito, "Circuit theory for chemical reaction networks", Physical Review X **13**, 21041 (2022).

[152] H. Hinrichsen, "Non-equilibrium critical phenomena and phase transitions into absorbing states", Advances in Physics **49**, 815–958 (2000).

[153] G. Ódor, "Universality in nonequilibrium lattice systems", Reviews of Modern Physics **76**, 663–724 (2004).

[154] R. Ziff, E. Gulari, and Y. Barshad, "Kinetic phase transitions in an irreversible surface-reaction model", Physical Review Letters **56**, 2553–2556 (1986).

[155] U. Seifert, "Stochastic thermodynamics, fluctuation theorems and molecular machines", Reports on Progress in Physics **75**, 126001 (2012).

[156] K. Asheichyk and M. Krüger, "Using the fluctuation-dissipation theorem for nonconservative forces", Physical Review Research **1**, 1–5 (2019).

[157] H. Kramers, "Brownian motion in a field of force and the diffusion model of chemical reactions", Physica **7**, 284–304 (1940).

[158] R. Zwanzig, *Non-equilibrium statistical mechanics* (Oxford University Press, USA, 2001), p. 222.

[159] K. Shrinivas and M. Brenner, "Phase separation in fluids with many interacting components", Proceedings of the National Academy of Sciences of the United States of America **118**, 1–8 (2021).

[160] F. Thewes, M. Krüger, and P. Sollich, "Composition Dependent Instabilities in Mixtures With Many Components", arXiv: 2211.04170 (2022).

[161] M. Akaberian, F. Thewes, P. Sollich, and M. Krüger, "Nonequilibrium mixture dynamics: A model for mobilities and its consequences", arXiv: 2302.02775 (2023).

[162] Y. Zhang and É. Fodor, "Pulsating active matter", arXiv: 2208.06831 (2022).

[163] C. Duclut, J. Paijmans, M. Inamdar, C. Modes, and F. Jülicher, "Nonlinear rheology of cellular networks", Cells & Development **168**, Quantitative Cell and Developmental Biology, 203746 (2021).